Development and study of novel mid-infrared frequency conversion sources

Biplob Kumar Nandy

Optical Parametric Oscillators Research Group, ICFO

Universitat Politècnica de Catalunya

A thesis submitted for the degree of

Doctor of Philosophy (PhD)

October 2020

Thesis advisor: Prof. Majid Ebrahim-Zadeh
ICREA Professor, Fellow, OSA, SPIE
ICFO-The Institute of Photonic Sciences

Thesis co-advisor: Dr. Chaitanya Kumar Suddapalli
Ramón y Cajal Fellow
ICFO-The Institute of Photonic Sciences

Dedicated to my family and friends.

Once you have tasted flight, you will forever walk the earth with your eyes turned skyward, for there you have been, and there you will always long to return.

-Leonardo da Vinci

Declaration

I hereby declare that the matter embodied in the thesis entitled, **"Development and study of novel mid-infrared frequency conversion sources"** is the result of the investigations carried out by me at the ICFO-Institute of Photonic Sciences, Castelldefels, Barcelona, Spain under the supervision of Prof. Majid Ebrahim-Zadeh, and Dr. Chaitanya Kumar Suddapalli, and that it has not been submitted elsewhere for the award of any degree or diploma. In keeping with the general practice in reporting scientific observations, due acknowledgement has been made whenever the work described is based on the findings of other investigators.

Biplob Nandy

Certificate

I hereby certify that the matter embodied and presented in this thesis entitled, **"Development and study of novel mid-infrared frequency conversion sources"** has been carried out by Mr Biplob Nandy at the ICFO-Institute of Photonic Sciences, Castelldefels, Barcelona, Spain, under my supervision, and that it has not been submitted elsewhere for the award of any degree or diploma.

Prof. Majid Ebrahim-Zadeh

(ICFO, Research Supervisor)

Acknowledgements

Personal Acknowledgements:

The outcome of this PhD thesis involves the efforts, support and inputs from a lot of people without whom it would have been difficult to accomplish the goals. I take this opportunity to thank the people who have been with me throughout this journey and of great value.

It is Prof. Majid Ebrahim-Zadeh's highly infectious enthusiasm for research that has helped me to carry out this work successfully. I owe an immense amount of gratitude to him for providing this unique opportunity to conduct my PhD studies under his supervision. I feel so lucky to have such a nice supervisor who is so friendly and professional and always approachable. He transformed my life and made me a much better person both personally and professionally.

I wholeheartedly thank Dr. S. Chaitanya Kumar for a lot of things. It is difficult to acknowledge in a constrained space the long hours of inspiring discussions I had with him, the priceless and timely advice he gave etc., still, I make a humble attempt by saying thanks. I would also like to thank Sree (Chaitanya's wife), she is a wonderful person, very kind and generous. On several occasions, I had the opportunity to taste some excellent food cooked by her. She is also a great mentor and she gave me a lot of moral support and motivation during some very tough times during my PhD. There is no way that I could thank her in a few words, still my hearty thanks to you.

This project would not have been possible without the help and support from my labmates, Pep, Callum, Sukeert, Anuja, Hanyu, Jun, Shahrzad and Kavita. Hearty thanks to Adolfo for teaching me the art of femtosecond laser alignment and for several hours of playing chess and also for his positive and useful comments for my chess tournaments. My sincere thanks to Francisco

Bernal for helping me with the spanish translation of the abstract of my thesis.

I want to express my gratitude to all my friends at ICFO, Santanu, Biswajit, Swapan, Abhijeet, Hitesh and Gourab for their encouragement and good wishes.

It gives me immense pleasure to express gratitude towards Prof. Lluis Torner (Director, ICFO) and the management team for sharing their knowledge, providing support and help whenever I needed.

I would like to thank my girlfriend/best friend Aishwarya for her support, understanding, patience, and energy during my time as a PhD student, and simply for being at my side. Without you, I would not be where I am today.

I would like to thank my former supervisors at Max-Planck Institute for Chemistry, Mainz, namely Dr. Hartwig Harder and Dr. Monica Martinez for being great mentors and friends over these years. You guys were the first people who gave me the opportunity of getting international exposure in science and research. I would also like to thank Markus Rudolf for sharing his immense knowledge and wisdom and for being so kind.

My sincere thanks to Prof. K. P. Ramesh at Indian Institute of Science for introducing me to research and giving me the opportunity to do world class research in his lab. You have been very supportive and wise and our discussions have always been fruitful.

I thank all the people whom I have ever worked with because without your contribution (small or big), things would have been different but I like the way it is now.

Finally, I sincerely thank my parents and my sister who have made me the person I am today. My father taught me not to go for the easy choices and to never give up. This thesis also is for you.

Formal Acknowledgements:

The research presented in this doctoral thesis was partially supported by the Ministro de Ciencia, Innovación y Universidades (MICINN) (nuOPO, TEC2015-68234-R); Generalitat de Catalunya (CERCA Programme); Severo

Ochoa Programme for Centres of Excellence in R&D; European Social Fund (ESF) (BES-2016-079359, Project: SEV-2015-0522-16-1); Fundación Cellex; European Commission (EC) (Mid-Tech, H2020-MSCA-ITN-2014).

To cite this document:

```
@phdthesis{nandy2020thesis,
  author = {Biplob K. Nandy},
  title  = {Development and study of novel mid-infrared frequency conversion sources}
  year   = {2020},
  school = {Universitat Polit\`{e}cnica de Catalunya}
}
```

Copyright and License:

Abstract

Tunable narrow-linewidth and broadband laser sources in the mid-infrared (mid-IR) wavelength range are extremely desirable in all time scales for their several useful applications in spectroscopy, imaging, optical communication and medical sciences to name a few. The one very important application of high-power tunable narrow-linewidth mid-IR laser sources in the 2 μm wavelength range is the ability to pump cascaded mid-IR optical parametric oscillators (OPO) for generating tunable wavelengths beyond 4 μm using semiconductor nonlinear crystals such as $ZnGeP_2$ (ZGP) or orientation patterned GaAs (OP-GaAs). These crystals have very good linear and nonlinear optical properties along with good transparency beyond 4 μm wavelengths unlike oxide-based materials such as MgO:PPLN which have strong multi-phonon absorption beyond 4 μm wavelengths. However, both ZGP and OP-GaAs cannot be pumped by commercially available 1 μm lasers due to linear and nonlinear absorptions below ~2 μm wavelengths.

In this thesis, we have demonstrated some very useful high-power narrow-linewidth tunable 2 μm nanosecond and picosecond high-repetition-rate sources with very good spatial beam qualities. We have further demonstrated a picosecond mid-IR idler-resonant MgO:PPLN based OPO with intra-cavity *second-harmonic-generation* (SHG). This helps in covering the essential wavelength gap between 1.064 μm and 1.45 μm when pumped by Yb-fiber laser at 1.064 μm. This wavelength gap is generally not covered by MgO:PPLN based SROs that are signal resonant due to the material transparency of MgO:PPLN which doesn't allow the idler wave to go above ~4 μm wavelength, thereby restricting the signal wave from reaching below ~1.45 μm.

Due to the requirement of synchronous pumping, the OPOs typically tend to be relatively bulky and of large size, which can restrict its practical utility in space-constrained applications. We address this challenge by demonstrating a compact picosecond high-repetition rate singly resonant OPO (SRO) with intracavity-mirror-retro-reflector fiber (IMRF) that enables two-fold reduction in the form-factor. This IMRF OPO demonstrates a high wavelength tunability from ~1.45 μm to ~4 μm with high spectral brightness and exceptionally good output beam quality.

In our attempt to further reduce the size and complexity of nonlinear frequency conversion sources, we have demonstrated the first single-pass optical parametric generation (OPG) and amplification (OPA) in MgO:PPLN with record high conversion efficiency of >59% without the requirement of any seed-laser. We have demonstrated a record-low pump threshold energy of 7.5 nJ which is remarkably small and opens a whole new area of research on single-pass frequency conversion devices based on OPG/OPA. Our system is highly tunable near ~2 μm region with >8 W of single-pass output power while pumped with ~14 W of pump power at 1064 nm.

Finally, in this thesis, we have demonstrated the first phase-locked picosecond OPO with record high output power and spectral bandwidth near ~2 μm wavelength region. Such a device can be used as a high spectral brightness phase-locked super-continuum source for a huge array of applications.

Resumen

Las fuentes láser de banda ancha y ancho de línea estrecho sintonizables en el rango de longitud de onda del infrarrojo medio (IR medio) son de gran interés en todas las escalas de tiempo por sus diversas aplicaciones en espectroscopia, imágenes, comunicación óptica y ciencias médicas, por nombrar algunas. Una aplicación muy importante de las fuentes láser de IR medio de ancho de línea estrecho sintonizable de alta potencia en el rango de longitud de onda de 2 μm es la capacidad de bombear osciladores ópticos paramétricos (OPO) de IR medio en cascada para generar longitudes de onda sintonizables más allá de 4 μm, usando cristales semiconductores no lineales tales como $ZnGeP_2$ (ZGP) o GaAs con patrón de orientación (OP-GaAs). Estos cristales tienen muy buenas propiedades ópticas lineales y no lineales junto con una buena transparencia más allá de las longitudes de onda de 4 μm, a diferencia de los materiales a base de óxido como MgO:PPLN que tienen una fuerte absorción de multifonones más allá de las longitudes de onda de 4 μm. Sin embargo, tanto ZGP como OP-GaAs no pueden ser bombeados por láseres de 1 μm disponibles comercialmente debido a absorciones lineales y no lineales por debajo de 2 μm de longitud de onda.

En esta tesis, hemos demostrado algunas fuentes de alta potencia sintonizables de 2 μm de nanosegundos y picosegundos de alta tasa de repetición con muy buena calidad de haz espacial. Además, hemos demostrado un OPO basado en MgO:PPLN de picosegundos resonante para el campo idler en el IR medio, con generación de segundo armónico (SHG) intracavidad. Esto permite cubrir la brecha de longitud de onda esencial entre 1.064 μm y 1.45 μm cuando se bombea con láser de fibra de Yb a 1.064 μm. Esta brecha de longitud de onda generalmente no está cubierta por los SRO basados en MgO:PPLN, que resuenan el campo señal, debido a la transparencia del material de MgO:PPLN, que no permite que el campo idler supere las 4 μm de longitud de onda, lo que restringe el alcance del campo señal por debajo de 1.45 μm.

Debido al requisito del bombeo síncrono, los OPOs suelen ser relativamente voluminosos y de gran tamaño, lo que puede restringir su utilidad prác-

tica en aplicaciones con limitaciones de espacio. Abordamos este desafío demostrando un sistema de picosegundo compacto de alta tasa de repetición de resonancia simple (SRO) con un espejo retro reflector intracavidad en fibra (IMRF) que permite una reducción doble en el factor de forma. Este IMRF OPO demuestra una alta sintonización de longitud de onda de 1.45 μm a 4 μm con un alto brillo espectral y una calidad de haz de salida excepcionalmente buena.

En nuestro intento de reducir aún más el tamaño y la complejidad de las fuentes de conversión de frecuencia no lineal, hemos demostrado la primera generación óptica paramétrica (OPG) y amplificación (OPA) de un solo paso en MgO:PPLN con un récord de alta eficiencia de conversión de >59% sin necesidad de ningún láser de inicio. Hemos demostrado un umbral de energía de bombeo récord bajo de 7,5 nJ, que es notablemente pequeño y abre una nueva área de investigación sobre dispositivos de conversión de frecuencia de un solo paso basados en OPG/OPA. Nuestro sistema es altamente sintonizable cerca de la región de 2 μm con >8 W de potencia de salida de un solo paso mientras se bombea con 14 W de potencia de bombeo a 1064 nm.

Finalmente, en esta tesis, hemos demostrado el primer OPO de picosegundos con ajuste de fases (mode-locked) con record en potencia de salida y un ancho de banda espectral cerca de la región de longitud de onda de 2 μm. Un dispositivo de este tipo se puede utilizar como una fuente supercontinua mode-locked de alto brillo espectral para una gran variedad de aplicaciones.

Publications

Journal Publications

1. **B. Nandy**, S. Chaitanya Kumar, J. C. Casals, H. Ye, and M. Ebrahim-Zadeh, "Tunable high-average-power optical parametric oscillators near 2 μm," *J. Opt. Soc. Am. B* **35**, C57-C67 (2018).
2. S. Parsa, S. Chaitanya Kumar, **B. Nandy**, and M. Ebrahim-Zadeh, "Yb-fiber-pumped, high-beam-quality, idler-resonant mid-infrared picosecond optical parametric oscillator," *Optics Express* **18**, 25436-25444 (2019).
3. **B. Nandy**, S. Chaitanya Kumar, and M. Ebrahim-Zadeh, "Phase-locked picosecond optical parametric oscillator," *Optics Letters* **45**, 3981-3984 (2020).
4. **B. Nandy**, S. Chaitanya Kumar, and M. Ebrahim-Zadeh, "Fiber-laser-pumped picosecond optical parametric generation and amplification in MgO:PPLN". (*accepted in Optics Letters*)
5. **B. Nandy**, S. Chaitanya Kumar, and M. Ebrahim-Zadeh, "Fiber-laser-based, 1-μm-pumped, high-power picosecond optical parametric oscillator covering the 1.3-1.5 μm region". (*submitted in Optics Express*)
6. S. Chaitanya Kumar, **B. Nandy**, and M. Ebrahim-Zadeh, "Pulse compression in single-pass high-repetition-rate degenerate picosecond optical parametric generation".(*submitted in Optics Express*)
7. **B. Nandy**, S. Chaitanya Kumar, and M. Ebrahim-Zadeh, "High repetition-rate phase-locked picosecond OPO with 8.6 W average power". (*To be submitted in Optics Express*)
8. **B. Nandy**, S. Chaitanya Kumar, and M. Ebrahim-Zadeh, "High-average-power, stable, compact and highly tunable picosecond fiber-retro-reflector based optical parametric oscillator". (*To be submitted in Optics Letters*)

Conference Publications

1. H.Ye, **B. Nandy**, S. Chaitanya Kumar, and M. Ebrahim-Zadeh, "Stable, high-average-power, degenerate optical parametric oscillator at 2.1 μm," *High-Brightness Sources and Light-driven Interactions, Strasbourg, France*, March 2018, paper JT5A.17.
2. **B. Nandy**, H. Ye, S. Chaitanya Kumar, and M. Ebrahim-Zadeh, "Stable, high-average-power, narrow-linewidth source at 2.1 μm pumped at 1.064 μm," *Conference on Lasers and Electro-Optics (CLEO), San Jose, California, USA*, May 2018, paper JTu2A.60.
3. **B. Nandy**, S. Chaitanya Kumar, and M. Ebrahim-Zadeh, "Compact, stable, high-average- power, integrated-mirror-fiber-feedback picosecond optical parametric oscillator for the near- and mid-infrared," *8th EPS-QEOD Europhoton Conference, Barcelona, Spain*, September 2018, paper WeP.20.
4. **B. Nandy**, S. Chaitanya Kumar, and M. Ebrahim-Zadeh, "8.3 W average power, 80% pump depletion, picosecond mid-infrared parametric generation and amplification at 80 MHz," *High-Brightness Sources and Light-driven interactions, Prague, Czech Republic*, March 2020, paper MT4C.3. **(post-deadline paper)**
5. **B. Nandy**, S. Chaitanya Kumar, and M. Ebrahim-Zadeh, "Phase-locked degenerate picosecond optical parametric oscillator with 2.8 W average power at 2 μm," *High-Brightness Sources and Light-driven Interactions, Prague, Czech Republic*, March 2020, paper JT6A.1. **(post-deadline paper)**
6. **B. Nandy**, S. Chaitanya Kumar, and M. Ebrahim-Zadeh, "Yb-fiber-pumped MgO:PPLN-based picosecond optical parametric oscillator tunable across 1.3-1.5 μm," *Conference on Lasers and Electro-Optics (CLEO), San Jose, California, USA*, May 2020, paper JTu2F.23.
7. **B. Nandy**, S. Chaitanya Kumar, and M. Ebrahim-Zadeh, "Broadband, efficient, high-power optical parametric generation in MgO:PPLN," *IEEE Photonics Conference (IPC), Vancouver, Canada*, September 2020, paper TuF2.3.

Contents

List of Figures xxi

List of Listings xxiv

List of Tables xxv

Glossary xxvii

1 Introduction 1

1.1 Background . . . 1

1.1.1 Applications of mid-IR OPO sources . . . 2

1.1.2 Need for mid-IR OPO sources . . . 4

1.2 Thesis Structure . . . 7

2 Basic Principles of Nonlinear Optics 13

2.1 Basics of nonlinear optics . . . 13

2.2 Second-order nonlinearity . . . 14

2.3 Nonlinear Susceptibility . . . 18

2.4 Coupled-wave equations . . . 19

2.5 Gain and amplification in parametric interactions . . . 21

2.6 Phase-matching . . . 22

2.6.1 Birefringent phase-matching . . . 23

2.6.2 Quasi-phase-matching . . . 26

2.7 Acceptance bandwidth . . . 29

2.8 Dispersion . . . 30

2.9 Optical parametric oscillator . . . 32

2.9.1 OPO resonance configurations . . . 33

2.9.2 Wavelength tunability 34
2.9.3 Cavity design 35

3 Narrow-linewidth near-degenerate optical parametric oscillators 37
3.1 Backround and motivation 37
3.2 High-average-power high-repetition-rate nanosecond OPO near 2 μm . . . 38
3.2.1 Experimental setup 39
3.2.2 Device tuning and characterization 40
3.3 High-average-power high-repetition-rate picosecond OPO near 2 μm . . . 49
3.3.1 Experimental setup 50
3.3.2 Device tuning and characterization 52
3.4 Conclusions 59

4 Fiber-laser-based, 1-μm-pumped, high power picosecond optical parametric oscillator covering the 1.3-1.5 μm region 65
4.1 Background and motivation 65
4.2 Experimental Setup 67
4.3 Device tuning and characterization 68
4.4 Conclusions 79

5 High-average-power, stable, compact and highly tunable picosecond optical parametric oscillator 83
5.1 Background and motivation 83
5.2 Experimental Setup 84
5.3 Device tuning and characterization 85
5.4 Conclusions 90

6 Fiber-laser-pumped picosecond optical parametric generation and amplification in MgO:PPLN 95
6.1 Background and motivation 95
6.2 Experimental Setup 97
6.3 Device tuning and characterization 98
6.4 Conclusions 105

7 Phase-locked picosecond optical parametric oscillator **109**

7.1 Background and motivation 109

7.2 Experimental Setup 110

7.3 Device tuning and characterization 112

7.4 Conclusions 117

List of Figures

1.1 Wavelength coverage of commercially available solid state lasers and all types of OPOs . . . 3
1.2 Main infrared wavelength sources and their emission range . . . 4
1.3 Main requirements for a nonlinear crystal to be used for mid-IR OPO pumped at 1.064 μm . . . 6

2.1 Potential energy profiles and resulting polarization versus time for linear and nonlinear mediums . . . 15
2.2 Schematic depiction of the second-order nonlinear processes. . . . 17
2.3 Refractive index surface in a positive uniaxaial crystal and wave vector, k. 25
2.4 Intensity of output waves in a parametric interaction for perfect (birefringent) phase-matching, quasi-phase-matching, and no phase-matching. 28
2.5 Single-pass gain as a function of phase-mismatch, Δk . . . 30
2.6 Schematic of an OPO. . . . 32
2.7 OPO resonance configurations . . . 34
2.8 OPO cavity designs . . . 35

3.1 Schematic of the experimental setup for the intracavity prism-coupled tunable 2 μm source. . . . 40
3.2 Signal wavelength tuning range and total output power generated from the prism-coupled nanosecond OPO. . . . 41
3.3 Wavelength tuning of the nanosecond OPO. . . . 43
3.4 Signal spectrum characteristics of the nanosecond OPO near degeneracy. 43
3.5 Spectral bandwidth measurements of the OPO output using the home-built grating spectrometer. . . . 45

3.6 Output power scaling of the prism-coupled MgO:PPLN OPO at various temperatures. . . . 46
3.7 Maximum average output power and output pulse duration at different signal wavelengths. . . . 47
3.8 Measurements of power stability for the OPO at different crystal temperatures, corresponding to different output wavelengths, and the pump beam over 1 hour. . . . 47
3.9 Measurements of beam quality and spatial beam profile of the nanosecond OPO output near degeneracy. . . . 48
3.10 Output spectrum from the nanosecond OPO using conventional plane-mirror cavity with no frequency selection elements, and prism cavity. . . . 49
3.11 Schematic of the experimental setup for the ~2.1 μm source pumped by a Yb-based fiber laser at 1064 nm. . . . 51
3.12 Parametric gain bandwidth of the OPO at degeneracy and GVM between the pump and the signal and the corresponding GVD as a function of the signal wavelength. . . . 53
3.13 Spectral characterization of the output beam from the OPO using a 400 lines/mm IDG at blaze angle of 25.2° and the calculated FWHM spectral bandwidth as a function of the beam diameter on the IDG with 400 lines/mm. . . . 54
3.14 Simultaneously measured output power and pump depletion as a function of the pump power for the picosecond OPO, and long-term power stability of the output from the degenerate OPO operating at 2.1 μm. Inset: spatial beam distribution of the OPO output at 2128 nm. . . . 56
3.15 M^2 measurement of the output beam at degeneracy. . . . 57
3.16 Cavity-delay tuning of the picosecond OPO. . . . 57
3.17 Spectrum of the resonating signal from the picosecond OPO at different IDG angles, and estimated spectral bandwidth selectivity as a function of the blaze angle deviation. . . . 58
3.18 Output spectrum from the synchronously pumped picosecond OPO using plane-mirror cavity, and intracavity diffraction grating in Littrow configuration for spectral control. . . . 59

4.1 Experimental setup of the idler-resonant PPLN OPO with intracavity SHG 67
4.2 Calculation of idler and SHG wavelength tuning 68
4.3 Signal and SHG total output power generated with respect to their corresponding wavelengths at fixed pump power 69
4.4 SHG spectrum over the entire tuning range 70
4.5 Signal spectrum over the entire tuning range 71
4.6 Output power scaling of the idler-resonant MgO:PPLN OPO 72
4.7 Measurements of power stability for the signal and SHG at fixed gain-crystal temperature of 23.5 °C 73
4.8 Measurement of spectrum stability for the SHG at fixed gain-crystal temperature of 23.5 °C 74
4.9 Signal, SHG and idler total output power generated with respect to their corresponding wavelengths at fixed pump power 74
4.10 SHG spectrum over the entire tuning range for OC cavity 75
4.11 SHG power scaling with respect to intra-cavity idler power 76
4.12 Measurements of power stability for the idler, signal and SHG at fixed gain-crystal temperature of 25 °C for OC cavity 77
4.13 Interferometric autocorrelation and optical spectrum of the SHG wave at 1392 nm for the intracavity SHG ring cavity OPO 77
4.14 Cavity detuning of SHG 78

5.1 Experimental setup of the compact IMRF picosecond OPO 85
5.2 Tuning range and average output power of the IMRF picosecond OPO . . 86
5.3 Signal and Idler power scaling of the IMRF OPO using a 50% signal OC 87
5.4 Variation of the signal and idler power as a function of the picosecond IMRF OPO cavity delay 88
5.5 Long-term power stability of the output waves from the IMRF picosecond OPO 88
5.6 Beam quality measurements of the signal and the idler of the IMRF OPO 89
5.7 Spectral stability of the signal output of the IMRF OPO around 1550 nm over the duration of 1 h 90
5.8 Interferometric autocorrelation and optical spectrum of the signal wave at 1550 nm for the IMRF OPO 91

6.1 Schematic of the picosecond OPG-OPA setup 97
6.2 Output spectral evolution, output spectra and total output power measured after the OPA stage as a function of the simultaneously varied MgO:PPLN crystal temperature 99
6.3 Power scaling characteristics of OPG and OPA stages at an operating temperature of 30 °C 100
6.4 Interferometric autocorrelation trace and corresponding spectra of the pump, OPG and OPA respectively 102
6.5 Simulated normalized temporal gain profile for signal pulse generation as a function of the phase-mismatch parameter in the high-gain limit and normalized signal pulse profile in the high-gain limit for ΔkL=0 104
6.6 Long-term power stability of OPA output and pump 105
6.7 Long-term spectral stability of the output from the OPA stage operating a central wavelength of 2078 nm 105

7.1 Experimental setup for the degenerate phase-locked picosecond OPO synchronously pumped by a mode-locked Yb-fiber laser 111
7.2 Picosecond OPO output spectrum in the absence of phase- locking and in degenerate phase-locked state. 112
7.3 Spatial f-$2f$ interference pattern of degenerate picosecond OPO output in phase-locked state. 113
7.4 Radio-frequency spectrum of picosecond OPO output in unlocked and phase-locked state. 114
7.5 Output power and spectrum of degenerate phase-locked picosecond OPO as a function of input pump power. 115
7.6 Picosecond OPO output power stability and spectral stability of picosecond OPO output in transition from unlocked to phase-locked regime. . . 115
7.7 Variation in repetition rate with time of input pump pulse train from the picosecond Yb-fiber laser, and the output pulse train from the phase-locked picosecond OPO, over 1 hour. 116
7.8 Spatial output beam profile of phase-locked picosecond OPO. 117
7.9 Typical interferometric autocorrelation profile of phase-locked OPO output pulses at 2128 nm, and input Yb-fiber pump pulses at 1064 nm. . . . 118

List of Tables

2.1 Numbering convention for nonlinear optical coefficients 18
2.2 Type I and type II phase-matching configurations for parametric process. 24

3.1 Comparison of the Performance Characteristics of the Plane-Mirror Nanosecond OPO and the Prism Cavity 50
3.2 Comparison of the Performance Characteristics of the Plane-Mirror Picosecond OPO and the IDG Cavity 60

4.1 M^2 data for the ring cavity OPO 76

Glossary

BBO	Beta barium borate (β-BaB_2O_4)
BPM	Birefringent phase-matching
CPM	Critical phase-matching
CSP	Cadmium silicon phosphide ($CdSiP_2$)
CW	Continuous Wave
DFG	Difference frequency generation
E	Electric field
FWHM	Full width at half maximum
IMRF	Integrated mirror retro-reflector fiber
LBO	Lithium triborate (LiB_3O_5)
mid-IR	Mid-infrared (2-12 μm wavelength)
NCPM	Noncritical phase-matching
OPA	Optical parametric amplification
OPG	Optical parametric generation
OP-GaAs	Orientation patterned gallium arsenide
OP-GaP	Orientation patterned gallium phosphide
OPO	Optical parametric oscillator
PPKTP	Periodically poled potassium titanyl phosphate
PPLN	Periodically poled lithium niobate
PPLT	Periodically poled lithium tantalate
QCL	Quantum cascade lasers
QPM	Quasi-phase-matching
SFG	Sum frequency generation
SHG	Second harmonic generation
SVEA	Slowly varying envelope approximation
UV	Ultraviolet
ZGP	Zinc germanium phosphide ($ZnGeP_2$)
$\chi^{(m)}$	m^{th} order susceptibility response tensor
P	Material polarization
c	Speed of light in vacuum
ω	Angular frequency
n	Refractive index
t	Time
Λ	Grating period
d_{eff}	Effective nonlinear coefficient
k_i	Wave vector
Δk	Wave vector mismatch
Γ	Gain factor
δ	Degeneracy factor
L	Interaction length
n_e	Extraordinary refractive index
n_o	Ordinary refractive index
L_{eff}	Effective crystal length

1

Introduction

1.1 Background

Several milestone discoveries and path-breaking developments in science and technology have been possible only because of lasers. Research has been going at an amazing pace in search for new uses of lasers. A big impact in nanotechnology [1], in the development of super-tiny machines and tools has been possible only because of advanced laser sources which can be controlled very precisely. Current generation lasers can be used to make molecule-size motors and can also be used as "optical tweezers" to move atoms [2]. Scientists have been working on using lasers to transform the shape of molecules [3] by varying laser's wavelength which could lead to advanced materials [4] and breakthroughs in medical sciences [5] leading to next-generation medicines.

Since, the first demonstration of coherent light source in the form of a ruby laser in 1960 by Maiman [6], several successful efforts have been made to improve the laser technology. Major improvements have been made in terms of wavelength tunability, good beam quality and high output power in both pulsed and continuous-wave (CW) modes of operation. Lasers have revolutionized the field of experimental nonlinear optics research, the first of the many successes, was the demonstration of *second-harmonic-generation* (SHG) in a quartz crystal by Franken and his co-workers in 1961 [7].

The field was further revolutionized with the development of the required theory for parametric electromagnetic interactions by Armstrong *et. al.* in 1962, revealing that by exploiting the concept of phase-matching in a nonlinear medium, light could be converted from common laser emission wavelengths to new wavelengths [8]. Intense

phase-matched SHG was demonstrated soon after, with *difference-frequency-generation* (DFG) reported in 1963 [9], and finally the first optical parametric oscillator (OPO) was demonstrated in 1965 by Giordmaine and Miller [10]. Driven by a laser source, an OPO produces coherent light output which can be tuned continuously over a wide wavelength range and has all properties of an ordinary laser.

In the face of all this impressive early progress, translating OPOs to other wavelengths and timescales proved challenging due to slow development of reliable high-power lasers with high spatial and spectral coherence, crystals with poor optical properties, and very low-quality optical coatings. Occasional reports continued throughout the late 1960s and 1970s, including Byer demonstrating the first CW visible OPO in 1968 [11], and the first synchronously-pumped picosecond OPO in 1977 [12], however, OPOs still remained far from a practical and reliable technology. In 1980s, the development of new nonlinear materials, such as β-BaB_2O_4 (BBO) [13], LiB_3O_5 (LBO) [14], and $KTiOPO_4$ (KTP) [15], once again created a major interest in parametric devices. Presently, OPOs cover a huge part of the visible and infrared spectrum which is not covered by any tunable solid-state lasers due to lack of appropriate gain material, as shown in Figure 1.1.

1.1.1 Applications of mid-IR OPO sources

Molecular spectroscopy is one of the very first applications of coherent mid-IR sources. Molecules characteristically absorb light at one or more specific wavelengths due to their vibration frequencies in the medium [16], as shown in the inset of Figure 1.1. Free-space optical communication is another important application of mid-IR wavelengths [17]. In the present digital age, it is an ever increasing requirement for communication networks to transport more information at higher bit-rates. And in order to boost the bit-rate, the carrier frequency needs to be increased. In the recent past, radio frequency (RF) communications have shifted from the 3-30 GHz range (microwaves) to the 30-300 GHz range (millimeter waves). The next logical step would be to shift to eye-safe optical wavelengths in the mid-IR in order to achieve even higher carrier frequencies.

Free-space optical communication could be used for general public applications as an alternative to expensive optical fibers and for developing next-generation WIFI networks which would ensure high bit-rate internet communication. Hence, there is a strong

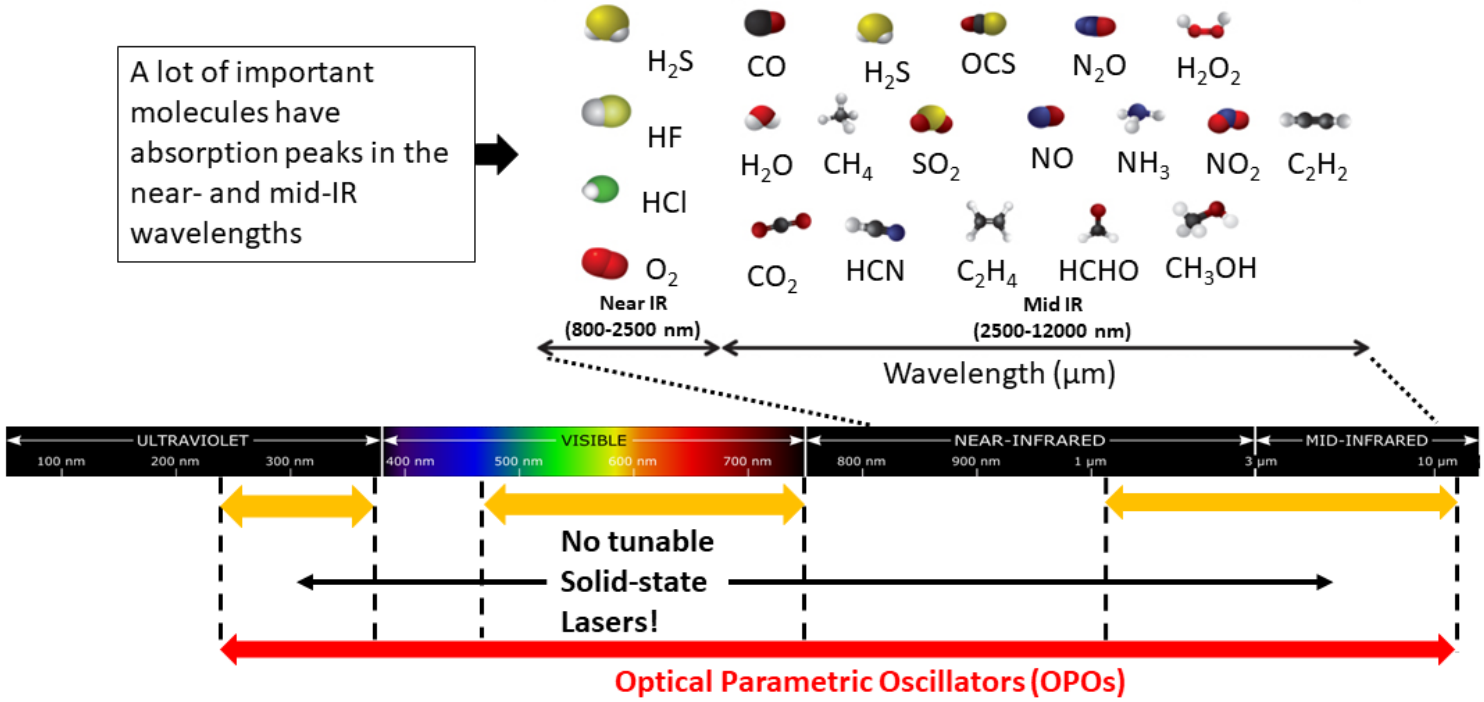

Figure 1.1: Wavelength coverage of commercially available solid state lasers and all types of OPOs. Inset: A few important molecules of interest which have absorption peaks in the near- and mid-IR region.

demand for the development of reliable, low-consumption, powerful mid-IR sources that can cater the above mentioned applications.

1.1.2 Need for mid-IR OPO sources

There are various types of infrared sources that have been developed to address the above mentioned applications, as presented in Figure 1.2. For instance, the CO_2 lasers [18] emit in the range between 9.6 and 10.6 μm with over 100 W in the CW operation regime. Similarly, CO lasers [19] emit in the 5-8 μm region when operated on the fundamental roto-vibrational mode and can also emit in the 2.5-4 μm region in the first harmonic. However, these lasers are typically cumbersome due to their large cooling systems.

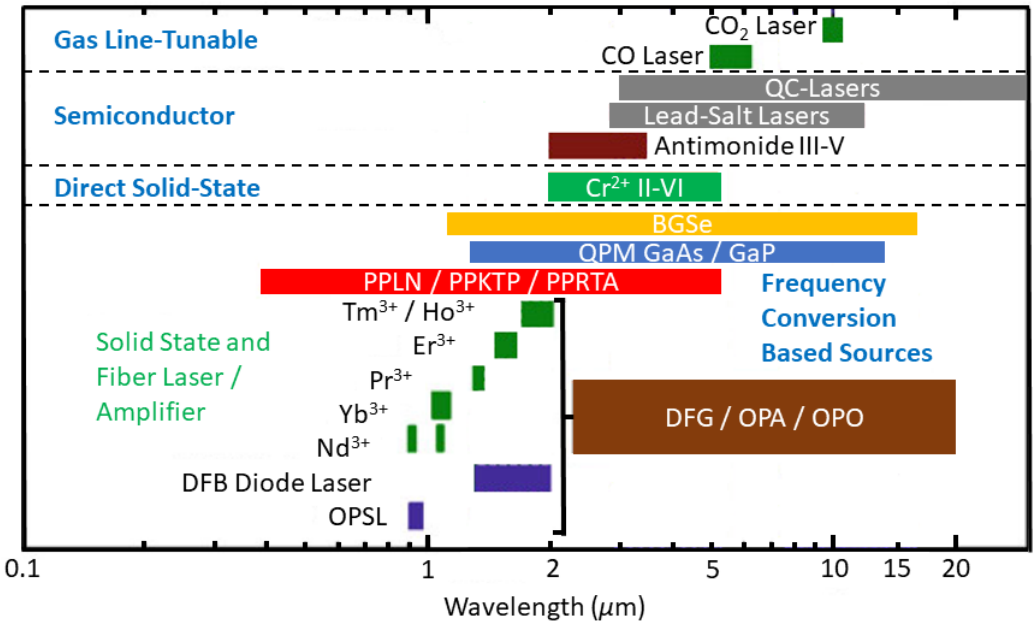

Figure 1.2: Main infrared wavelength sources and their emission range.

Lead-salt lasers are another type of mid-IR semiconductor laser sources based on PbSe, PbTe or PnS which operate in the 3 to 30 μm wavelength ranges [20, 21]. These lasers generally emit few μW output power and require cryogenic temperatures for CW operation, which is not practical. The performance of such lasers are sensitive to small temperature fluctuations. There are also antimony-based semiconductor laser, such as

AlGaIn/AsSb which emit below 3 μm [22] or GaInSb/InAs which emits in the 3 to 4 μm wavelength region [23]. However, these sources are limited to low powers.

In order to improve the performances of antimony-based mid-IR laser diodes, Yang [24] proposed a cascading design leading to quantum cascade lasers (QCLs). Here, the optical transition occurs between two sub-bands of the conduction band, which leads to large range of accessible wavelengths in the 3 to 250 μm region [25]. However, even after a decade of effort, unfortunately QCLs still require cryogenic temperatures for stable operation [26].

However, by exploiting the second order nonlinearities of optical crystals such as, BBO, LBO, KTP, $LiNbO_3$ (LN), $BaGa_4Se_7$ (BGSe) and others, allows us to obtain optical waves which are tunable all the way from the UV to the mid-IR wavelengths, and have proven to be more robust and reliable solution in comparison to the above mentioned. One of the most widely used nonlinear effects is *difference-frequency-generation* (DFG) in crystals such as LN which converts two waves at angular frequencies ω_3 and ω_1 in to a single wave at angular frequency $\omega_2 = \omega_3 - \omega_1$ [27]. Another important and widely used nonlinear effect is optical parametric generation (OPG), where we obtain a signal wave at ω_1 and an idler wave at ω_2 from a single pump wave at ω_3, such that $\omega_3 = \omega_1 + \omega_2$. This is also the key ingredient for OPOs, based on crystals such as MgO-doped periodically-poled lithium niobate (MgO:PPLN) [28], periodically-poled lithium tantalate (PPLT) [29], and others which provide very wide wavelength tunability in all time scales along with strong optical output powers [30].

In ferroelectric crystals such as LN, the orientation of the crystal is periodically switched, in order to obtain *quasi-phase-matching* (QPM), which allows all optical waves to propagate in the crystal with same phase, leading to strong optical output power. The period of the nonlinear crystal also determines the output wavelengths and wide wavelength tunability can be obtained with OPOs by using crystals with multiple periods [31]. However, oxide-based materials such as MgO:PPLN have some fundamental limitations in terms of OPO wavelength tunability due to strong multi-phonon absorption beyond 4 μm [32]. Hence, there is a huge interest in semiconductor nonlinear crystals such as $ZnGeP_2$ (ZGP) or orientation patterned GaAs (OP-GaAs) which have very good linear and nonlinear optical properties along with good transparency beyond 4 μm wavelengths. However, both ZGP and OP-GaAs cannot be pumped by

commercially available 1 μm lasers due to linear and nonlinear absorptions below ~2 μm wavelengths.

As a result, there has been significant efforts towards development of novel nonlinear crystals with large bandgaps, high damage threshold, high nonlinear coefficient and very wide transparency range from the near- to mid-IR in order to be able to use commercially available 1 μm lasers for pumping as shown in Figure 1.3. $CdSiP_2$ (CSP), BGSe and orientation patterned GaP (OP-GaP) are very good candidates which satisfy the above requirements along with *birefringent phase-matching* (BPM) and QPM, respectively. Recently, major advances have been made in the field of OPOs leading to numerous pulsed OPOs in the mid-IR based on OP-GaP (up to 13 μm) [33] and BGSe (up to 17 μm) [34] down to the UV spectral regions [35, 36].

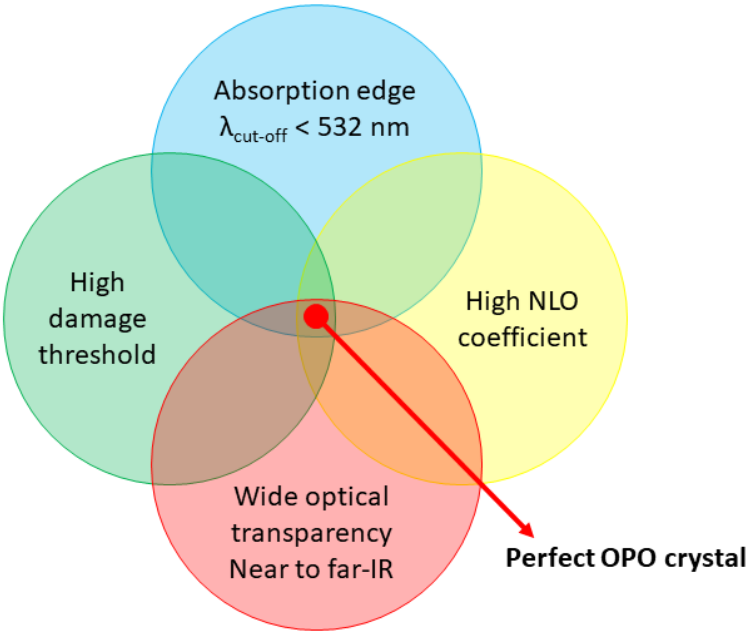

Figure 1.3: Main requirements for a nonlinear crystal to be used for mid-IR OPO pumped at 1.064 μm.

Most of this thesis is focused on picosecond synchronously-pumped OPOs, covering from 1.27 μm to ~4 μm wavelength region based on MgO:PPLN, providing high spectral and spatial beam quality with excellent output stabilities. Such OPOs represent viable alternatives to Tm^{3+}/Ho^{3+}-doped solid-state and fiber lasers for the generation of high-power radiation in the ~2 μm spectral range which can be used to pump mid-

IR nonlinear crystals such as ZGP and OP-GaAs. We also demonstrate high-power, high-repetition-rate picosecond single-pass OPG systems tunable in the 2 μm wavelength region pumped at 1.064 μm with record pump conversion efficiencies. Such simple picosecond single-pass source alleviates the requirement for complex OPO cavities for synchronous pumping, and provides multi-Watt average power in compact and cost-effective format with wide wavelength coverage across the near- and mid-IR for a variety of applications. We further report the first picosecond phase-locked OPO source with multi-Watt average powers using relatively simple, low-cost, and widely available mode-locked fiber pump lasers, paving the way for new applications in remote sensing, atmospheric optics, free-space communications, astronomy, and more.

1.2 Thesis Structure

This thesis is structured as follows.

Chapter 2: This chapter introduces the core concepts in nonlinear optics, which forms the basis for parametric wave interactions and frequency conversion. The second-order nonlinear processes such as SHG, *sum-frequency-generation* (SFG), DFG and OPG are discussed together with an introduction to phase-matching, dispersion and optical parametric oscillation.

Chapter 3: In this chapter, we report on the development of high-average-power nanosecond and picosecond laser sources tunable near 2 μm based on OPOs pumped by solid-state Nd:YAG and Yb-fiber lasers at 1.064 μm. By exploiting 50-mm-long MgO:PPLN as the nonlinear crystal and operating the OPO in a near-degenerate doubly resonant configuration with intracavity wavelength selection elements, we have generated tunable high-average-power radiation across 1880–2451 nm in high spectral and spatial beam quality with excellent output stability. In nanosecond operation, pumping with a Q-switched Nd:YAG laser and using an intracavity prism for spectral control, we have generated more than 2 W of average power in pulses of 10 ns duration at 80 kHz repetition rate with narrow linewidth (<3 nm), with $M^2 < 2.8$, and a passive power stability better than 2.2% rms over 1 h. In picosecond operation, pumping with a mode-locked Yb-fiber laser and using a diffraction grating as the wavelength selection

element, we have generated more than 5W of average power in pulses of 20 ps at 80 MHz repetition rate with narrow bandwidth (~2.5 nm), with $M^2 < 1.8$ and a passive power stability better than 1.3% rms over 2 h. The demonstrated sources represent viable alternatives to Tm^{3+}/Ho^{3+}-doped solid-state and fiber lasers for the generation of high-power radiation in the ~2 μm spectral range.

Chapter 4: In this chapter, we present an idler-resonant picosecond OPO based on 5%MgO:PPLN with intracavity SHG using a second MgO:PPLN crystal with fanout grating structure. The OPO is synchronously pumped by a mode-locked Yb-fiber laser delivering ~20 ps pulses at 79.5 MHz repetition-rate at 1064 nm. We have generated a broadly tunable radiation across 2610-3075 nm in the idler, 1627-1782 nm in the signal and 1272-1537 nm in the SHG with >1 W average output power in the 1290-1375 nm region.

Chapter 5: In this chapter, we present a compact picosecond OPO based on 5%MgO:PPLN in a novel configuration using a 80-cm-long single-mode integrated-mirror-retro-reflector fiber (IMRF) as the feedback element, resulting in a two-fold reduction in the overall footprint. The OPO is synchronously pumped by a mode-locked Yb-fiber laser delivering ~20 ps pulses at 79.5 MHz repetition-rate at 1064 nm. We have generated a broadly tunable radiation across 2211-3983 nm in the idler and 1451-2051 nm in the signal with maximum average output power of ~1 W in the signal and idler and excellent passive output stability of better than 0.8% rms over 3 hrs and immaculate beam quality. We also obtained excellent spectral stability of better than 0.004% rms over 3 hrs and very good pulse-repetition-rate stability of better than 0.00001% rms over 3 hrs.

Chapter 6: In this chapter, we report the generation of tunable high-repetition-rate picosecond pulses in the near-infrared at high average power with record conversion efficiency using singe-pass OPG and optical parametric amplification (OPA) in MgO:PPLN, for the first time to our knowledge. By deploying a mode-locked Yb-fiber laser at 1064 nm providing 21 ps pump pulses at 80 MHz, and a cascade of two 50-mm-long MgO:PPLN crystals, we generate up to 8.3 W of total average output power at a conversion efficiency of 59% over a tunable range of 513 nm, across 1902-2415 nm, with

a record threshold as low as 600 mW (7.5 nJ). The two-stage OPG-OPA scheme provides control over fine wavelength tuning and output spectral bandwidths, enabled by independent control of phase-matching in each crystal. The OPG-OPA output exhibits high spatial beam quality and excellent passive power and central wavelength stability better than 0.9% rms and 0.1% rms, respectively, over 1 hour. The OPA output pulses have a duration of ~11 ps, with 10dB bandwidth of ~350 nm at 2107 nm. And the OPG output pulses have duration of 5.2 ps with a FWHM spectral bandwidth of 117 nm at 2123 nm, resulting in a time-bandwidth product of $\Delta\tau\Delta\nu$ ~40, indicating ~4 times pulse compression with respect to the pump pulses. Theoretical simulations confirm the effect of the exponential gain in the parametric process as playing a key role in the resulting pulse compression.

Chapter 7: Finally, in the last chapter, we report a degenerate self-phase-locked picosecond OPO synchronously pumped by a mode-locked Yb-fiber laser at 1064 nm, delivering broadband output near 2 μm with 2.8 W of average power at ~80 MHz repetition rate. By exploiting a 50-mm-long MgO:PPLN crystal providing high gain and low group velocity dispersion under type 0 ($e \rightarrow ee$) phase-matching, the OPO generates phase-locked degenerate output spectrum with a bandwidth of ~202 nm centered at 2128 nm in pulses of ~21 ps duration with excellent passive long-term power and spectral stability in high spatial beam quality. Phase-locked operation results in spectral and power stabilization at exact degeneracy and is further validated by f-2f interferometry and radio-frequency measurements of OPO output. To the best of our knowledge, this is the first degenerate self-phase-locked OPO in picosecond time-scale, and the highest average power reported for a phase-locked ultrafast OPO to date.

References

[1] A. Cerdi, M. Venturi, and V. Balzani, "Light on molecular machines," *Chem Phys Chem* **11**, 3398-3403 (2010).

[2] S. R. Samoylenko, A. V. Lisitsin, D. Schepanovich, I. B. Bobrov, S. S. Straupe and S. P. Kulik, "Single atom movement with dynamic holographic optical tweezers," *Laser Physics Letters* **17**, 025203 (2020).

[3] P. M. Kraus, O. I. Tolstikhin, D. Baykusheva, A. Rupenyan, J. Schneider, C. Z. Bisgaard, T. Morishita, F. Jensen, L. B. Madsen and H. J. Woerner, "Observation of laser-induced electronic structure in oriented polyatomic molecules," *Nat. Comm.* **6**, 1-8 (2015).

[4] H. J. Booth, "Recent applications of pulsed lasers in advanced materials processing," *Thin Solid Films* **453**, 450-457 (2004).

[5] F. Trautinger, "Lasers in medicine," *Photochemical & Photobiological Sciences* **18**, 1619-1620 (2019).

[6] T. H. Maiman, "Stimulated optical radiation in ruby," *Nature* **187**, 493-494 (1960).

[7] P. A. Franken, A. E. Hill, C. W. Peters, and G. Weinrich, "Generation of Optical Harmonics," *Phys. Rev. Lett.* **7**, 118 (1961).

[8] J. A. Armstrong, N. Bloembergen, J. Ducuing, and P. S. Pershan, "Interactions between Light Waves in a Nonlinear Dielectric," *Phys. Rev.* **127**, 1918 (1962).

[9] A. W. Smith, and N. Braslau, "Observation of an optical difference frequency," *J. Appl. Phys.* **34**, 2105-2106 (1963).

[10] J. A. Giordmaine, and R. C. Miller, "Tunable Coherent Parametric Oscillation in $LiNbO_3$ at Optical Frequencies," *Phys. Rev. Lett.* **14**, 973 (1965).

[11] R. L. Byer, M. K. Oshman, J. F. Young, and S. E. Harris, "Visible CW parametric oscillator," *Appl. Phys. Lett.* **13**, 109-111 (1968).

[12] T. Kushida, Y. Tanaka, and M. Ojima, "Tunable picosecond pulse generation by optical parametric oscillator," *Japanese Journal of Applied Physics* **16**, 2227 (1977).

[13] C. Chen, B. Wu, A. Jiang, and G. You, "A New-Type Ultraviolet SHG Crystal–β-BaB_2O_4," *Science in China Series B-Chemistry, Biological, Agricultural, Medical & Earth Sciences* **28**, 235-243 (1985).

[14] C. Chen, Y. Wu, A. Jiang, B. Wu, G. You, R. Li, and S. Lin, "New nonlinear-optical crystal: LiB_3O_5," *J. Opt. Soc. Am. B* **6**, 616-621 (1989).

[15] F. C. Zumsteg, J. D. Bierlein, and T. E. Gier, "$K_xRb_{1-x}TiOPO_4$: a new nonlinear optical material," *J. Appl. Phys.* **47**, 4980-4985 (1976).

[16] A. Kosterev, G. Wysocki, Y. Bakhirkin, S. So, R. Lewicki, M. Fraser, F. Tittel, and R. F. Curl, "Application of quantum cascade lasers to trace gas analysis," *Appl. Phys. B* **90**, 165-176 (2008).

[17] A. Majumdar, and J. Ricklin, *Free-Space Laser Communications: Principles and Advances* (Springer, 2010).

[18] C. K. N. Patel, "Interpretation of CO_2 Optical Maser Experiments," *Phys. Rev. Lett.* **12**, 588 (1964).

[19] M. M. Mann, "CO electric discharge lasers," *AIAA Journal* **14**, 549-567 (1976).

[20] D. L. Partin, "Lead salt quantum effect structures," *IEEE Journal of quantum electronics* **24**, 1716-1726 (1988).

[21] M. Tacke, "Lead–salt lasers," *Philosophical Transactions of the Royal Society of London. Series A: Mathematical, Physical and Engineering Sciences* **359**, 547-566 (2001).

[22] J. G. Kim, L. Shterengas, R. U. Martinelli, and G. L. Belenky, "High-power room-temperature continuous wave operation of 2.7 and 2.8 μm In (Al) GaAsSb/GaSb diode lasers," *Appl. Phys. Lett.* **83**, 1926-1928 (2003).

[23] C. L. Canedy, W. W. Bewley, J. R. Lindley, I. Vurgaftman, C. S. Kim, M. Kim, and J. R. Meyer, "High-power continuous-wave midinfrared type-II "W" diode lasers," *Appl. Phys. Lett.* **86**, 211105 (2005).

[24] R. Q. Yang, "Infrared laser based on intersubband transitions in quantum wells," *Superlattices and Microstructures* **17**, 77-83 (1995).

[25] J. Faist, *Quantum cascade lasers* (OUP Oxford, 2013).

[26] M. S. Vitiello, G. Scalari, B. Williams, and P. De Natale, "Quantum cascade lasers: 20 years of challenges," *Optics Express* **23**, 5167-5182 (2015).

[27] S. Sanders, R. J. Lang, L. E. Myers, M. M. Fejer, and R. L. Byer, "Broadly tunable mid-IR radiation source based on difference frequency mixing of high power wavelength-tunable laser diodes in bulk periodically poled $LiNbO_3$," *Electronics Letters* **32**, 218-219 (1996).

[28] S. Chaitanya Kumar, J. Wei, J. Debray, V. Kremlin, B. Boulanger, H. Ishizuki, T. Taira, and M. Ebrahim-Zadeh, "High-power, widely tunable, room-temperature picosecond optical parametric oscillator based on cylindrical 5% MgO:PPLN," *Opt. Lett.* **40**, 3897-3900 (2015).

[29] S. Chaitanya Kumar, and M. Ebrahim-Zadeh, "High-power, fiber-laser-pumped, picosecond optical parametric oscillator based on MgO:sPPLT," *Opt. Express* **19**, 26660-26665 (2011).

[30] M. Ebrahim-Zadeh and M. H. Dunn, "Optical parametric oscillators," in *Handbook of Optics*, 2nd ed., Vol. IV (McGraw-Hill, 2000), pp. 1–72.

[31] S. Chaitanya Kumar, and M. Ebrahim-Zadeh, "Green-pumped optical parametric oscillator based on fan-out grating periodically-poled MgO-doped congruent $LiTaO_3$," *Opt. Lett.* **44**, 5796-5799 (2019).

[32] L. E. Myers, R. C. Eckardt, M. M. Fejer, R. L. Byer, and W.R. Bosenberg, "Multigrating quasi-phase-matched optical parametric oscillator in periodically poled LiNbO3," *Opt. Lett.* **21**, 591-593 (1996).

[33] L. Maidment, O. Kara, P. G. Schunemann, J. Piper, K. McEwan, and D. T. Reid, "Long-wave infrared generation from femtosecond and picosecond optical parametric oscillators based on orientation-patterned gallium phosphide," *Appl. Phys. B* **124**, 143 (2018).

[34] N. Y. Kostyukova, A. A. Boyko, V. Badikov, D. Badikov, G. Shevyrdyaeva, V. Panyutin, G. M. Marchev, D. B. Kolker, and V. Petrov, "Widely tunable in the mid-IR $BaGa_4Se_7$ optical parametric oscillator pumped at 1064 nm," *Opt. Lett.* **41**, 3667-3670 (2016).

[35] S. French, M. Ebrahim-Zadeh, and A. Miller, "High-power, high-repetition-rate picosecond optical parametric oscillator tunable in the visible," *Opt. Lett.* **21**, 976-978 (1996).

[36] G. K. Samanta, S. Chaitanya Kumar, A. Aadhi, and M. Ebrahim-Zadeh, "Yb-fiber-laser-pumped, high-repetition-rate picosecond optical parametric oscillator tunable in the ultraviolet," *Optics Express* **22**, 11476-11487 (2014).

2

Basic Principles of Nonlinear Optics

This chapter provides an overview of the relevant theory and dynamical equations of wave-mixing in nonlinear optics. More detailed and comprehensive treatment of nonlinear three-wave processes and devices can be found in several other references [1-3].

2.1 Basics of nonlinear optics

Optics is the study of interaction of light with matter. Light is generally expressed as an electromagnetic field with spatially and temporally varying electric and magnetic components, $E(\mathbf{r}, t)$ and $B(\mathbf{r}, t)$, respectively. Such an electromagnetic wave can interact with matter or, more precisely, with the charged particles inside matter. In most situations of practical interest in nonlinear optics, the interaction between the electric field and matter is much stronger in comparison to the magnetic field. Therefore, the magnetic field will not be considered in the light-matter interactions. Instead, the description in this thesis is limited to the interaction between the electrical field of a laser beam and a nonlinear dielectric medium with free charges and no currents.

For a laser propagating along x-axis, the electric field can be described by a complex amplitude, E, and an exponential function:

$$E(x,t) = \frac{1}{2}\{E_0(x,\omega)exp[i(\omega t - kx)]\} + c.c. \tag{2.1}$$

Here, $E_0(x,\omega)$ is the space and frequency dependent amplitude, k is the wave vector, ω is the circular frequency of the rapidly oscillating wave, and c.c. denotes the complex conjugate terms.

The interaction of electric field with a dielectric medium induces separation of bound charges, resulting in a collection of induced dipole moments. In order to describe the optical response, the polarization of the nonlinear material in which the frequency conversion is to take place needs to be considered. Since the incident laser light will induce material polarization, this in turn gives rise to a dipole moment. The dipole moment per unit volume is called the polarization of the material and the induced polarization, P, in its most general form, is given by a power series in the applied electric field as:

$$P = \varepsilon_0(\chi^{(1)}E + \chi^{(2)}E^2 + \chi^{(3)}E^3 + ...) = P^L + P^{NL} \tag{2.2}$$

where $P^L = \varepsilon_0\chi^{(1)}E$ is the linear polarization, and P^{NL} is the nonlinear polarization induced by sufficiently intense light field. $\varepsilon_0 = 8.85\times10^{-12}$ F/m is the electric permittivity in free space. $\chi^{(m)}$ is the susceptibility response tensor of m^{th} order and becomes a scalar quantity in an isotropic medium. The Lorentz model of a single electron of charge -e bound to a nucleus by a spring, which provides a linear restoring force proportional to the displacement, x, of the electron from the nucleus, is a useful model for linear optical effects. The microscopic polarization is the product of the charge times the displacement of the electron, such as $p = -ex$. In this linear model, the electron moves in response to an applied electric field $E(t)$, Figure 2.1(a), within a symmetric parabolic potential energy profile (Figure 2.1(b)), $U(x)$:

$$U(x) = -\int_{-x}^{x} eE(x,t).dx \tag{2.3}$$

2.2 Second-order nonlinearity

Nonlinearities are described by the higher-order terms of the potential energy profile, Figure 2.1(c). The polarization generated by a charge moving in such a potential has additional spectral components due to the quartic term of $U(x)$, but it does not contain a DC component, as would be required for optical rectification. Inversion symmetric materials, including liquids, gases, and glass, always have symmetric potentials and thus a vanishing $\chi^{(2)}$, while having a non-zero $\chi^{(3)}$ nonlinearity. To induce a nonlinear polarization, the electron must be displaced far enough from the nucleus to "see" the non-parabolic regions of the potential well and in the case of nonlinear optics, this is done by applying an electric force to the electron with a strong electric field, $F = -eE$,

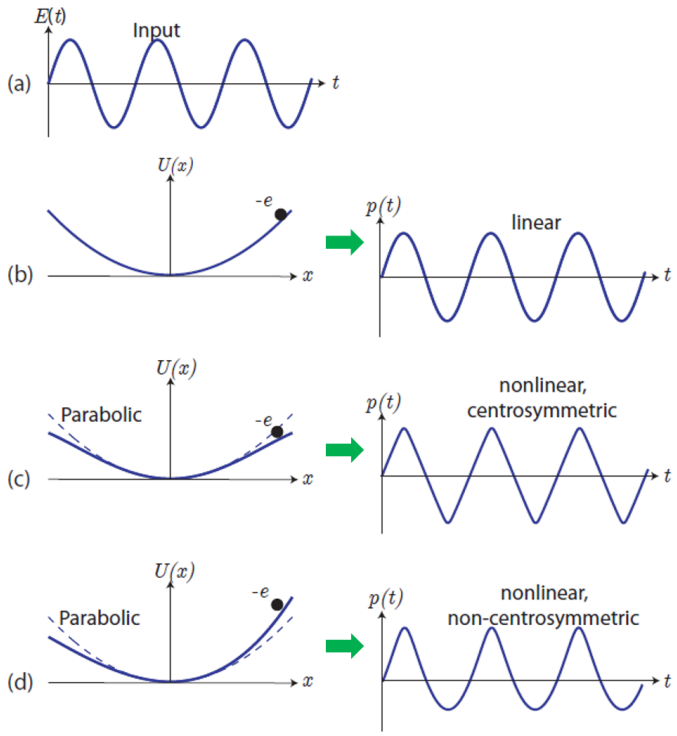

Figure 2.1: (a) Applied laser electric field versus time. (b) Parabolic potential energy profile and resulting polarization versus time in a linear model. (c) Potential energy profile with quadratic and quartic terms and the generated polarization in a nonlinear centrosymmetric model. (d) Potential energy profile with quadratic and cubic terms and the generated polarization in nonlinear non-centrosymmetric model.

such as those produced by lasers. In materials without inversion symmetry such as quartz, GaAs, GaP and lithium niobate, the potential well is no longer symmetric due to the cubic term of $U(x)$, Figure 2.1(d), and such materials will possess a non-zero $\chi^{(2)}$ value. The polarization of an electron moving in such a potential contains additional spectral components as well as a DC term and the generation of additional spectral components can be described in a more quantitative fashion.

The second-order nonlinear polarizability, $P^{(2)}$, is used to describe the three-wave mixing processes. Mathematically, it can be represented as:

$$P^{(2)} = \varepsilon_0 \chi^{(2)} : EE \tag{2.4}$$

where $\chi^{(2)}$ is the second-order nonlinear susceptibility of the material, which gives rise to familiar nonlinear optical processes such as *second-harmonic-generation* (SHG),

sum-frequency-generation (SFG), *difference-frequency-generation* (DFG), and most importantly in the context of this thesis, *optical parametric generation* (OPG) and *amplification* (OPA), and *optical-parametric-oscillator* (OPO).

If we assume an applied electric field, E, consisting of two monochromatic harmonic waves, E_1 and E_2, with corresponding frequency components, ω_1 and ω_2, it can be presented in the following form:

$$E(t) = E_1(t)e^{-i\omega_1 t} + E_2(t)e^{-i\omega_2 t} + c.c. \tag{2.5}$$

According to Equation 2.4 and Equation 2.5, we find that the second-order nonlinear polarization created in such a medium is:

$$P^{(2)} = \varepsilon_0\chi^{(2)}[E_1^2e^{-2i\omega_1 t} + E_2^2e^{-2i\omega_2 t} \tag{2.6}$$

$$+2E_1E_2e^{-i(\omega_1+\omega_2)t} + 2E_1E_2^*e^{-i(\omega_1-\omega_2)t} + c.c.] \tag{2.7}$$

$$+2\varepsilon_0\chi^{(2)}[E_1E_1^* + 2E_2E_2^*], \tag{2.8}$$

from which several familiar second-order processes are associated with the different combinations of ω_1 and ω_2. These include the first two terms of Equation 2.6, which represent SHG, the first two terms of Equation 2.7 which represent the physical processes of SFG, and DFG, and the last term of Equation 2.8 which represents *optical rectification* (OR). Here, we do not consider the complex conjugates (c.c.) of the above equation, as they do not lead to any extra processes other than the above mentioned processes.

The physical meaning of the different types of frequency conversion processes are illustrated in Figure 2.2. In all of the optical processes, energy and momentum of the photons taking part in the frequency conversion have to be conserved. The momentum conservation is also known as the *phase-matching* condition. In case of SHG, depicted in Figure 2.2(a), which can be considered special case of SFG where two photons of the same frequency are converted into a single photon at twice the frequency (2ω). SHG was first demonstrated in 1961 [4] and was the first observed nonlinear optical effect. In the SFG processes, depicted in Figure 2.2(b), two input photons (ω_1 and ω_2) traveling through the nonlinear medium, are converted into a single photon at higher

frequency ($\omega_3 = \omega_1 + \omega_2$). In the DFG processes, depicted in Figure 2.2(c), two photons of the initial beams (ω_1 and ω_3) are converted into a single photon at lower frequency ($\omega_2 = \omega_3 - \omega_1$). In the case of optical rectification, which can be considered special case of DFG, the input beam at frequency, ω, mixes with itself or another beam at the same frequency, resulting in a difference frequency, $\Delta\omega = 0$. This process was first observed by Bass *et. al.* in 1962 [5]. In addition, there is the another type of down-conversion process, OPG, where the incoming pump light (ω_3) is converted into two beams at different lower frequencies (ω_1 and ω_2), as shown in Figure 2.2(d). In practice, the OPG process is initiated by a single intense pump field, ω_3, at the input of

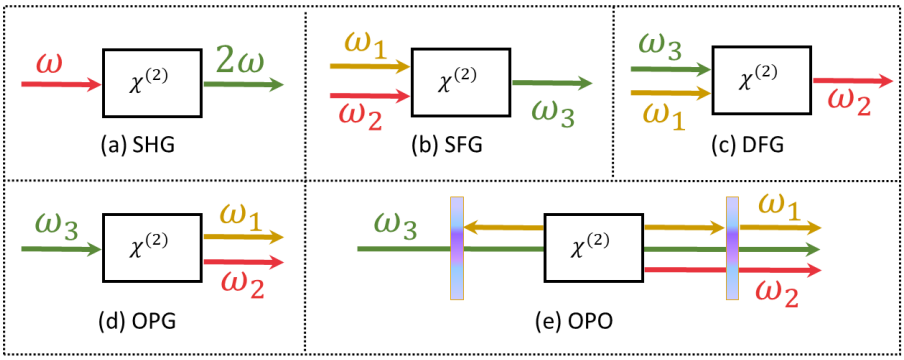

Figure 2.2: Schematic depiction of the second-order nonlinear processes.

the $\chi^{(2)}$ nonlinear material, and the pump photons generate the initial signal and idler photon pairs by the breakup of the pump photons through spontaneous parametric down conversion. This process is also referred to as parametric noise or parametric fluorescence [6,7,8]. Then, as the signal and idler photons move along with the pump in the nonlinear medium, more optical frequency down-conversion takes place from the pump photons to the signal and idler photons. The process continues in this way until power is gradually transferred from the strong pump to the initially weak signal and idler fields through the $\chi^{(2)}$ nonlinear interaction in the medium. When satisfying the phase-matching condition, as discussed later in this section, the generated signal and idler fields will undergo macroscopic amplification by continually draining power from the input pump field as they propagate through the nonlinear medium. The OPG process is a consequence of parametric fluorescence, and thus always occurs in the nonlinear material. The generated and amplified signal and idler frequencies are determined by the phase-matching condition, where the signal is generally the field

with the shorter wavelength. If the OPG process occurs within an optical cavity with resonance frequency ω_1, see Figure 2.2(e), and the gain exceeds the cavity loss, then oscillation starts, and the device is referred to as an OPO. The theory of the OPO is developed more fully later in this chapter.

2.3 Nonlinear Susceptibility

The second-order nonlinear susceptibility, $\chi^{(2)}$, is a tensor represented by 3 × 3 × 3 elements, and depends on the direction of the electric field of the optical waves involved. In the tensor notation, the second-order nonlinear polarization is:

$$P_i^{(2)} = \varepsilon_0 \chi_{ijk}^{(2)} E_j E_k \tag{2.9}$$

Here the first index, i, corresponds to the induced polarization, while the second index, j, and the third index, k, are related to the indices of the incident electric field.

Instead of the susceptibility tensor, a more common description of second-order nonlinear processes is to use the d-matrix notation [3]:

$$\chi_{ijk}^{(2)} = 2d_{ijk} \tag{2.10}$$

Clearly, d is a tensor quantity, and can be described by its tensor elements. Using Kleinman symmetry [9], i.e. all interacting frequencies are far from resonance frequency of the material, the frequencies involved can permute independently of the ijk indices. Thus, we can write the d-tensor as a 3×6 matrix, d_{im}. Conventionally, the index, m, is given by the numbering scheme outlined in Table 2.1:

	j=1	j=2	j=3
k=1	m=1	m=6	m=5
k=2	m=6	m=2	m=4
k=3	m=5	m=4	m=3

Table 2.1: Numbering convention for nonlinear optical coefficients, d.

Thus, we can describe the nonlinear polarization in the expression:

$$\begin{pmatrix} P_x(\omega_3) \\ P_y(\omega_3) \\ P_z(\omega_3) \end{pmatrix} = 2\varepsilon_0 K \begin{bmatrix} d_{11} & d_{12} & d_{13} & d_{14} & d_{15} & d_{16} \\ d_{21} & d_{22} & d_{23} & d_{24} & d_{25} & d_{26} \\ d_{31} & d_{32} & d_{33} & d_{34} & d_{35} & d_{36} \end{bmatrix} \cdot \begin{pmatrix} E_x(\omega_1)E_x(\omega_2) \\ E_y(\omega_1)E_y(\omega_2) \\ E_z(\omega_1)E_z(\omega_2) \\ E_y(\omega_1)E_z(\omega_2) + E_z(\omega_1)E_y(\omega_2) \\ E_x(\omega_1)E_z(\omega_2) + E_z(\omega_1)E_x(\omega_2) \\ E_x(\omega_1)E_y(\omega_2) + E_y(\omega_1)E_x(\omega_2) \end{pmatrix} \tag{2.11}$$

Here, the matrix components, d_{im}, are also known as the nonlinear coefficients of the material, where K is the degeneracy factor, which takes the value of 0.5 for SHG and optical rectification, and 1 for the other second-order conversion processes.

A further important consideration in relation to nonlinear frequency conversion processes is the crystal structural or spatial symmetry. For example, for inversion symmetry materials, if we change the sign of the applied electric field, *E(t)*, then the sign of the induced polarization must also be changed, which means:

$$-P^{NL}(t) = \varepsilon_0\chi^{(2)}(-E(t))^2 = \varepsilon_0\chi^{(2)}(E(t))^2 = P^{NL}(t) \tag{2.12}$$

This Equation 2.12 can only be satisfied if $\chi^{(2)}$=0. Such materials are called *centrosymmetric* materials. Therefore, all second-order nonlinear optical effects are excluded in centrosymmetric materials and are only possible in non-centrosymmetric materials.

2.4 Coupled-wave equations

If we substitute for $P^{(2)}$ and E in Maxwell's wave equation, the evolution of light through a dielectric medium without free charges and currents can be described by the wave equation:

$$\nabla^2 E = \frac{n^2}{c^2}\frac{\partial^2 E}{\partial t^2} = \frac{1}{\varepsilon_0 c}\frac{\partial^2 P^{(NL)}}{\partial t^2} \tag{2.13}$$

where $P^{(NL)}$ is the nonlinear part of the induced polarization from Equation 2.2, c is the speed of light in vacuum, and refractive index n at frequency ω is represented as:

$$n = n(\omega) = \sqrt{\frac{\varepsilon(\omega)}{\varepsilon_0}} \tag{2.14}$$

$\varepsilon(\omega)$ is the permittivity of the medium at frequency, ω, and ε_0 is the permittivity of free space. To simplify the discussion, we assume that the applied fields, E_i (i = 1, 2,

3), are infinite uniform plane waves propagating only in the z-direction, and define each field as:

$$E_i(z,t) = \frac{1}{2}\{A_i(z,\omega)exp[i(\omega t - kz)]\} + c.c. \tag{2.15}$$

Since the applied fields depend only on the coordinate, z, we can replace ∇^2 by d^2/dz^2. Generally, the wave equation holds for all involved frequency components in the mixing process, so we can obtain three separate wave equations at each frequency for wave mixing processes [3]:

$$\frac{d^2A_1}{dz^2} + 2ik_1\frac{dA_1}{dz} = \frac{-4d_{eff}\omega_1^2}{c^2}A_3A_2^*e^{-i(k_1+k_2-k_3)z} \tag{2.16a}$$

$$\frac{d^2A_2}{dz^2} + 2ik_2\frac{dA_2}{dz} = \frac{-4d_{eff}\omega_2^2}{c^2}A_3A_1^*e^{-i(k_1+k_2-k_3)z} \tag{2.16b}$$

$$\frac{d^2A_3}{dz^2} + 2ik_3\frac{dA_3}{dz} = \frac{-4d_{eff}\omega_3^2}{c^2}A_1A_2^*e^{i(k_1+k_2-k_3)z} \tag{2.16c}$$

For interactions (linear and nonlinear), using the *Slowly Varying Envelope Approximation* (SVEA)[1], where the field amplitudes vary only slowly over distances compared to a wavelength in space and the optical period in time, the wave Equation 2.16 can be simplified to the following three coupled amplitude equations:

$$\frac{dA_1}{dz} = \frac{2id_{eff}\omega_1^2}{k_1c^2}A_3A_2^*e^{-i\Delta kz} \tag{2.17a}$$

$$\frac{dA_2}{dz} = \frac{2id_{eff}\omega_2^2}{k_2c^2}A_3A_1^*e^{-i\Delta kz} \tag{2.17b}$$

$$\frac{dA_3}{dz} = \frac{2id_{eff}\omega_3^2}{k_3c^2}A_1A_2e^{i\Delta kz} \tag{2.17c}$$

where $k_j = n_j\omega_j/c$ (j=1, 2, 3) is the wave vector, Δk is wave vector mismatch represented as $\Delta k = k_1 + k_2 - k_3$, which will be discussed later in more detail, and d_{eff} is the effective nonlinear coefficient. These are the coupled-wave equations governing the parametric interaction in a dielectric medium and apply universally to any three-wave mixing process involving the second-order susceptibility. It is clear that through the effective nonlinear coefficient, d_{eff}, the amplitudes of the three fields are coupled to one another. Physically, this coupling provides the mechanism for the exchange of energy among the interacting fields as they propagate through the nonlinear medium. The energy flow direction in a given three-wave mixing process depends on the relative phase and the intensity of the input fields.

[1]The SVEA is often used because the resulting equations are in many cases easier to solve than the original equations, reducing the order of all or some of the highest-order partial derivatives.

2.5 Gain and amplification in parametric interactions

The general solution of the three coupled amplitude equations shown in Equation 2.17, are Jacobi's elliptic functions [10]. However, by using some assumption that one of the incoming wave, termed pump in our analysis, is much stronger than the other two, an analytical solution can be found. In this special simplification, which is known as the undepleted pump approximation, the pump amplitude, A_3, can be considered to be constant along the propagation direction, which means dA_3/dz=0 . In this case, the resulting coupled equation will be reduced to a two linear coupled equations with A_3 independent of z, and after some manipulation, we arrive at:

$$\frac{dA_1}{dz} = \frac{2id_{eff}\omega_1^2}{k_1c^2}A_3A_2^*e^{-i\Delta kz} \tag{2.18a}$$

$$\frac{dA_2}{dz} = \frac{2id_{eff}\omega_2^2}{k_2c^2}A_3A_1^*e^{-i\Delta kz} \tag{2.18b}$$

Taking into consideration of the initial condition, zero input idler field, $A_2(z=0)=0$, and non-zero input signal, $A_1(z=0)\neq 0$, the net fractional gain in the signal intensity after propagation through the nonlinear crystal can be derived as [2]:

$$G_1(L) = \frac{I_1(z=L)}{I_1(z=0)} - 1 = \Gamma^2L^2\frac{sinh^2[\Gamma^2L^2-(\Delta kL/2)^2]^{1/2}}{[\Gamma^2L^2-(\Delta kL/2)^2]} \tag{2.19}$$

where L is the interaction length, $I_1 = nc\varepsilon_0E_1E_1^*/2$ is the intensity, Δk is the phase-mismatch, and Γ is the gain factor defined as:

$$\Gamma^2 = \frac{8\pi^2d_{eff}^2}{c\varepsilon_0n_1n_2n_3\lambda_1\lambda_2}I_3(0) \tag{2.20}$$

Here, n is the refractive index, λ is the wavelength of the respective waves in vacuum, and $I_3(0)$ is the input pump intensity. In some situations of practical interest, the gain factor is also expressed in the form [2]:

$$\Gamma^2 = \frac{8\pi^2d_{eff}^2}{c\varepsilon_0n_0^2n_3\lambda_0^2}(1-\delta^2)I_3(0) \tag{2.21}$$

where δ is the degeneracy factor defined through:

$$1+\delta = \frac{\lambda_0}{\lambda_2}, \qquad 1-\delta = \frac{\lambda_0}{\lambda_1} \qquad (0\leq\delta\leq 1) \tag{2.22}$$

The degenerate wavelength, λ_0, is given by $\lambda_0 = 2\lambda_3$, and n_0 is the refractive index at degeneracy, with $n_0 \sim n_1 \sim n_2$ assumed. It is clear from Equation 2.21 that the parametric gain in an amplification process has a maximum value at degeneracy, where

$\delta \sim 0$, and the gain decreases for operation away from degeneracy, as $\delta \to 1$. Now, we consider the net single-pass signal gain under different pumping conditions. In the high-gain limit, where $\Gamma^2 >> (\Delta k/2)^2$, the single-pass gain reduces to:

$$G_1(L) = \frac{1}{4} exp(2\Gamma L), \tag{2.23}$$

which corresponds to the case of high-intensity, pulsed, and amplified laser pump sources. Alternatively, pumping by a CW or low-peak-power pulsed laser, this corresponds to the low-gain limit of parametric generation, with $\Gamma^2 < (\Delta k/2)^2$ or $\Delta L < 1$, the single-pass gain approximates to:

$$G_1(L) = \Gamma^2 L^2 sinc^2\{L \cdot | [\Gamma^2 - (\Delta k/2)^2] |^{1/2}\} \tag{2.24}$$

When $\Gamma^2 << (\Delta k/2)^2$, the term of inside *sinc* function will be replaced by $(\Delta kL/2)$. When near phase-matching, $\Delta k \approx 0$, and $\Gamma L << 1$, the single-pass power gain will be:

$$G_1(L) = \Gamma^2 L^2 \tag{2.25}$$

Therefore, under the phase-match condition, $\Delta k = 0$, the single-pass signal gain has a quadratic dependence on ΓL in the low-gain limit, whereas it increases exponentially with $2\Gamma L$ in the high-gain limit.

2.6 Phase-matching

Momentum conservation, or often-called the *phase-matching* condition, is a crucial requirement and widely used concept in many energy-conserving multiphoton processes including SFG, DFG, OPG, and even the extreme nonlinear optical process of high-order harmonic generation. Phase-mismatch originates from material dispersion and causes a lack of constructive interference between optical waves involved in the nonlinear processes. With an appropriate design the material, the phase-matching condition can be achieved and the energy of input wave will be transferred to the generated waves. However, if there is phase-mismatch in the nonlinear frequency conversion process, it will prevent microscopic nonlinear sources from combining constructively, resulting in destructive interference and poor generation efficiency. To overcome this limitation and improve the efficiency of frequency conversion, some compensation techniques have

been developed including the *birefringent phase-matching* and widely used *quasi-phase-matching*. Implementing each technique poses a number of challenges. Other important parameters relevant to phase-matching, such as walk-off, acceptance bandwidth and tuning characteristics will be introduced.

2.6.1 Birefringent phase-matching

From the proceeding discussion, it may be concluded that the efficiency of a nonlinear frequency conversion process depends mainly on the phase-matching condition. Mathematically, the phase-matching term is given by:

$$\Delta k = k_1 + k_2 - k_3 \tag{2.26}$$

where Δk is the wave vector mismatch, and k_1, k_2 and k_3 are the wavevectors of the signal, idler and pump beam, respectively. As mentioned in the previous section, in the parametric process, the signal is generally the wave with the shorter wavelength.

Since the nonlinear medium in general exhibits different refractive indices to the pump, signal and idler waves, the phase-matching condition, $\Delta k = 0$, is often difficult to achieve due to normal dispersion, where the refractive index is an increasing function of frequency. As a result, the condition for perfect phase-matching with collinear beams is not possible. However, for optically anisotropic materials, the refractive index depends not only on wavelength, but also on the polarization direction of the light relative to the crystal axes. This optical property also called *birefringence*, thus the phase matching is still achievable by making use of the birefringent properties displayed by certain materials. It should be noted that not all crystals display birefringence, in particular are optically isotropic, crystals belonging to the cubic crystal system such as OP-GaAs in which it is not possible to achieve phase-matching by this method.

Birefringent phase-matching (BPM) is a conventional and important phase-matching technique. In the history of nonlinear optics, an essential step toward efficient frequency conversion, taken in 1962 [4], was the use of BPM in SHG. The basic idea of BPM is that the interacting waves of different frequencies are polarized differently, so that their corresponding phase velocities can be adjusted, and thus their wave vectors can satisfy the phase-matching condition. Here, two different perpendicular polarizations, *ordinary* (o) and *extraordinary* (e) polarization are distinguished according to the crystallographic point group of the material. In addition, for uniaxial crystals, two different cases are

distinguished: *positive* and *negative* birefringent materials. In the case of a positive uniaxial crystal, the extraordinary refractive index is larger than the ordinary index, represent as $n_e > n_o$. For a negative uniaxial crystal, the opposite is true, which is $n_e < n_o$. Mathematically, the equation of the extraordinary index is given by:

$$n_e(\theta) = [\frac{sin^2\theta}{n_e^2} + \frac{cos^2\theta}{n_o^2}]^{-1/2} \tag{2.27}$$

Clearly, Equation 2.27 indicates the dependence of the extraordinary index, $n_e(\theta)$, on θ. In practical operation of parametric devices, two different types of phase-matching (type I and type II) are possible. Historically, they originate from SHG experiments [11]. Here, we cite the definition of different types for parametric processes. Assuming the process is $\omega_3 \rightarrow \omega_1 + \omega_2$, then *type I* is defined to be the case in which the two lower-frequency waves have the same polarization, while *type II* is the case where the polarizations are orthogonal. In all cases of three-wave mixing processes, the situation can be summarised as in Table 2.2, where e represents the extraordinary polarization and o is the ordinary polarization. For example, in a DFG process, using a positive

Phase-matching	Pump	Signal	Idler	Crystal Type
Type I	e	o	o	Negative birefringent
Type I	o	e	e	Positive birefringent
Type II	e	e	o	Negative birefringent
Type II	e	o	e	Negative birefringent
Type II	o	e	o	Positive birefringent
Type II	o	o	e	Positive birefringent

Table 2.2: Type I and type II phase-matching configurations for parametric process. e: extraordinary polarisation; o: ordinary polarisation.

birefringent crystal with *type I* process, the phase-matching condition can be expressed as follows:

$$\frac{n_o(\omega_3)}{\lambda_3} - \frac{1}{\lambda_1}\sqrt{\left(\frac{sin^2\theta_{pm}}{n_e^2(\omega_1)} + \frac{1-sin^2\theta_{pm}}{n_o^2(\omega_1)}\right)^{-1}} = \frac{1}{\lambda_2}\sqrt{\left(\frac{sin^2\theta_{pm}}{n_e^2(\omega_2)} + \frac{1-sin^2\theta_{pm}}{n_o^2(\omega_2)}\right)^{-1}} \tag{2.28}$$

where θ_{pm} is the phase-matching angle. By choosing a proper angle with respect to the crystal axis, phase-matching can be achieved. This is visually illustrated in Figure 2.3 for a positively birefringent crystal.

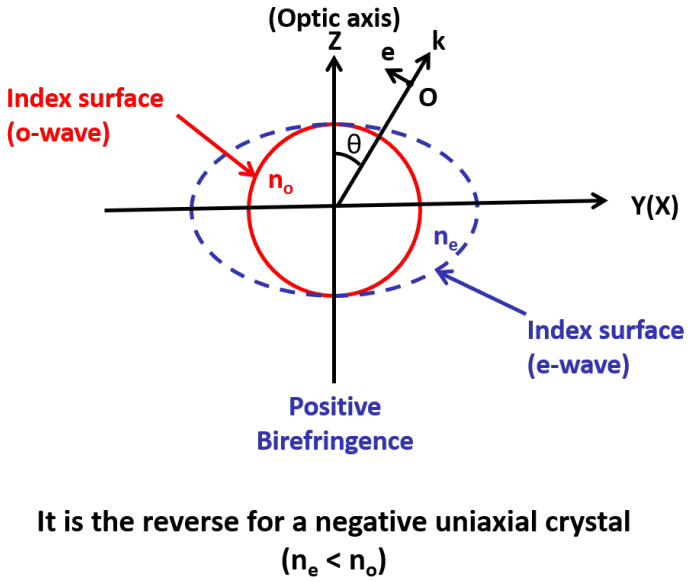

Figure 2.3: Refractive index surface in a positive uniaxaial crystal and wave vector, k.

In practice, on the other hand, such conversions suffer from an inherent limitation that is *Poynting vector walk-off*, where the direction of the beam propagation differs from the phase front direction. The propagation direction is the direction of energy flow given by the Poynting vector, while the direction of the phase front is given by the k vector. The polarization, P, is only parallel to the electric field, E, when it oscillates along the principal axis of crystal, thus the Poynting vector is often pointed at an angle to the direction of wave vector, and then the output beams will be separated. This phenomenon is also known as *spatial walk-off*. Given the limited length of the nonlinear crystal, walk off leads to a smaller spatial overlap between the interacting beams in the crystal, thus only a limited length of crystal for the parametric waves can be used and, therefore, the conversion efficiency will be reduced. In the presence of walk-off, the effective crystal length is defined as [12]:

$$L_{eff} = \frac{\sqrt{\pi}\omega_0}{\rho} \tag{2.29}$$

where ω_0 is the waist radius of the input beam. ρ is the double-refraction angle, which in the case of a uniaxial crystal is expressed as:

$$tan(\rho) = -\frac{1}{2} \mid n_e(\theta_{PM}) \mid^2 \left(\frac{1}{n_e^2} - \frac{1}{n_o^2}\right) sin(2\theta_{PM}) \tag{2.30}$$

where θ_{PM} is the phase-matching angle. It is clear from Equation 2.30 that spatial walk-off angle in birefringent phase-matching has a minimum value at $\theta_{PM} = 90°$ relative to principal axes of the nonlinear crystal, where spatial walk-off will be vanished, this is called *noncritical phase-matching* (NCPM). Otherwise, it is referred to as *critical phase-matching* (CPM). In the NCPM configuration, due to the absence of spatial walk-off, the nonlinear crystal length becomes the effective interaction length of the nonlinear optical process.

In the BPM scheme, it is possible to greatly enhance the frequency conversion efficiency by NCPM. However, it needs to be borne in mind that BPM does not allow access to all the coefficients of the second-order nonlinear susceptibility tensor [13]. In particular, in any ferroelectric crystal, the highest coefficient, d_{11}, d_{22}, and d_{33} cannot be purely solicited by BPM because this requires the interacting beams to be in different polarizations, which is not the case with the diagonal matrix elements.

2.6.2 Quasi-phase-matching

In BPM method, many desirable OPO implementations are limited by spatial walk-off, low effective nonlinear coefficient, and inconvenient phase-matching temperatures and angles. Specially, the largest nonlinear coefficient cannot be used in many cases for the frequency conversion process. An example is the well-known negative birefringent material, $LiNbO_3$, where d_{33} is the largest nonlinear coefficient, which implies that the polarizations of all three beams are the same. Unfortunately, in BPM, this coefficient cannot be used, as it is neither compatible with *type I* nor *type II* phase-matching (see Table 2.2 above). In addition, some semiconductor crystals have large nonlinearities, as well as other desirable properties such as availability in good quality and relatively large size, but phase-matching is not possible by BPM, thus alternate approaches of compensation of phase-mismatch are desirable.

For a frequency-conversion process, such as OPG or SHG, the phase-mismatch is accumulated with increasing interaction length. After travelling a short distance known as the *coherence length*, given by $L_{coh} = \pi/\Delta k$, the conversion efficiency reduces and energy flows back from the generated waves to the pump. For a crystal length much longer than the coherence length, the efficiency will behave in the way of the Maker fringes [3]. One way to avoid this conflict is to use periodically-poled nonlinear materials and take advantage of the so-called *quasi-phase-matching* (QPM). The QPM technique

was first proposed by Armstrong and Bloembergen in 1962 [10], prior to the introduction of BPM. However, it was first demonstrated in 1966 [14], after BPM was demonstrated. The basic idea of QPM is to periodically flip the sign of the nonlinear susceptibility with a period twice the coherence length, i.e., the sign of $\chi^{(2)}$ tensor is modulated along the propagation direction of the beams by means of electric field poling, as illustrated in Figure 2.4. This modulation will introduce extra complexity to the coupled-wave field equations, which provides a net compensation for the phase-mismatch between the interacting waves. Consequently, the conversion efficiency increases quasi-continuously with interaction length.

Mathematically, the periodic inversion of the nonlinear coefficient is described by a Fourier series. In order to be valid for QPM, the coupled-wave equations, Equation 2.16, need to be slightly adjusted, where the term $d_{eff}(z)$ now shows a z dependency. With a periodic change of the sign of the nonlinear coefficient, the $d_{eff}(z)$ term can simply be described by [1]:

$$d_{eff}(z) = d_{eff} sign[cos(2\pi z/\Lambda)] \tag{2.31}$$

Using Fourier expansion, the effective nonlinear coefficient, d_{eff}(z), can be written in the following way:

$$d_{eff}(z) = d_{eff} \sum_{m=-\infty}^{\infty} G_m e^{iK_m z} \tag{2.32}$$

where the grating vector, K_m, is given by:

$$K_m = \frac{2\pi m}{\Lambda} \tag{2.33}$$

Here, Λ is the period of the grating, and the Fourier coefficients, G_m, is given by:

$$G_m = \frac{2}{m\pi} sin(m\pi D) \tag{2.34}$$

where D is the duty cycle, defined by the length of reversibly poled domain divided by the grating period, Λ. Usually, the duty cycle is twice the coherence length, so that D = 0.5, and, therefore, the coefficients, G_m, are given by:

$$G_m = \frac{2}{m\pi} sin(m\pi/2) \tag{2.35}$$

where m refers to the order of the QPM. For first-order QPM, m=1, with a 50% poling duty cycle, the effective nonlinear coefficient can be simplified as:

$$d_Q = \frac{2}{\pi} d_{eff} \tag{2.36}$$

And now the effective phase-mismatch parameter is the summation of the dispersion phase-mismatch and an artificial phase-mismatch, and can be written as:

$$\Delta k_Q = k_3 - k_1 - k_2 - \frac{2\pi}{\Lambda} \tag{2.37}$$

To achieve efficient QPM, the modulation period can thus be chosen such that Δk_Q=0, and so phase-matching will be obtained.

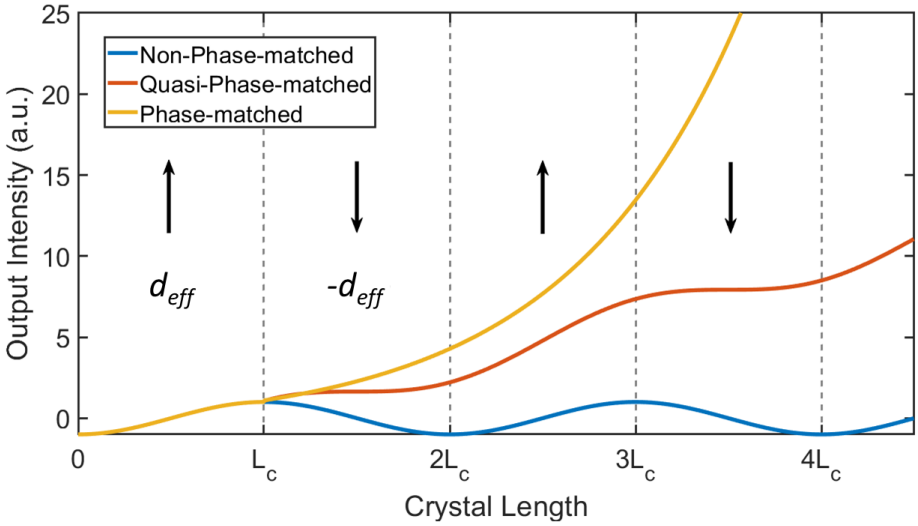

Figure 2.4: Intensity of output waves in a parametric interaction for perfect (birefringent) phase-matching in yellow, quasi-phase-matching in red, and no phase-matching in blue.

For a QPM device, any interaction within the transparency range of the material can be noncritically phase-matched at a specific temperature, even interactions for which BPM is impossible. Another key advantage of this method is that the polarization of interacting waves can be chosen so that coupling occurs through the largest element of the $\chi^{(2)}$ tensor. For example, in PPLN, one can use the largest nonlinear coefficient (d_{33}) by choosing the pump, signal, and idler wave polarizitions in parametric process to be parallel to the z axis ($e \rightarrow e+e$), yielding a gain enhancement over the birefringently phase-matched process of $(2d_{33}/\pi d_{31})^2 \approx 20$. In addition, the extraordinary polarization experiences lower absorption loss through the transmission window of the material than the corresponding ordinary polarization, which can further enhance efficiency.

2.7 Acceptance bandwidth

As introduced from the preceding discussion, we know that the parametric interaction process is strongly dependent on the phase-matching term, $\Delta k = k_3 - k_1 - k_2$ (Equation 2.26). The conversion efficiency reaches maximum at $\Delta k = 0$, and decreases rapidly with increasing wave-vector mismatch when $\Delta k \neq 0$. Thus, it is important to quantify the consequence of variation of Δk from 0, due to variations of wavelength, angle, or temperature.

As described by Equation 2.24, the single-pass gain is a $sinc^2$ function at the low-gain limit of parametric generation. Since the $sinc^2$ curve will decrease by a factor of 2 when $\Delta kL/2 = \pm 1.39$, see Figure 2.5, thus the acceptance bandwidth is the deviation, $\Delta\xi$, of the dispersive parameter, $\xi(\xi = \lambda, \theta, T)$, leading to a phase-mismatch variation, Δk, from 0 to $2.78/L$, where L is the crystal length. Solving for the wavelength range, $|\Delta k| < 2.78/L$, yields the phase-matching bandwidth.

Mathematically, the acceptance bandwidth can be determined by expressing the phase-mismatch term, Δk, as a Taylor series, through first order, as a function of dispersive parameter, ξ, and solving for $\Delta\xi$:

$$\Delta k = \frac{\partial(\Delta k)}{\partial \xi} \cdot \delta\xi + \frac{1}{2}\frac{\partial^2(\Delta k)}{\partial \xi^2} \cdot (\delta\xi)^2 + \cdots \tag{2.38}$$

For example, DFG process in a QPM nonlinear material, the phase-mismatch is given by:

$$\Delta k = 2\pi\left[\frac{n(\lambda_3)}{\lambda_3} - \frac{n(\lambda_1)}{\lambda_1} - \frac{n(\lambda_2)}{\lambda_2} - \frac{1}{\Lambda}\right] \tag{2.39}$$

Here, λ_3, λ_1 and λ_2 refers to the pump, signal and DFG wavelengths, and $n(\lambda_3)$, $n(\lambda_1)$ and $n(\lambda_2)$ are the corresponding refractive indices, respectively. Assuming the process is phase-matched at signal wavelength, λ_2, when the input signal wavelength changes by $\delta\lambda_1$, through the first order in $\delta\lambda_1$, the phase-mismatch is described by:

$$\Delta k = \frac{2\pi\delta\lambda_1}{\lambda_1}\left[\frac{n(\lambda_1)}{\lambda_1}\bigg|_{\lambda_1} - \frac{\partial(n(\lambda_1))}{\partial\lambda_1}\bigg|_{\lambda_1}\right] \tag{2.40}$$

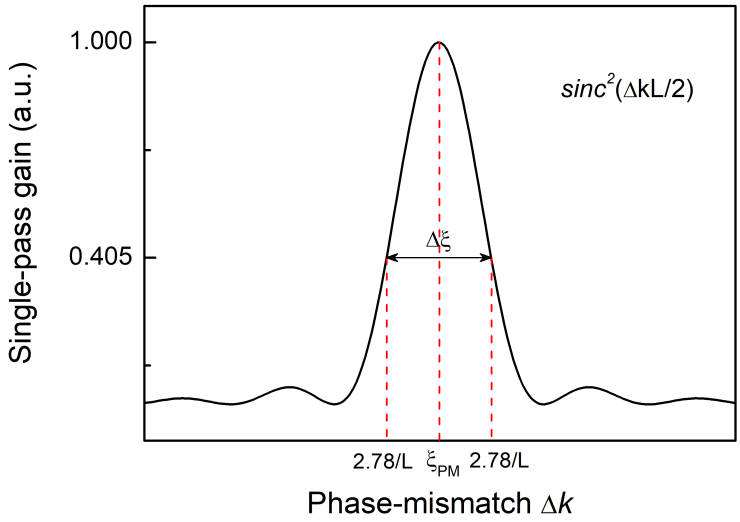

Figure 2.5: Single-pass gain as a function of phase-mismatch, Δk. ξ: dispersive parameter of the refractive indices. ξ_{PM} is the value satisfying phase-matching; $\Delta\xi$ is the full-width of the curve at 0.405 of the maximum.

Using the condition of -2.78$/L < \Delta k <$ 2.78$/L$, we finally obtain the spectral acceptance bandwidth:

$$\delta\lambda_{FWHM} = \frac{0.885\lambda_1/L}{\left[\frac{n(\lambda_1)}{\lambda_1}\bigg|_{\lambda_1} - \frac{\partial(n(\lambda_1))}{\partial\lambda_1}\bigg|_{\lambda_1}\right]} \tag{2.41}$$

Here, L is the length of the nonlinear crystal. Similarly, assuming the process is phase-matched at temperature T_0, and then the temperature acceptance bandwidth can be derived as:

$$\delta T_{FWHM} = \frac{0.885/L}{\left[\frac{1}{\lambda_3}\frac{\partial(n(\lambda_3))}{\partial T}\bigg|_{T_0} - \frac{1}{\lambda_1}\frac{\partial(n(\lambda_1))}{\partial T}\bigg|_{T_0} - \frac{1}{\lambda_2}\frac{\partial(n(\lambda_2))}{\partial T}\bigg|_{T_0}\right]} \tag{2.42}$$

2.8 Dispersion

In frequency conversion processes involving ultrashort pulses, where more than two waves interacts with each other while propagating though the nonlinear medium, dispersion characteristics of the material are very important. Waves at different frequencies

propagate at different group velocities and, hence, the interacting pulses can become separated after certain distance in the crystal. If this happens, the temporal effective interaction length is reduced. In order to evaluate this effect, an important temporal parameter is the *group velocity mismatch* (GVM) between the interacting waves in the optical medium.

$$\Delta v_g^{-1} = \left(\frac{1}{v_{g,i}} - \frac{1}{v_{g,j}} \right) \tag{2.43}$$

where $v_{g,i}$ and $v_{g,j}$ are the group velocity of wave i and j, respectively, defined as:

$$v_{g,i} = \frac{c}{n_i - \lambda_i \frac{\partial n_i}{\partial \lambda_i}} \tag{2.44}$$

The temporal effective interaction length, L_{eff}, for wave i or j can be calculated by:

$$L_{eff} = \frac{\tau_1}{\mid \Delta v_g^{-1} \mid} \tag{2.45}$$

where τ_1 is the incident pump pulse duration, and it is assumed that i and j waves have similar pulse duration.

Another important temporal effect that estimates the pulse broadening is the *group velocity dispersion* (GVD). The most important feature of the GVD values is the signal value, as this is the parameter governing whether or not the resonant wave will see a positive or negative GVD. This effect can be calculated by evaluating the dispersion parameter, which is defined as:

$$\beta = \frac{\partial^2 k}{\partial \omega^2} = \frac{\lambda^3}{2\pi c^2} \frac{\partial^2 n}{\partial \lambda^2} \tag{2.46}$$

A closely related yet independent quantity is the *group delay dispersion* (GDD), defined such that group velocity dispersion is the group delay dispersion per unit length. GDD is commonly used as a parameter in characterizing layered mirrors, where the group velocity dispersion is not particularly-well defined, yet the chirp induced after bouncing off the mirror can be well-characterized. The units of group delay dispersion are $[\text{time}]^2$, often expressed in fs^2.

2.9 Optical parametric oscillator

An *optical parametric oscillator* (*OPO*) is a device that converts an input laser wave (called "pump") with frequency ω_3 into two output waves of lower frequency (ω_1, ω_2) by means of second-order nonlinear optical interaction, as illustrated in Figure 2.6. The OPO consists essentially of an optical resonator and a nonlinear optical crystal. In the OPO, the initial idler and signal waves are taken from background waves, which are always present. Then, pump wave is spontaneously down-converted to two lower frequency waves called signal, ω_1, and idler, ω_2, conserving the energy ($\omega_3 = \omega_1 + \omega_2$). Although conservation of the energy permits any signal wavelength with frequency from 0 to ω_3 to be radiated in any direction, the signal and idler pair that is in practice generated at frequency and direction that yields the optimum phase-matching condition (Δk=0).

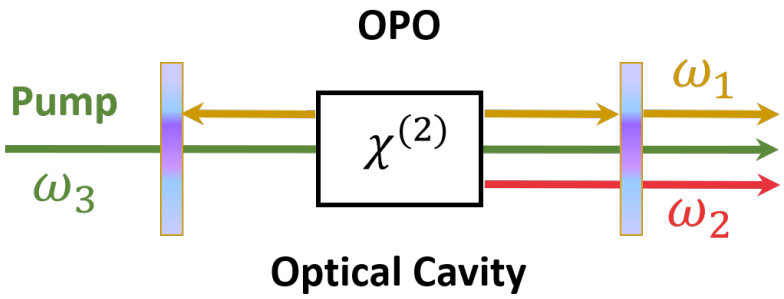

Figure 2.6: Schematic of an OPO.

In the next step, the pump wave mixes with the resonating wave and results in amplification of the signal and the idler fields through OPA. The optical gain in an OPO is instantaneous, meaning that the gain is only available in the presence of the pump. The single-pass parametric gain in the nonlinear crystal can be calculated with the coupled-waves equations, assuming undepleted pump, zero initial idler, and non-zero initial signal. When phase-matching is perfectly satisfied, $\Delta k = 0$, this gain can be simplified as:

$$G_s(L) = sinh^2(\Gamma L) \tag{2.47}$$

For low gains ($\Gamma L \leq 1$) as:

$$G_s(L) = \Gamma^2 L^2 \tag{2.48}$$

and for high gains ($\Gamma L >> 1$) as:

$$G_s(L) = \frac{1}{4} e^{2\Gamma L} \tag{2.49}$$

where Γ is:

$$\Gamma = \sqrt{\frac{8\pi^2 d_{eff}^2}{n_1 n_2 n_3 c \varepsilon_0 \lambda_1 \lambda_2} I_3(0)(1-\delta^2)} \tag{2.50}$$

where δ is the degeneracy factor defined by Equation 2.22.

2.9.1 OPO resonance configurations

The main requirement for the successful operation of an OPO is the attainment of sufficient gain at the parametric waves for a given pump power to overcome parasitic losses in the cavity originating from scattering, parasitic reflection, and any absorption in the crystal. This is achieved by providing feedback at the generated waves using various configurations of the optical cavity, as summarized in Figure 2.7. These configurations depends on the number of resonating waves that oscillates inside the cavity, which is controlled with the reflectivity of the mirrors forming the optical cavity.

In *singly-resonant oscillator* (SRO), only one of the generated waves, signal or idler, oscillates in the cavity while the other wave is extracted from the cavity together with the remaining undepleted pump wave. With sufficient intracavity power, it is also possible to extract part of the resonant wave power. In *doubly-resonant oscillator* (DRO), both the generated waves oscillate in the cavity, a small part of the power of one or both waves from the optical cavity is extracted using suitable output coupler (OC). *Pump-enhanced SRO* ($PE-SRO$) is a special case of the SRO where a small part of the pump is also resonated in the cavity in order to reduce the threshold of the OPO. In *triply-resonant oscillator* (TRO), all the three interacting waves oscillate in the optical cavity. DRO, PE-SRO and TRO do have lower threshold pump power in comparison to SRO. However, stable operation is challenging due to the requirement of

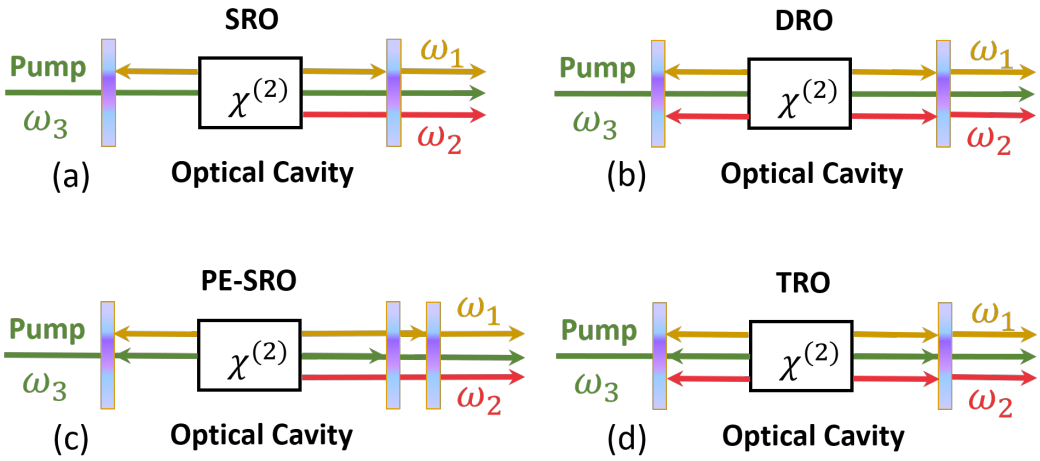

Figure 2.7: OPO resonance configurations: (a) singly-resonant oscillator (SRO), (b) doubly-resonant oscillator (DRO), (c) pump-enhanced singly-resonant oscillator (PE-SRO) and (d) triply-resonant oscillator (TRO).

simultaneous fulfilment of cavity-resonance condition for multiple wavelengths. SROs generally provide stable performance with single-frequency output.

2.9.2 Wavelength tunability

OPOs are known for their wide wavelength tunability covering essential wavelength gaps which commercial lasers fail to cover. Using the energy conservation ($\omega_3 = \omega_1 + \omega_2$) and phase-matching ($k_3 = k_1 + k_2$), it is observed that the generated idler frequency depends on the refractive indices of the three interacting waves, n_3, n_1 and n_2

$$\omega_2 = \frac{n_3 - n_1}{n_2 - n_1}\omega_3 \tag{2.51}$$

In BPM crystals, wavelength tuning is obtained by changing the angle between the optic axis of the crystal and the direction of propagation by tilting the nonlinear crystal. In QPM, tuning can be achieved by changing the grating period of the crystal. In either cases, the temperature of the crystal can also be used to tune the output wavelengths. In femtosecond OPOs, wavelength tuning is also observed by control of cavity length.

2.9.3 Cavity design

In order to have efficient OPO operation, a good narrow linewidth pump source, proper selection of nonlinear material and a well designed optical resonator cavity are of utmost importance. The most common cavity designs are presented in Figure 2.8.

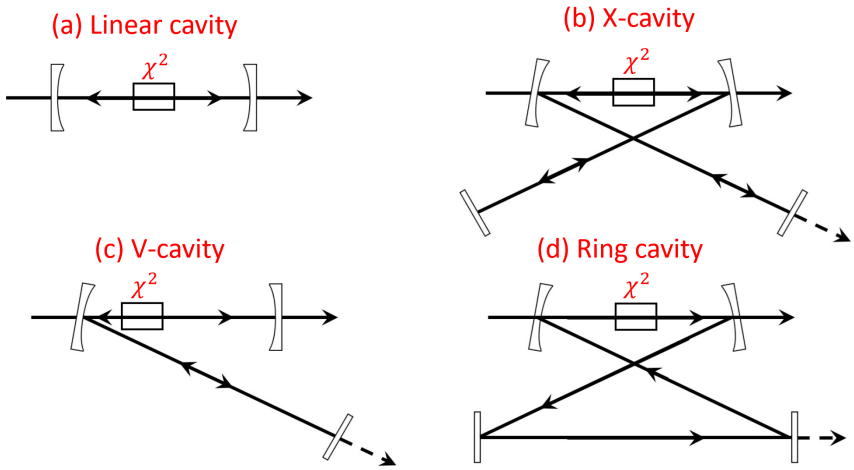

Figure 2.8: OPO cavity designs: (a) Linear cavity, (b) X-cavity, (c) V-cavity, and (d) ring cavity.

The linear, X- and V-cavities are standing-wave cavities, while the ring cavity is a travelling-wave cavity. Standing-waves cavities are favourable for ultrafast OPOs, because it is easier to synchronize the pump with the resonating wave. The standing-wave cavities also have some disadvantages for single-pass pumping designs, as the resonating wave sees gain only in one direction, but suffers losses while traversing the crystal in both directions. The travelling-wave cavities are better as no pump radiation is reflected back into the laser, so no requirement for an optical isolator and also the resonating wave experiences gain in every pass through the nonlinear crystal.

In synchronous pumping, the cavity length of the OPO has to match the repetition-rate of the pump laser. And a very efficient OPO cavity should have the confocal parameter of the pump beam, b_p, equal to that of the resonant beam, $b_s \sim b_p$. Further informationson the stability criteria and transformation matrices can be found in [2].

References

[1] R. W. Boyd, *Nonlinear Optics*, (Academic Press, 2007).

[2] M. Ebrahim-Zadeh and M. H. Dunn, "Optical parametric oscillators," in *Handbook of Optics*, 2nd ed., Vol. IV (McGraw-Hill, 2000), pp. 1–72.

[3] R. L. Sutherland, *Handbook of Nonlinear Optics*, (Marcel Dekker, 2003).

[4] P. A. Franken, A. E. Hill, C. W. Peters, and G. Weinreich, "Generation of optical harmonics," *Phys. Rev. Lett.* **7**, 118 (1961).

[5] M. Bass, P. A. Franken, J. F. Ward, and G. Weinrich, "Optical rectification," *Phys. Rev. Lett.* **9**, 446 (1962).

[6] J. P. Gordon, W. H. Louisell, and L. R. Walker, "Quantum fluctuations and noise in parametric processes II," *Phys. Rev.* **129**, 481 (1963).

[7] W. H. Louisell, A. Yariv, and A. E. Siegman, "Quantum fluctuations and noise in parametric processes I," *Phys. Rev.* **124**, 1646 (1961).

[8] W. G. Wagner, and R. W. Hellwarth, "Quantum noise in a parametric amplifier with lossy modes," *Phys. Rev.* **133**, A915 (1964).

[9] D. A. Kleinman, "Nonlinear dielectric polarization in optical media," *Phys. Rev.* **126**, 1977 (1962).

[10] J. A. Armstrong, N. Bloembergen, J. Ducuing, and P. S. Pershan, "Interactions between light waves in a nonlinear dielectric," *Phys. Rev.* **127**, 1918 (1962).

[11] J. Q. Yao, and T. S. Fahlen, "Calculations of optimum phase match parameters for the biaxial crystal $KTiOPO_4$," *J. App. Phys.* **55**, 65-68 (1984).

[12] W. Koechner, *Solid-state laser engineering Vol. I*, (Springer, 2013).

[13] B. Boulanger, and J. Zyss, "Nonlinear optical properties," *International Tables for Crystallography* **500**, 181-222 (2006).

[14] G. D. Boyd, and C. K. N. Patel, "Enhancement of optical second-harmonic generation (SHG) by reflection phase matching in ZnS and GaAs," *Appl. Phys. Lett.* **8**, 313-315 (1966).

3

Narrow-linewidth near-degenerate optical parametric oscillators

This chapter constitutes the following publication:

1. **B. Nandy**, S. Chaitanya Kumar, J. C. Casals, H. Ye, and M. Ebrahim-Zadeh, "Tunable high-average-power optical parametric oscillators near 2 μm," *J. Opt. Soc. Am. B* **35**, C57-C67 (2018).

3.1 Backround and motivation

The spectral region near 2 μm is well known for the high absorption by water and shallow penetration depth of ~0.4 nm, which is useful for various clinical applications [1]. Tunable sources near 2 μm are also of interest due to their utility in applications such as speckle-imaging [2, 3], eye-safe differential absorption lidar [4, 5], range finding [6], coherent Doppler wind lidar [7], and terahertz (THz) difference-frequencygeneration (DFG) [8]. Wavelength generation in the 2 μm region has been achieved using Ho^{3+}-doped, Tm^{3+}-doped, or Tm^{3+}:Ho^{3+} co-doped fiber lasers [9, 10], mode-locked Tm:CaYAlO4 (Tm:CYA) lasers [11], near-degenerate optical parametric oscillators (OPOs) [12], and, more recently, intracavity OPOs in a two-crystal walk-off compensation scheme [13]. Laser sources at ~2 μm and beyond are also necessary for pumping long-wave mid-infrared (mid-IR) OPOs and DFG sources based on non-oxide nonlinear materials such as $ZnGeP_2$, $AgGaS_2$, $AgGaSe_2$, and quasi-phase-matched orientation-patterned gallium arsenide (OP-GaAs) [12, 14-17]. Such mid-IR materials

offer high nonlinearity and wide transparency into the deep mid-IR, but suffer from two-photon absorption at wavelengths below ~2 μm. Laser sources in such long-wave mid-IR regions are essential for high-resolution spectroscopy, trace gas detection, and environmental sensing in the mid-IR molecular fingerprint region [18]. Currently, commercially available laser sources in the ~2 μm region are based on Tm^{3+}/Ho^{3+}-doped solid-state and fiber lasers, often powerhungry and requiring water-cooling for stable high-power operation, while relying on passive or active acousto-optic Q-switching, typically at fixed repetition rates [19-21].

An alternative approach for efficient and cost-effective generation of tunable laser pulses near 2 μm is to use OPOs pumped by widely available, well-established, and low-cost Nd/Yb-based laser technology at 1.064 μm. This approach has been previously demonstrated in nanosecond OPOs, where by deploying volume Bragg gratings, narrowband radiation at a fixed wavelength near 2 μm has been generated using Q-switched Nd:YAG solid-state pump lasers at 1.064 μm [12, 22]. On the other hand, in picosecond operation, the use of a diffraction grating has enabled the generation of similarly narrowband radiation at a fixed wavelength near 2 μm in a synchronously pumped OPO using a mode-locked Ybfiber laser at 1.064 μm [23]. Here we report high-averagepower, high-repetition-rate nanosecond and picosecond OPOs with wavelength tunability near ~2 μm using this approach by deploying Nd/Yb-doped solid-state and fiber lasers at 1064 nm as the pump source and MgO-doped lithium niobate (MgO:PPLN) as the nonlinear gain crystal. The demonstrated OPOs operate close to degeneracy, where the output spectrum and bandwidth are controlled by incorporating two different wavelength selection elements, a prism in nanosecond OPO, and a diffraction grating in picosecond OPO. The technique allows practical OPO operation at high average powers, with good spectral and spatial beam quality, and high output power stability, over an extended tuning range of 1880–2451 nm, including the degenerate wavelength of 2128 nm.

3.2 High-average-power high-repetition-rate nanosecond OPO near 2 μm

We have developed a high-repetition-rate nanosecond near-degenerate OPO tunable near 2.1 μm by using a Q-switched Nd: YAG laser at 1064 nm as the pump source. The OPO deploys MgO:PPLN as the nonlinear crystal and an intracavity prism for spectral

control, output coupling, and output power stabilization. Such a technique has been previously reported in pulsed OPOs in a singly resonant oscillator (SRO) configuration away from degeneracy [24]. Here, we deploy this approach in a doubly resonant oscillator (DRO) operating close to degeneracy, where we demonstrate wavelength tunability across 1880–2128 nm in the signal and 2128–2451 nm in the idler, thus covering ~571 nm across the entire spectral range of 1880–2451 nm, including the degenerate wavelength of 2128 nm. We also show that the deployment of the intracavity prism enables effective control of the output spectrum and stabilization of the output power in the DRO near or away from degeneracy.

3.2.1 Experimental setup

The schematic of the experimental setup for the tunable ~2 μm OPO is shown in Figure 3.1. The OPO is pumped by a high-repetition-rate Q-switched Nd:YAG laser (Bright Solutions, Sol) delivering up to ~30 W of average power in linear polarization with a variable repetition rate from 20 to 100 kHz. The laser operates at a central wavelength of 1064 nm with a full-width at half-maximum (FWHM) bandwidth of ~0.2 nm and exhibits spectral jitter of ~1 nm over 30 s. For pumping the OPO, we chose a fixed repetition rate of 80 kHz in order to avoid any optical damage to the MgO:PPLN crystal caused by increasing pulse energy fluence at lower repetition rates. At 80 kHz repetition rate, the pump pulses have a FWHM duration of ~23 ns. Also shown in the inset of Figure 3.1 is a laboratory photograph of the OPO incorporating an uncoated intracavity prism (P) for spectral control and output coupling. The pump power is adjusted by the combination of a half-wave plate (HWP) and a polarizing beam-splitter (PBS). The pump beam polarization is adjusted for optimum phase-matching in the MgO:PPLN crystal under type-0 (e $\Rightarrow$ ee) interaction. After preparation of the pump beam for systematic input power control and polarization, it is focused to a waist radius of w0 ~ 300 μm at the center of the crystal, which is 50-mm-long and incorporates a single grating period of Λ=32.16 μm. The crystal end-faces are antireflection (AR)-coated for high transmission (R $<$ 0.5%) at 1064 nm and over 2050–2150 nm. The crystal is mounted in an oven providing temperature control from 32 °C to 100 °C with a stability of 0.1 °C, thus covering OPO operation through wavelength degeneracy.

The OPO is configured in a linear standing-wave cavity with an input plane mirror, M_1, which is highly transmitting for the pump ($T > 90\%$) at 1064 nm and highly reflect-

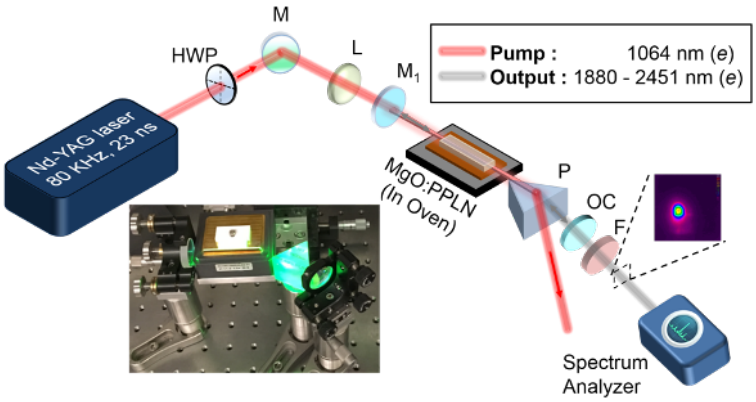

Figure 3.1: Schematic of the experimental setup for the intracavity prism-coupled tunable 2 μm source. HWP, half-wave plate; M, mirrors; L, lens; M_1, input plane mirror; P, TF3 prism; OC, output coupler; F, filter. Inset: visualization of the actual setup.

ing ($R > 99\%$) over 1800–2150 nm, resulting in OPO operation in a DRO configuration near degeneracy. The plane output coupler (OC) has varying transmission ($T \sim 60\%$ – 90%) over the OPO tuning range. Owing to the large parametric gain bandwidth near degeneracy, an uncoated TF3-glass prism (apex angle: 60.8°) is incorporated within the OPO cavity for wavelength selection, linewidth control, and spectral tuning around ~2 μm. The TF3 glass has a refractive index of ~1.7 and high transmittance ($T > 94\%$) in the 2 μm spectral region. The PPLN crystal was oriented for p-polarization on the prism. The total single-pass optical path length of the OPO cavity is ~165 mm, allowing ~21 round-trips of the signal and idler parametric waves over the ~23 ns duration of the pump pulse. The undepleted pump exits the cavity through the prism, P, at a different angle from the signal and idler waves, and is dumped onto a beam block, ensuring single-pass pumping of the prismcoupled OPO. A long-pass filter, F, with >90% transmission above 1.65 μm is used to extract the total output power (signal plus idler) from the pump. A second filter with high transmission ($T > 95\%$) over 1300–2000 nm is used to extract signal wavelengths up to ~2 μm, beyond which the signal and idler begin to approach degeneracy.

3.2.2 Device tuning and characterization

We initially investigated the tuning characteristics of the OPO. Wavelength tuning in the prism-coupled OPO was achieved by varying the crystal temperature. We first

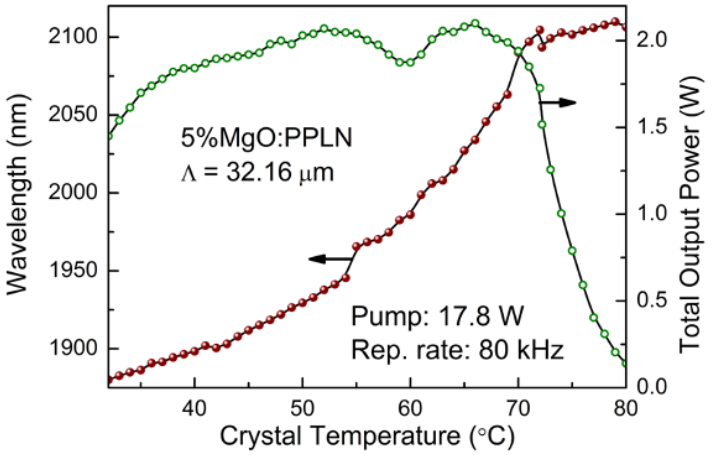

Figure 3.2: Signal wavelength tuning range and total output power generated from the prism-coupled nanosecond OPO. The solid curves are a guide to the eye.

studied temperature tuning of the OPO together with the total average output power variation across the tuning range for a fixed prism incidence angle of ~60° in the cavity. By varying the temperature of the MgO:PPLN crystal over 32 °C–81 °C, we were able to tune the generated signal across 1880–2128 nm, together with the corresponding idler across 2451–2128 nm, resulting in a total (signal plus idler) tuning over 571 nm. The results are shown in Figure 3.2, where the solid circles represent the measured signal wavelengths, while the hollow circles correspond to the total average output power from the OPO as a function of crystal temperature. The measurements were performed for a fixed input average pump power of 17.8 W (corresponding to a pump pulse energy of 0.22 mJ), and the power data are not corrected for the transmission loss (~10%) of the filter, F. As can be seen, the total average output power from the OPO remains nearly constant at ~2 W over the signal wavelength range of 1898–2090 nm (corresponding to a crystal temperature of 40 °C–70 °C), with the total OPO output power (pulse energy) increasing from 1.45 W (18.1 μJ) to 2.1 W (26.3 μJ) as the crystal temperature is increased from 32 °C to 66 °C. However, further increasing the temperature up to 81 °C results in a decline in output power down to 0.14 W (1.75 μJ), due to the broadening of the signal bandwidth towards degeneracy. As a result of the dispersion through the intracavity prism, an increasingly smaller fraction of total signal

spectrum can be supported by the cavity as the OPO is tuned towards degeneracy, thus leading to a sharp decline in the output power. The recorded OPO average output power (pulse energy) of ~2 W (25 μJ) at 55 °C corresponds to a measured signal power (pulse energy) of ~0.9 W (11.3 μJ) at 1965 nm and an estimated idler power (pulse energy) of 1.1 W (14 μJ) at 2320 nm. The average power of 2.1 W from the OPO represents a single-pass conversion efficiency of 11.84% and photon conversion efficiency of 10.7% and 13% for the signal and idler, respectively. By deploying an AR-coated intracavity prism for wavelength selection, further improvements in OPO output power and efficiency are expected. Figure 3.3 shows the phase-matched temperature tuning of the OPO together with the theoretical calculation. The measurements were performed using an InGaAs spectrometer (StellarNet RED-Wave NIRX-SR-100 T2 BW) with a resolution of about 35 nm. The solid circles represent the experimentally measured signal wavelengths, while the hollow circles are the corresponding idler wavelengths estimated from energy conservation. The solid curves are the theoretical calculations using the relevant Sellmeier equations for MgO:PPLN [25]. The discrepancy between the experimental data and theoretical calculations is attributed to the limited resolution of the spectrometer. Further, the relatively flat wavelength response as a function of the temperature close to degeneracy is due to the broad temperature acceptance bandwidth of ΔT = 14°C at a phase-matching temperature of 78°C, as shown in the inset of Figure 3.3, enabling degenerate operation of the OPO around 2128 nm.

We also recorded the signal spectrum over the entire temperature tuning range of the prism-coupled OPO at fixed prism incidence angle of ~60°. The measurements were performed using the same InGaAs spectrometer used for temperature tuning measurements, with a resolution of 15 nm in the ~2 μm region. The results are shown in Figure 3.4(a), confirming signal tuning from 1880 nm to degeneracy at 2128 nm, for a change in the MgO:PPLN crystal temperature from 32 °C to 78.5 °C. The spectral stability of the degenerate output at the temperature of 78.5 °C was also recorded over 1 hour, and the center wavelength was found to be stable to within ±2 nm with 0.1% rms, as shown in Figure 3.4(b). The corresponding FWHM bandwidth at degeneracy was also measured to be stable within ±3 nm with 6.2% rms over the same period, as shown in Figure 3.4(c). In these experiments, the measurement accuracy was constrained by the limited resolution of the spectrometer.

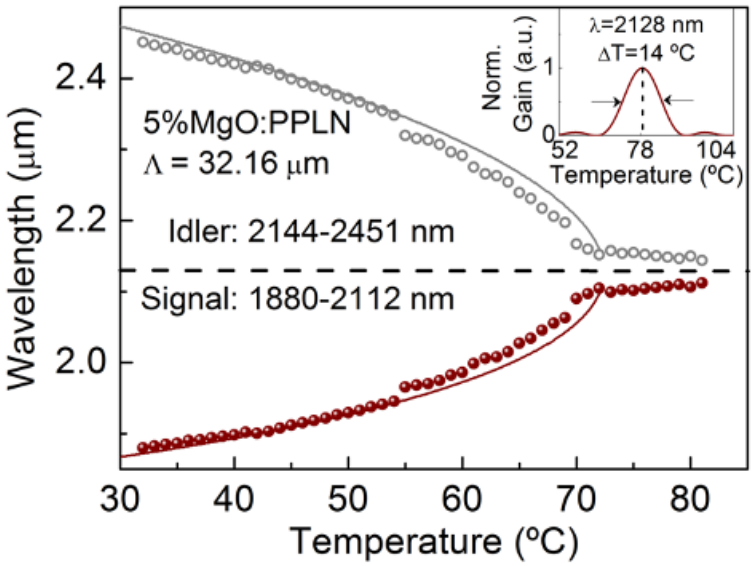

Figure 3.3: Wavelength tuning of the OPO. The filled and hollow circles represent the experimental data, while the solid curve is the calculated tuning range. Inset: temperature acceptance bandwidth for degenerate operation at 2128 nm.

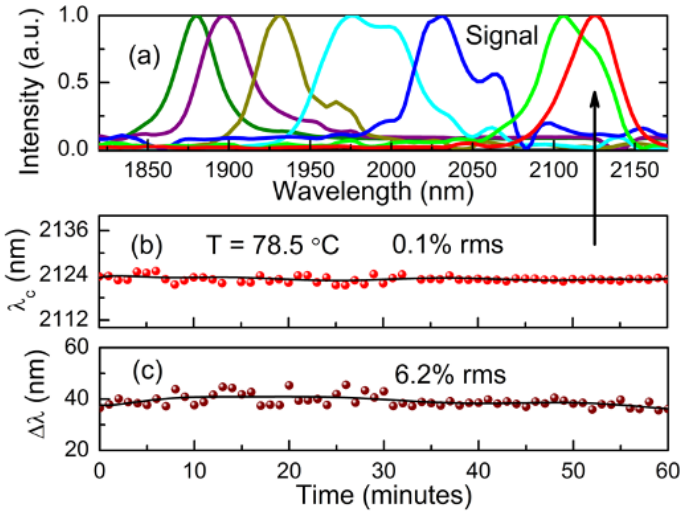

Figure 3.4: **(a)** Signal spectrum over the entire tuning range of the OPO. **(b)** Spectral stability over 1 hour measured near degeneracy. **(c)** Spectral bandwidth stability over 1 hour measured near degeneracy.

In order to determine the spectral quality of the prism-coupled OPO with higher accuracy, we further constructed a home-made grating spectrometer, and performed spectral measurements close to wavelength degeneracy. The device comprised of a 420

lines/mm diffraction grating mounted on a rotation stage with 0.01° angular precision and a sensitive power meter. The degenerate OPO output at a crystal temperature of 78.5 °C was filtered using a 1.65 μm cut-on filter and collimated using a f=150 mm lens before entering the spectrometer. The spectral components in the OPO output are separated upon reflection from the grating, and are then focused onto a slit and recorded using a power meter. For this arrangement, we can calculate the first-order diffraction angle by using the grating equation,

(3.1)

where d is the spacing between two adjacent grooves on the diffraction grating, a is the angle of incidence, b is the diffraction angle, Δx is the change in the incidence angle corresponding to the rotation of the diffraction grating, m is diffraction order, and λ is the central wavelength of the incident beam. For our device, d = 2.38μm, a = 40.22°, λ = 2.128μm, m = 1, and b is calculated to be 14.38°. Using this equation, we can ensure the calibration of the grating spectrometer. By changing Δx, using the rotation stage on which the grating is mounted, and measuring the power, the spectral intensity as a function of wavelength is recorded. The measured FWHM spectral bandwidth is limited by the resolving power of the diffraction grating, which is given by

$$R = m \times N = \lambda/\Delta\lambda \tag{3.2}$$

where m is the diffraction order, N is the total number of grooves illuminated on the surface of the grating from the incident laser, and $\Delta\lambda$ is the resolution limit. The resolving power, R, is a measure of the ability of grating to separate adjacent spectral lines of average wavelength, λ. In our case, the measured input beam diameter is ~2.5 mm, resulting in a calculated beam size of 3.3 mm on the grating surface, for an incidence angle of a=40.22°, covering 1386 grooves. Considering λ=2128 nm, the limit of resolution is calculated to be $\Delta\lambda$=1.5 nm, while the wavelength scanning step is estimated to be 0.1 nm for a minimum angular increment of 0.01° on the grating rotation stage. By using the home-built spectrometer, we further studied the OPO output spectrum across the tuning range near degeneracy by varying the crystal temperature from 71 °C to 78.5 °C, corresponding to the degenerate wavelength of ~2128 nm. The results are shown in Figure 3.5, where Δ represents the separation between the signal and idler peaks. It can be seen that, away from degeneracy there are two distinct signal

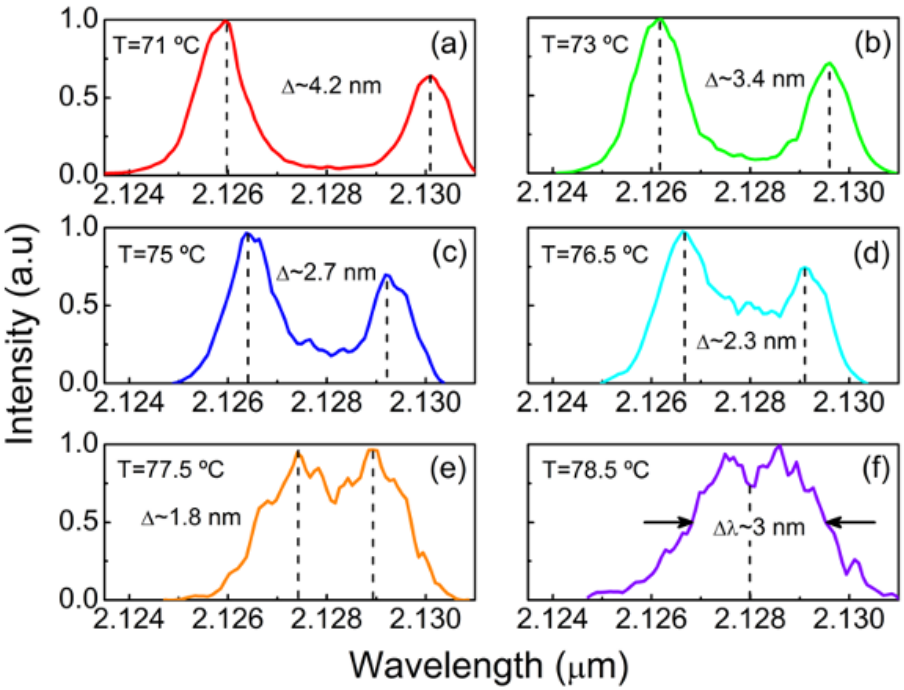

Figure 3.5: Spectral bandwidth measurements of the OPO output using the home-built grating spectrometer. **(a)** Spectrum at 71 °C with peak separation (Δ) of 4.2 nm. **(b)** Spectrum at 73 °C with Δ ~3.4 nm. **(c)** Spectrum at 75 °C with Δ ~2.7 nm. **(d)** Spectrum at 76.5 °C with Δ ~2.3 nm. **(e)** Spectrum at 77.5 °C with Δ ~1.8 nm. **(f)** Spectrum at degeneracy temperature of 78.5 °C with center wavelength at 2128 nm and FWHM of ~3 nm.

and idler peaks, while increasing the crystal temperature the two peaks begin to merge, finally resulting in a composite spectrum centered at the degenerate wavelength of 2128 nm. It is also evident from Figure 3.5(a)-(e) that the signal and idler peak wavelength separation gradually decreases from 4.2 nm at 71 °C to 1.8 nm at 77.5 °C. The peaks finally merge into a single spectrum at a crystal temperature of 78.5 °C at degeneracy with center wavelength at 2128 nm and FWHM bandwidth of ~3 nm, as shown in Figure 3.5(f).

We studied power scaling of the prism-coupled OPO at various crystal temperatures, and the corresponding signal wavelengths, by recording the total (signal plus idler) output power as a function of input pump power. The results are shown in Figure 3.6. The measurements were performed for an available average pump power of 17.8 W at

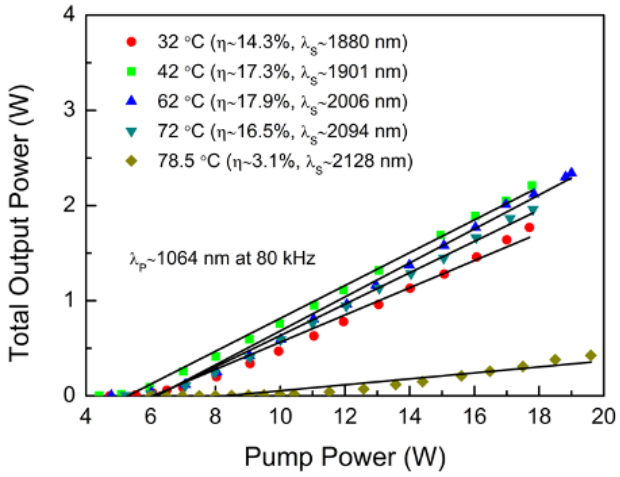

Figure 3.6: Output power scaling of the prism-coupled MgO:PPLN OPO at various temperatures.

80 kHz pulse repetition rate. For each crystal temperature, we measured the slope efficiencies as well as pulse duration at maximum output power. The measurements resulted in typical slope efficiencies of ~14% to 18% for crystal temperatures ranging from 32 °C to 72 °C, with the lowest slope efficiency of ~3% obtained at 78.5 °C. The corresponding maximum total average power and output signal pulse duration at different wavelengths are shown in Figure 3.7. The OPO average output power varies from 1.45 W to 2.1 W over the signal wavelength range of 1880-2110 nm, with the power remaining >1.5 W across nearly the full range and the highest power at 2034 nm.

The FWHM output signal pulse duration, measured using a fast photodetector with a rise-time <200 ps in the OPO wavelength range, was recorded to vary over ~14-18 ns over the same wavelength range. At the degenerate wavelength of 2128 nm, the OPO delivers an average power of 400 mW, with corresponding pulse duration of ~10 ns, as shown in the inset of Figure 3.7. We attribute the shortening of the pulse duration at degeneracy to the increase in the OPO buildup time due to the rise in threshold caused by spectral broadening, which is also accompanied by the decline in output power, as described previously and observed in Figure 3.2 and Figure 3.7. We also performed measurements of output power stability from the prism-coupled OPO at different MgO:PPLN crystal temperatures, corresponding to different wavelengths near 2 μm. The output power was recorded over 1 hour, with the results shown in Figure 3.8(a)-(d). As can be seen, the OPO exhibits a passive long-term power stability

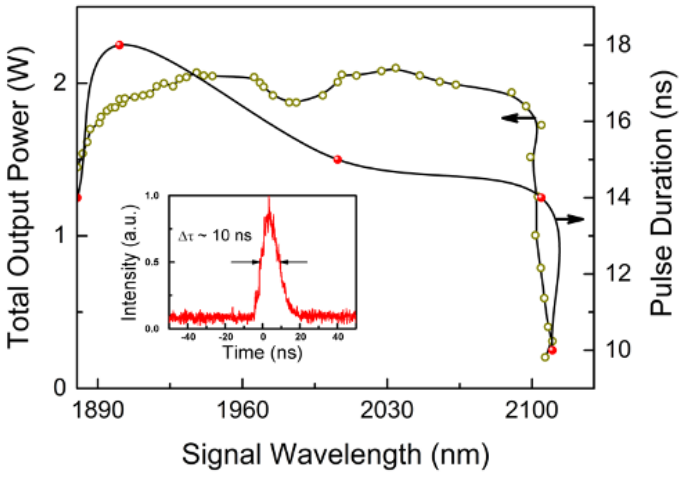

Figure 3.7: Maximum average output power and output pulse duration at different signal wavelengths. Inset: Pulse duration measurement at degeneracy.

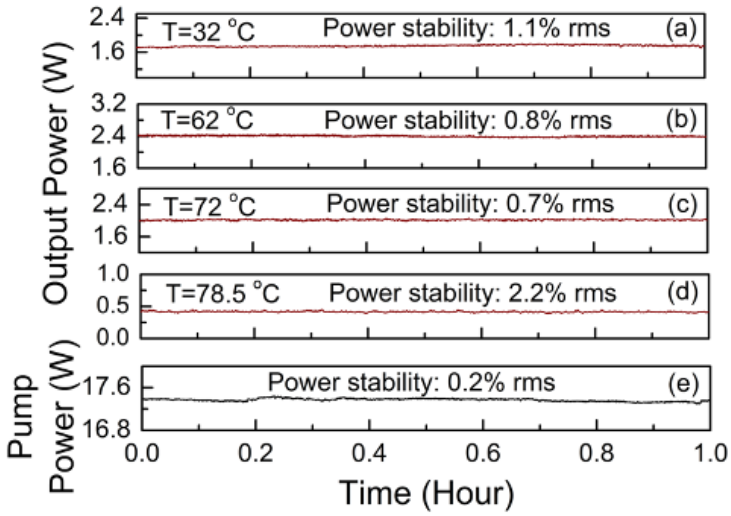

Figure 3.8: (a)-(d) Measurements of power stability for the OPO at different crystal temperatures, corresponding to different output wavelengths, and **(e)** the pump beam over 1 hour.

ranging 0.7% rms to 1.1% rms over the crystal temperature range of 32 °C to 72 °C, with a stability of 2.2% rms at 78.5 °C. Figure 3.8(e) shows the power stability of the Nd:YAG pump laser, measuring 0.2% rms over the same period.

We further recorded the spatial quality of the output beam from the prism-coupled

OPO at the degenerate wavelength of 2128 nm. Using a focusing lens of focal length, f=50 mm, and a scanning beam profiler, we measured the M^2-value of the output beam at 78.5 °C, resulting in M_x^2 <2.8 and M_y^2 <2.3, as shown in Figure 3.9(a)-(b). The degenerate output beam was also observed to exhibit high spatial quality with single-mode Gaussian distribution, as presented in the inset of Figure 3.9(c). Finally,

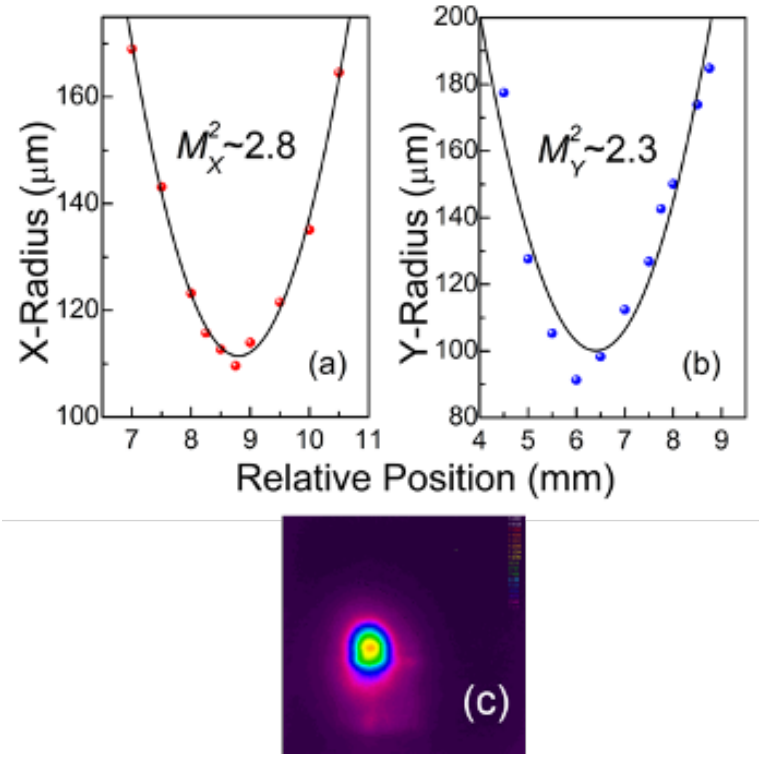

Figure 3.9: **(a)-(b)** Measurement of M^2 beam quality of the OPO output at the degenerate wavelength of 2128 nm along x and y axes. **(c)** Spatial beam profile of the OPO output at degeneracy.

we performed a detailed comparison of the performance of the prism-cavity OPO with a standard free-running OPO without the prism, in a cavity formed by the same plane high reflector and OC, as in Figure 3.1, separated by 78 mm, and operating under the same conditions. Both OPOs were optimized to generate maximum power together with narrow spectral bandwidth. The spectrum of the standard nanosecond OPO using plane mirrors, operating close to degeneracy, measured using a commercial spectrometer, together with the spectrum from the nanosecond OPO with an intracavity prism for spectral control, is shown in Figure 3.10. Due to the limited resolution of the commercial

spectrometer, we used a diffraction grating-based home-made spectrometer to measure the spectrum from the prism-cavity nanosecond OPO. As is evident, the spectral quality of the output is significantly improved with bandwidth reduced from 50 nm (centered at 2092 nm) in the standard plane-mirror cavity to 3 nm (centered at 2128 nm) in the prism cavity. The main performance characteristics of the prism-cavity nanosecond

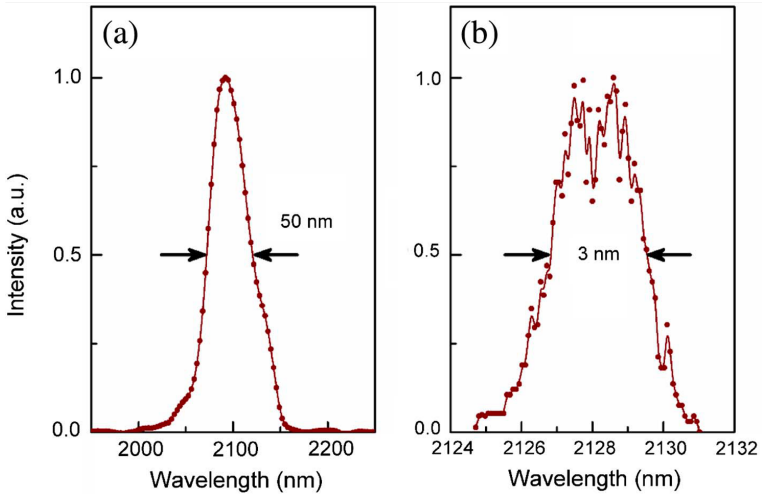

Figure 3.10: Output spectrum from the nanosecond OPO using **(a)** conventional plane-mirror cavity with no frequency selection elements, and **(b)** prism cavity.

OPO are compared with those of the plane-mirror cavity in Table 3.1. It is clear that the prism-cavity OPO surpasses the performance of the conventional plane-mirror OPO in most respects, except for output power and efficiency. However, with further design improvements including the use of an AR-coated prism as well as optimization of output coupling, we expect substantial enhancement in output power and efficiency from the prism-cavity OPO.

3.3 High-average-power high-repetition-rate picosecond OPO near 2 μm

We have also developed a stable high-average-power high-repetition-rate picosecond source at ~2.1 μm in linear polarization. This source is similarly based on a degenerate OPO in DRO configuration, but deploys a diffraction grating as the frequency selective element for spectral control and output power stabilization. The approach similarly

Nanosecond 2.1 μm OPO Parameter	Plane-Mirror Cavity	Prism Cavity
Wavelength (nm)	2092	2128
Spectral bandwidth (nm)	50	3
Output Power (W)	4.3	0.4
Slope efficiency (%)	39	3.1
Power stability over 1 h (% rms)	0.61	2.2
Spatial mode	TEM_{00}	TEM_{00}
Beam quality	–	$M^2 < 2.8$
Repetition rate (kHz)	80	80

Table 3.1: Comparison of the Performance Characteristics of the Plane-Mirror Nanosecond OPO and the Prism Cavity

overcomes the output power and spectral instabilities typical of OPOs in the DRO configuration. Using this technique, our ~2.1 μm picosecond source provides ~5.25 W of average power with high stability, at ~36% conversion efficiency at ~80 MHz repetition rate. The output exhibits long-term power stability better than 1.3% rms over 2 h, high spatial quality with $M^2 < 1.8$, and narrow bandwidth of $\Delta\lambda \sim 2.9$ nm.We further reduce the spectral bandwidth down to ~2.5 nm by using an intracavity telescope in one arm of the OPO cavity.

3.3.1 Experimental setup

The schematic of the experimental setup for ~2.1 μm picosecond OPO is shown in Figure 3.11. The OPO is pumped by a Yb-fiber laser delivering 15 W of average power at a central wavelength of 1064 nm with a FWHM spectral bandwidth of $\Delta\lambda_p \sim 1$ nm, in pulses of ~20 ps duration at ~80 MHz repetition rate. A combination of a HWP and a PBS is used for systematic control of the laser pump power, while a second HWP is used to control the linear input polarization for optimum phase-matching in the nonlinear crystal. The pump beam is focused to a waist radius of $w_0 \sim 130$ μm, corresponding to a focusing parameter of $\xi \sim 0.23$, in a 50-mm-long 5%MgO:PPLN crystal incorporating a single grating period of Λ=32.16 μm for type-0 (e $\Rightarrow$ ee) quasi-phase-matching, identical to that used for the nanosecond OPO in Section 2. The crystal end-faces are similarly AR-coated for high transmission ($R < 0.5\%$) at 1064 nm and over 2050–2150 nm. The

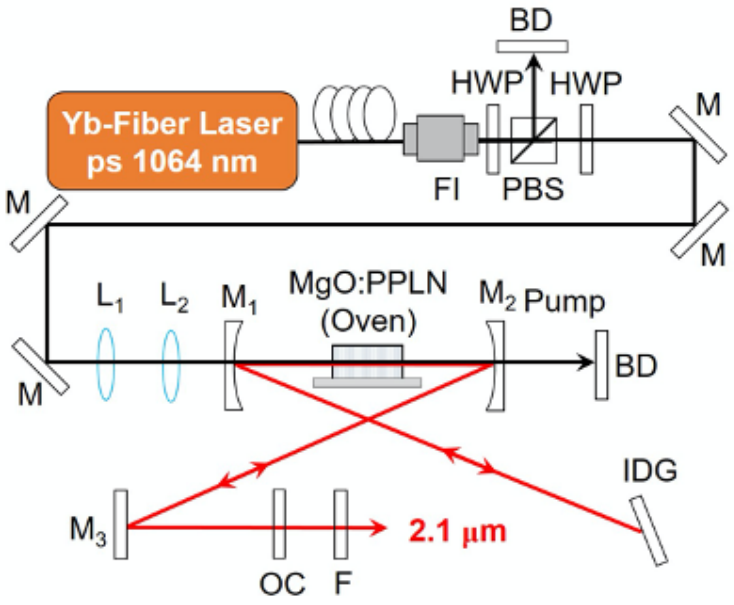

Figure 3.11: Schematic of the experimental setup for the ~2.1 μm source pumped by a Yb-based fiber laser at 1064 nm. FI, Faraday isolator; HWP, half-wave plate; PBS, polarizing beam-splitter; BD, beam dumper; M, mirrors; L, lenses; IDG, intracavity diffraction grating; OC, output coupler; F, filter.

crystal is mounted in an oven providing temperature control from 32 °C to 100 °C with a stability of 0.1°C, thus covering OPO operation through wavelength degeneracy. The OPO is configured in a standing-wave X-cavity formed by two plano-concave mirrors, M_1-M_2, with radius of curvature r = 200 mm, a plane mirror, M_3, an output coupler (OC), and an aluminum intracavity diffraction grating (IDG). All mirrors are highly transmitting (R < 90%) for the pump at 1064 nm and highly reflecting (R > 99%) over 1800–2150 nm, resulting in DRO operation close to degeneracy. The plane OC has partial transmission (T ~ 87%) at 2.1 μm. The total round-trip optical length of the OPO cavity is ~3.78 m, corresponding to a repetition rate of ~80 MHz, ensuring synchronization with the pump laser repetition rate. The IDG is configured in a Littrow configuration, where the incident angle is equal to the diffracted angle, and the beam is thus reflected back and can resonate in the cavity. A Ge filter (F) is used to separate the OPO output beam at ~2.1 μm from the residual pump after the OC.

In order to generate an output wavelength at ~2.1 μm using a pump source at 1064 nm, the temperature of the MgO:PPLN crystal with a grating period of Λ =

32.16 μm has to be set to T ~ 72 °C to allow phase-matching near degeneracy. Under this condition, both signal and idler waves can oscillate in the DRO cavity, which, combined with increased parametric gain close to degeneracy, results in a major increase in intracavity power, and thus a substantially lower threshold compared to the SRO configuration [26]. Therefore, significantly lower peak pump intensities can be used to drive the DRO, and thus in our experiment the beam waist in the center of the crystal was increased up to w_0 ~ 130 μm. The high nonlinearity of MgO:PPLN, together with the long interaction length and the high peak powers in the picosecond regime, enable high conversion efficiencies together with high output power from the picosecond OPO, even in the presence of large output coupling losses. As such, an output coupling as large as T ~ 87% was used for the DRO to maximize the generated average power and extraction efficiency. In addition, operating close to degeneracy, the OPO provides large parametric gain with broad bandwidth and low temporal walk-off [26]. For a 50-mm-long MgO:PPLN crystal with a grating period of Λ = 32.16 μm at a temperature of T ~ 72 °C, the parametric gain bandwidth at ~2.1 μm is calculated to be $\Delta\lambda$ ~ 144 nm for pumping at 1064 nm, as shown in Figure 3.12(a). The group velocity mismatch (GVM) between the pump and signal, and the corresponding group velocity dispersion (GVD), as a function of the signal wavelength is also shown in Figure 3.12(b). At the degenerate wavelength of 2128 nm, the GVM is calculated to be ~113 fs/mm, whereas GVD is approximately -68 fs^2/mm.

3.3.2 Device tuning and characterization

We first performed spectral characterization of the OPO output at a crystal temperature of T = 71 °C using a 400 lines/mm IDG at a blaze angle of 25.2°. The result is shown in Figure 3.13(a), where a central wavelength at λ = 2128 nm with a FWHM spectral bandwidth of $\Delta\lambda$ ~ 2.9 nm was recorded. The measurement was performed using a home-made spectrometer. The spectral bandwidth of the output from the OPO incorporating the IDG is given by [27]

$$\Delta\lambda_{estimated} = \frac{\sqrt{ln(2)}\lambda^2}{\pi w_0 tan(\theta)} \tag{3.3}$$

where w_0 is the beam radius on the IDG and θ is the incidence angle of the resonant beam on the IDG in the Littrow configuration, which depends on the wavelength and

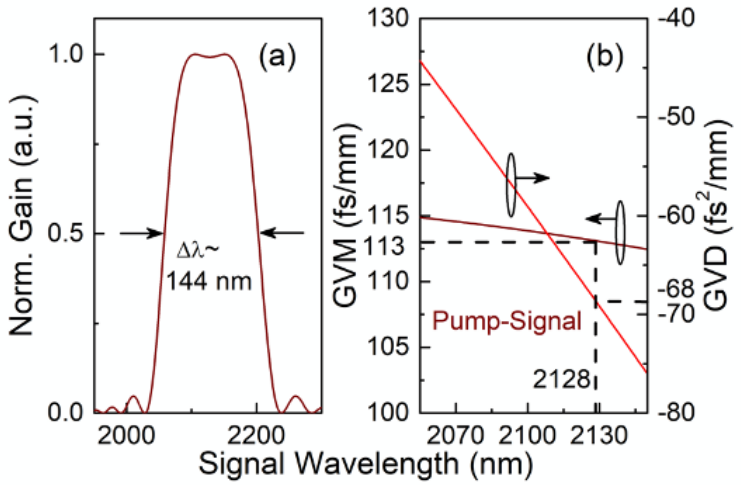

Figure 3.12: **(a)** Parametric gain bandwidth of the OPO at degeneracy. **(b)** GVM between the pump and the signal and the corresponding GVD as a function of the signal wavelength.

the grove spacing.

The calculated FWHM spectral bandwidth as a function of the beam diameter on the IDG with 400 lines/mm is shown in Figure 3.13(b), indicating a FWHM spectral bandwidth of $\Delta\lambda \sim 2.3$ nm and $\Delta\lambda \sim 1.15$ nm for a beam diameter of $2w_0 \sim 2.2$ mm and $2w_0 \sim 4.4$ mm, respectively, on the IDG. Also shown in the inset of Figure 3.13(b) is the experimentally measured beam diameter of 2 mm at the position of the IDG, resulting in a calculated beam diameter of $2w_0 \sim 2.2$ mm on the surface of the IDG.

To further reduce the output spectral bandwidth at the degenerate wavelength of 2128 nm, we increased the beam diamter to $2w_0 \sim 4.4$ mm on the grating by using a telescope with magnification of 2 in one of the arms of the OPO cavity. However, the FWHM spectral bandwidth of the output from the OPO was measured to be $>$2.5 nm, still limited by the resolution of the spectrometer. Hence, using a spectrometer with higher resolution, narrower spectral bandwidth is expected. Considering 20 ps output pulses from the OPO with an expected FWHM bandwidth of $\Delta\lambda \sim 1.15$ nm, we obtain a time-bandwidth product of $\Delta\tau\Delta\nu \sim 1.52$ in the absence of dispersion compesation. This indicates operation of the ~2.1 μm picoscoend OPO near the transform limit ($\Delta\tau\Delta\nu \sim$ 0.44), despite the large time-bandwidth product of $\Delta\tau\Delta\nu \sim 5.3$ for the pump laser.

In order to characterize the output power characteristics of the ~2.1 μm picosecond

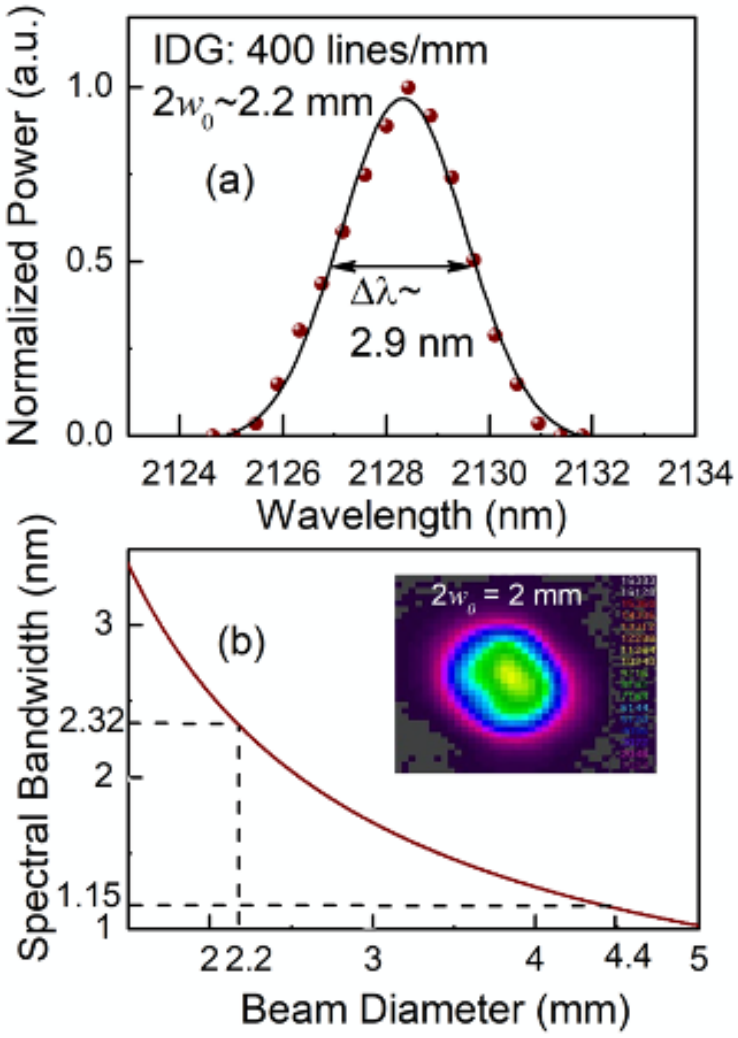

Figure 3.13: **(a)** Spectral characterization of the output beam from the OPO using a 400 lines/mm IDG at blaze angle of 25.2°. **(b)** Calculated FWHM spectral bandwidth as a function of the beam diameter on the IDG with 400 lines/mm. Inset: measured beam profile on the diffraction grating.

OPO, we performed power scaling measurements at a crystal temperature of 71 °C, corresponding to a signal wavelength of 2128 nm, and with the OC extracting ~87% of the intracavity power. The result is shown in Figure 3.14(a), where it can be seen that up to 5.25 W of average power was generated for an input pump power of 15 W, without considering the transmission loss of the Ge filter estimated as ~8% at 2.1 μm. It can

also be seen that the generated power increases linearly with the input power at a slope efficiency of ~43%, with a maximum extraction efficiency of ~36% and external photon conversion efficiency of ~60% at full pump power of 15 W. The pump depletion is ~60% near the maximum input power, while the OPO threshold is measured to be ~2.6 W.We also recorded the long-term stability of the output power, with the OPO generating an average power of ~5 W at 2.1 μm. The result is presented in Figure 3.14(b), where we have a passive power stability of 1.3% rms over 2 h. The stability of the pump laser was recorded to be <0.3% rms over the same period of time. The spatial profile of the output beam measured at a distance of ~75 mm from the cavity is shown in the inset of Figure 3.14(b), exhibiting a single-peak Gaussian spatial intensity distribution with TEM_{00} mode profile and circularity ~90%.

We performed further measurements of spatial beam quality at the degenerate wavelength of 2128 nm, with the OPO delivering output power ~4.5 W. Using a lens with focal length f=50 mm and a scanning beam profiler, we recorded the beam radius across the Rayleigh range and estimated the M^2 values, resulting in $M_x^2 < 1.73$ and $M_y^2 < 1.77$, as shown in Figure 3.15(a) and (b).

We also investigated cavity-delay tuning of the OPO for an input pump power of 13 W, at a temperature of ~71 °C, corresponding to the degenerate wavelength of 2128 nm. The output power as a function of cavity detuning is shown in Figure 3.16. The cavity detuning is normalized to zero for the maximum power at the center of the detuning range. As the cavity length detuning is adjusted from -4.5 mm to +4.9 mm, the output power remains well above 3Wover the entire range with multiple peaks and a maximum of 4.6 W at zero detuning. This tolerance of the OPO operation, in spite of the large cavity detuning of ~10 mm, is enabled by the low GVM at degeneracy, resulting in a temporal walk-off of ~5.6 ps, which is ~4 times lower than the ~20 ps pump and signal pulse durations. Further, the temporal walk-off-limited intraction length is estimated to be ~177 mm, which is ~3.5 times greater than the length of the MgO:PPLN crystal used in this experiment. The power peaks at -3.4 mm and +3.3 mm correspond to signal beams at slightly different wavelengths within the selectivity band of the diffraction grating that have better temporal overlap with the pump pulses. However, we could not measure this wavelength shift, due to the limited resolution of our spectrometer. If we do not consider these two peaks, slightly asymmetric power behavior is observed with more sensitivity in the positive detuning, as also observed previously [27]. In our

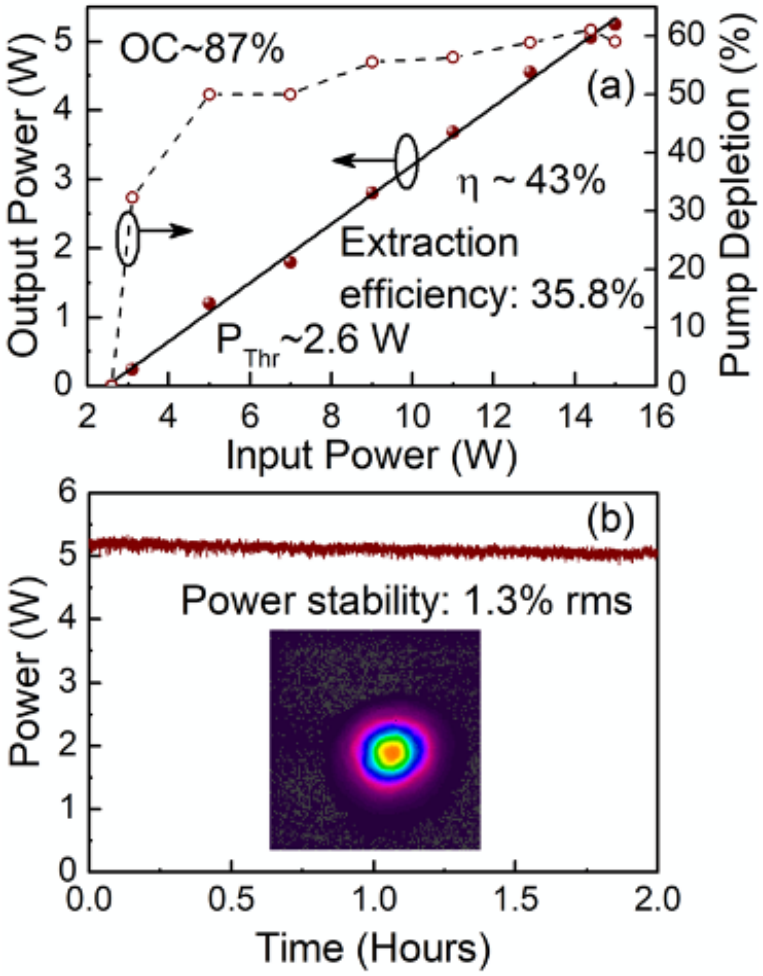

Figure 3.14: **(a)** Simultaneously measured output power and pump depletion as a function of the pump power for the picosecond OPO, and **(b)** long-term power stability of the output from the degenerate OPO operating at 2.1 μm. Inset: spatial beam distribution of the OPO output at 2128 nm.

case, we do not have a large asymmetry because of the similar group velocity of the pump and the resonant signal in the cavity, $v_{gs} \sim 1.38 \times 10^8$ and $v_{gp} \sim 1.36 \times 10^8$, which mitigates the nonlinear pulse-shaping effects.

We futher studied the wavelength tunability of the picosceond OPO around the ~2.1 μm output by rotating the IDG with 400 lines/mm. When operating in the Littrow configuration, for an incidence angle of θ on the IDG, only the associated wavelength,

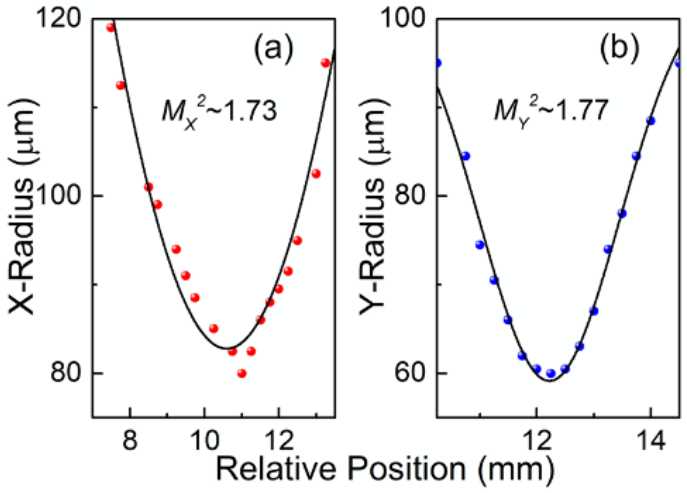

Figure 3.15: M^2 measurement of the output beam at degeneracy along **(a)** x axis, and **(b)** y axis.

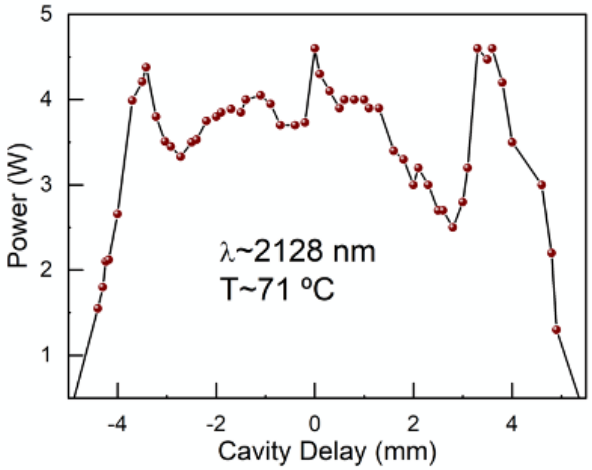

Figure 3.16: Cavity-delay tuning of the picosecond OPO for an input pump power of 13 W at degeneracy.

λ, is exactly reflected on itself, allowing the OPO oscillation according to

$$\lambda = 2dsin(\theta), \tag{3.4}$$

where λ is the reflected wavelength at the angle, $\theta = \alpha = \beta$, and d is the spacing between two adjacent grooves. The measured spectra at different IDG angles, expressed as angle deviation with respect to the blaze angle of 25.2° of the IDG, are shown in

Figure 3.17. By decreasing the angle deviation, the resonant central wavelength in the cavity is also reduced. Using this method, we were able to tune the OPO near ~2.1 μm, generating different spectra for different IDG angles. The output spectra, measured using a commercial spectrometer (StellarNet RED-Wave NIRX-SR-100 T2 BW) with resolution ~35 nm, are shown in Figure 3.17(a). The spectrum with central wavelength at 2128 nm was obtained for a blaze angle at 25.2° or blaze angle deviation of 0°. However, with progressive decrease in the IDG angle, the resonant wavelength in the OPO cavity drops, reaching a minimum wavelength of 2030 nm for an IDG angle at -1.2° deviation from the blaze angle.

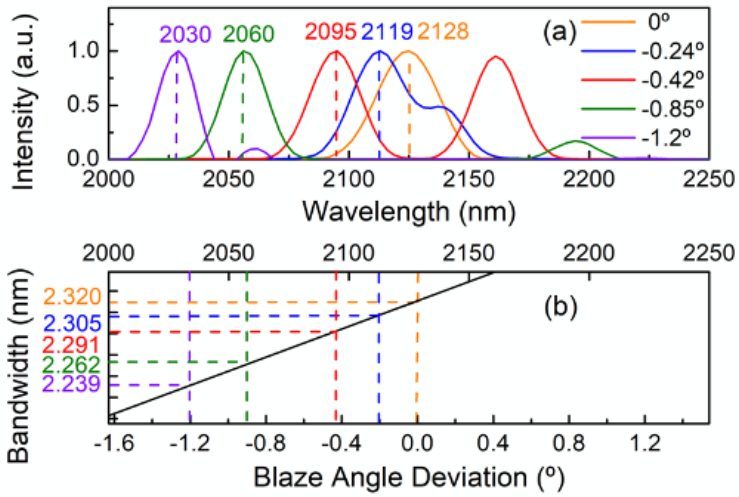

Figure 3.17: **(a)** Spectrum of the resonating signal from the picosecond OPO at different IDG angles, and **(b)** estimated spectral bandwidth selectivity as a function of the blaze angle deviation.

We also calculated the FWHM spectral bandwidth of the output spectra as a function of the resonant wavelength in the cavity and the corresponding IDG angle, as shown in Figure 3.17(b). The result confirms that in the case of the double-peak spectrum generated for an angle deviation of -0.42°, the idler wavelength cannot be resonant in the cavity when we operate away from degeneracy because it is out from the spectral selectivity band imposed by the IDG. Hence, this second peak is the residual idler generated from the resonating signal and the pump beam that has not been completely extracted from the cavity.

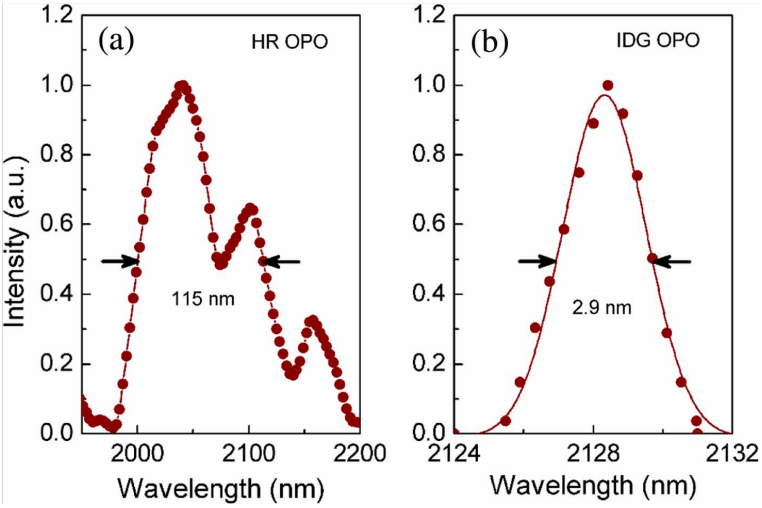

Figure 3.18: Output spectrum from the synchronously pumped picosecond OPO using **(a)** plane-mirror cavity, and **(b)** intracavity diffraction grating in Littrow configuration for spectral control.

Similarly, we performed a detailed comparison of the performance of the synchronously pumped picosecond OPO operating near degeneracy using intracavity IDG with an OPO using a conventional plane mirror. The spectral characteristics for the two OPOs are presented in Figure 3.18, where the measured output spectra in both cases are compared. Again, it is clear that substantial bandwidth reduction from 115 nm (centered at ~2040 nm) in the case of standard plane-mirror OPO to 2.9 nm (centered at 2128 nm) in the OPO with IDG is obtained.

The main performance characteristics of the picosecond OPO in both configurations are presented in Table 3.2. As can be seen, the picosecond synchronously pumped OPO with IDG for spectral control delivers superior performance to the standard OPO using the plane mirror in almost all respects, providing stable, high-power, linearly polarized 2.1 μm picosecond pulses at 80 MHz repetition rate, with well-controlled spectrum and high spatial beam quality.

3.4 Conclusions

In conclusion, we have demonstrated stable and practical operation of pulsed nanosecond and picosecond OPOs near 2 μm by exploiting Nd/Yb solid-state and fiber lasers at 1064 nm as the pump source and a 50-mm-long MgO:PPLN crystal incorporating a

Picosecond 2.1 μm OPO Parameter	**Plane-Mirror Cavity**	**IDG Cavity**
Wavelength (nm)	~2040	~2128
Spectral bandwidth (nm)	~115	2.9
Output Power (W)	4.3	5.25
Power stability over 2 h (% rms)	~1	1.3
Pulse-to-pulse stability over 2 μs (% rms)	2.6	3.4
Round-trip cavity-delay tolerance (mm)	24	10
Spatial mode	TEM_{00}	TEM_{00}
Beam quality	$M^2 < 2.3$	$M^2 < 1.8$
Repetition rate (MHz)	80	80

Table 3.2: Comparison of the Performance Characteristics of the Plane-Mirror Picosecond OPO and the IDG Cavity

single grating period of $\Lambda = 32.16$ μm as the nonlinear gain material. Operating the OPOs in the DRO configuration close to degeneracy, and deploying an intracavity prism and a diffraction grating for spectral and bandwidth control, we have generated high-average-power high-repetition-rate radiation tunable across the 1880-2451 nm spectral range. In both operating domains, the use of intracavity wavelength selection elements has enabled high spectral quality with narrow bandwidth together with high spatial quality and excellent output stability. In nanosecond operation, we have generated up to 2.1 W of average power in pulses of 10-20 ns duration at 80 kHz repetition rate with a FWHM spectral bandwidth down to ~3 nm, in high beam quality with $M^2 < 2.8$, with passive power stability as high as 0.7% rms over 1 h. In picosecond operation, we have achieved up to 5.25 W of average power at 80 MHz repetition rate in ~20 ps pulses with a FWHM spectral bandwidth down to 2.5 nm, in high beam quality with $M^2 < 1.8$, with passive power stability as high as 1.3% rms over 2 h. With further design improvements, substantial enhancements in OPO efficiency, output power, and tunability, and the potential for power scaling, are also expected. The demonstrated OPO sources combine the widely established, reliable, and cost-effective Nd/Yb-doped solid-state and fiber laser technology as the pump source with readily available MgO:PPLN as the nonlinear crystal, thus paving the way for the realization of a new class of practical high-average-power pulsed laser sources for wavelength generation near 2 μm, which will find practical utility for many applications, including pumping of long-wavelength OPOs into the mid-IR.

References

[1] P. J. Gilling, C. B. Cass, M. D. Cresswell, A. R. Malcolm, and M. R. Fraundorfer, "The use of the holmium laser in the treatment of benign prostatic hyperplasia," *J. Endourol.* **10**, 459–461 (1996).

[2] J. Qin, L. Shi, S. Dziennis, R. Reif, and R. K. Wang, "Fast synchronized dual-wavelength laser speckle imaging system for monitoring hemodynamic changes in a stroke mouse model," *Opt. Lett.* **37**, 4005–4007 (2012).

[3] J. Wang, Y. Wang, B. Li, D. Feng, J. Lu, Q. Luo, and P. Li, "Dualwavelength laser speckle imaging to simultaneously access blood flow, blood volume, and oxygenation using a color CCD camera," *Opt. Lett.* **38**, 3690–3692 (2013).

[4] J. L. Machol, R. M. Hardesty, B. J. Rye, and C. J. Grund, "Proposed compact, eye-safe lidar for measuring atmospheric water vapor," in *Advances in Atmospheric Remote Sensing with Lidar*, A. Ansmann, R. Neuber, P. Rairoux, and U. Wandinger, eds. (Springer, 1997), pp. 321–324.

[5] S. Cha, K. P. Chan, and D. K. Killinger, "Tunable 2.1-μm Ho lidar for simultaneous range-resolved measurements of atmospheric water vapor and aerosol backscatter profiles," *Appl. Opt.* **30**, 3938–3943 (1991).

[6] S. W. Henderson, C. P. Hale, J. R. Magee, M. J. Kavaya, and A. V. Hauffaker, "Eye-safe coherent laser radar system at 2.1 μm using Tm, Ho: YAG lasers," *Opt. Lett.* **16**, 773–775 (1991).

[7] S. Ishii, K. Mizutani, H. Fukuoka, T. Ishikawa, B. Philippe, H. Iwai, T. Aoki, T. Itabe, A. Sato, and K. Asai, "Coherent 2 μm differential absorption and wind lidar with conductively cooled laser and two-axis scanning device," *Appl. Opt.* **49**, 1809–1817 (2010).

[8] D. Yan, Y. Wang, D. Xu, P. Liu, C. Yan, J. Shi, H. Liu, Y. He, L. Tang, J. Feng, J. Guo, W. Shi, K. Zhong, Y. H. Tsang, and J. Yao, "High-average-power, high-repetition-rate tunable terahertz difference frequency generation with GaSe crystal pumped by 2 μm dual-wavelength intracavity KTP optical parametric oscillator," *Photon. Res.* **5**, 82–87 (2017).

[9] F. Wang, D. Shen, D. Fan, and Q. Lu, "Widely tunable dual-wavelength operation of a high-power Tm: fiber laser using volume Bragg gratings," *Opt. Lett.* **35**, 2388–2390 (2010).

[10] M. R. K. Soltanian, H. Ahmad, A. Khodaie, I. S. Amiri, M. F. Ismail, and S. W. Harun, "A stable dual-wavelength thulium-doped fiber laser at 1.9 μm using photonic crystal fiber," *Sci. Rep.* **5**, 14537 (2015).

[11] L. C. Kong, Z. P. Qin, G. Q. Xie, X. D. Xu, J. Xu, P. Yuan, and L. J. Qian, "Dual-wavelength synchronous operation of a mode-locked 2-μm Tm: $CaYAlO_4$ laser," *Opt. Lett.* **40**, 356–358 (2015).

[12] M. Henriksson, M. Tiihonen, V. Pasiskevicius, and F. Laurell, "$ZnGeP_2$ parametric oscillator pumped by a linewidth-narrowed parametric 2 μm source," *Opt. Lett.* **31**, 1878–1880 (2006).

[13] D. Yan, Y. Wang, D. Xu, W. Shi, K. Zhong, P. Liu, C. Yan, J. Mei, J. Shi, and J. Yao, "High power, widely tunable dual-wavelength 2 μm laser based on intracavity KTP optical parametric oscillator," *J. Phys. D* **50**, 035104 (2017).

[14] F. Ganikhanov, T. Caughey, and K. L. Vodopyanov, "Narrow-linewidth middle-infrared $ZnGeP_2$ optical parametric oscillator," *J. Opt. Soc. Am. B* **18**, 818–822 (2001).

[15] K. L. Vodopyanov, O. Levi, P. S. Kuo, T. J. Pinguet, J. S. Harris, and M. M. Fejer, "Optical parametric oscillation in quasi-phase-matched GaAs," *Opt. Lett.* **29**, 1912–1914 (2004).

[16] S. Haidar and H. Ito, "Injection-seeded optical parametric oscillator for efficient difference frequency generation in mid-IR," *Opt. Commun.* **171**, 171–176 (1999).

[17] K. L. Vodopyanov, I. Makasyuk, and P. G. Schunemann, "Grating tunable 4-14 μm GaAs optical parametric oscillator pumped at 3 μm," *Opt. Express* **22**, 4131–4136 (2014).

[18] L. Maidment, P. G. Schunemann, and D. T. Reid, "Molecular fingerprint-region spectroscopy from 5 to 12 μm using an orientation-patterned gallium phosphide optical parametric oscillator," *Opt. Lett.* **41**, 4261–4264 (2016).

[19] H. Huang, H. Wang, and D. Shen, "VBG-locked continuous-wave and passively Q-switched Tm:Y_2O_3 ceramic laser at 2.1 μm," *Opt. Mater. Express* **7**, 3147–3154 (2017).

[20] A. Hemming, N. Simakov, J. Haub, and A. Carter, "A review of recent progress in holmium-doped silica fibre sources," *Opt. Fiber Technol.* **20**, 621–630 (2014).

[21] J. Kwiatkowski, J. K. Jabczynski, W. Zendzian, L. Gorajek, and M. Kaskow, "High repetition rate, Q-switched Ho: YAG laser resonantly pumped by a 20 W

linearly polarized Tm: fiber laser," *Appl. Phys. B* **114**, 395–399 (2014).

[22] J. Saikawa, M. Fujii, H. Ishizuki, and T. Taira, "52 mJ narrow-bandwidth degenerated optical parametric system with a large-aperture periodically poled MgO:$LiNbO_3$ device," *Opt. Lett.* **31**, 3149–3151 (2006).

[23] S. Chaitanya Kumar and M. Ebrahim-Zadeh, "Yb-fiber-based, high-average-power, high-repetition-rate, picosecond source at 2.1 μm," *Laser Photon. Rev.* **10**, 970–977 (2016).

[24] P. Schlup, I. T. McKinnie, and S. D. Butterworth, "Single-mode, singly resonant, pulsed periodically poled lithium niobate optical parametric oscillator," *Appl. Opt.* **38**, 7398–7401 (1999).

[25] O. Paul, A. Quosig, T. Bauer, M. Nittmann, J. Bartschke, G. Anstett, and J. A. L'Huillier, "Temperature-dependent Sellmeier equation in the MIR for the extraordinary refractive index of 5% MgO doped congruent $LiNbO_3$," *Appl. Phys. B* **86**, 111–115 (2007).

[26] M. Ebrahim-Zadeh and M. H. Dunn, "Optical parametric oscillators," in *Handbook of Optics*, 2nd ed., Vol. IV (McGraw-Hill, 2000), pp. 1–72.

[27] C. Laporte, J. Dherbecourt, J. Melkonian, M. Raybaut, C. Drag, and A. Godard, "Analysis of cavity-length detuning in diffraction-grating narrowed picosecond optical parametric oscillators," *J. Opt. Soc. Am. B* **31**, 1026–1034 (2014).

4

Fiber-laser-based, 1-μm-pumped, high power picosecond optical parametric oscillator covering the 1.3-1.5 μm region

This chapter constitutes the following publication:

1. **B. Nandy**, S. Chaitanya Kumar, and M. Ebrahim-Zadeh, "Fiber-laser-based, 1-μm-pumped, high power picosecond optical parametric oscillator covering the 1.3-1.5 μm region". (To be submitted)

4.1 Background and motivation

High-average-power picosecond mid-infrared (mid-IR) OPO sources based on 5%MgO-doped periodically-poled $LiNbO_3$ (MgO:PPLN) pumped at 1.064 μm are of great interest for variety of applications spanning from physics [1], chemistry [2, 3], biology and medical sciences [3-6]. Such OPOs can be rapidly tuned in the mid-IR up to ~4.3 μm, affording high output coupling losses [6] providing watt-level output power in the mid-IR with excellent photon-conversion efficiencies. Although such PPLN-based OPOs are now matured and well-established in all time scales from CW to femtosecond [7-10], access to the 1.1-1.4 μm wavelength range with good average power while pumping at 1.064 μm is proven to be challenging. This is due to the strong multi-phonon absorp-

tion at idler wavelengths near the infrared transparency cut-off of MgO:PPLN crystal, resulting in an absorption coefficient of 0.08 cm^{-1} at 4 μm, rapidly increasing to 0.94 cm^{-1} at 5 μm [11]. Due to this strong absorption of the idler wave beyond 4 μm, the photon-conversion efficiency of the signal wave is drastically reduced, either ceasing the OPO operation and/or leading to catastrophic damage, thereby precluding direct access to wavelengths below 1.4 μm. An alternative approach to access the near-IR wavelength range below 1.4 μm is to implement frequency doubling of the idler in another suitable MgO:PPLN crystal. Recently, we have demonstrated such idler resonant configuration that enables Watt-level output power tunable from 2198-4028 nm, with good beam quality [12]. By deploying the frequency doubling crystal internal to the idler resonant OPO, we can exploit the high intracavity power as well as the good spatial beam quality of the resonant idler beam, generating practical output powers in the desired wavelength range below 1.4 μm.

In 1995, Ebrahimzadeh *et. al.* demonstrated a continuous tuning picosecond OPO based on temperature-tuned LiB_3O_5 (LBO) and synchronously pumped by a self-mode-locked Ti:sapphire laser at 81 MHz continuously tunable from 1.15-2.26 μm with 200 mW power [13]. Such LBO based OPOs proved to be highly versatile, simple and cost-effective source of picosecond near-infrared pulses but lacked the reliability of diode pumped fiber lasers. This was fulfilled by Kienle et. al. who demonstrated a picosecond, green-pumped, MgO:PPLN based OPO synchronously pumped by a frequency-doubled, Yb-fiber-amplified gain-switched laser diode with ~107 mW power in the 1.28-1.54 μm region but the crystal suffered physical damage in the center of the poled grating after only ~30 min of operation [14]. This is one of the major problems with PPLN when it is green-pumped apart from low gain. Recently, Kumar *et. al.* reported a stable, Yb-fiber-laser-based, green-pumped picosecond OPO based on periodically poled potassium titanyl phosphate (PPKTP) using fan-out grating design with 300 mW in the idler at 1338 nm and tunable from 1201-1998 nm (idler) and 726-955 nm (signal) [15]. PPKTP is a very new crystal and is very difficult to obtain unlike PPLN which is a very matured crystal with wide commercial availability.

Here, we present the first widely tunable idler-resonant OPO based on MgO:PPLN crystal (Λ= 31.27 μm) with intracavity SHG of the idler wave using a PPLN crystal with fan-out grating (Λ=34.8-36.2 μm) in a ring cavity configuration which was synchronously pumped by a 1.064 μm picosecond Yb-doped fiber laser. A wide tuning

range of 1.63-1.86 μm (signal), 2.54-3.07 μm (idler) and 1.31-1.54 μm was achieved with high-average-power in the ~1.3 μm region. We obtained >1 W of SHG in the 1.29-1.38 μm region. The performance characteristics of the intracavity-SHG-ring cavity OPO has been demonstrated.

4.2 Experimental Setup

The schematic of the proposed idler-resonant ring-cavity PPLN OPO with intracavity SHG is depicted in Figure 4.1. The OPO is synchronously pumped by a mode-locked Yb-fiber laser (Fianium, $FP1060-20$) delivering up to 20 W of average power at a central wavelength of 1064 nm with a full-width-at-half-maximum (FWHM) spectral bandwidth of $\Delta\lambda_p$ ~1 nm, in pulses of ~20 ps duration at a ~79.5 MHz repetition rate. After attenuation optics for systematic input power control, an average pump power of ~13 W is focused to a waist radius of w_0 ~60 μm at the center of the nonlinear crystal, C_1, which is 50-mm-long MgO:PPLN with grating period Λ=31.27 μm. To reduce the photorefractive effect, the crystal is doped with 5 mol % of MgO. The crystal (C_1) end-faces are antireflection (AR)-coated for high transmission (R<1%) at 1.064 μm, (R<0.5%) at 1.4-2 μm and (R<7%) over 2-4 μm. The crystal (C_1) is mounted in an oven providing temperature control from 23.5 °C to 200 °C with a stability of 0.1 °C.

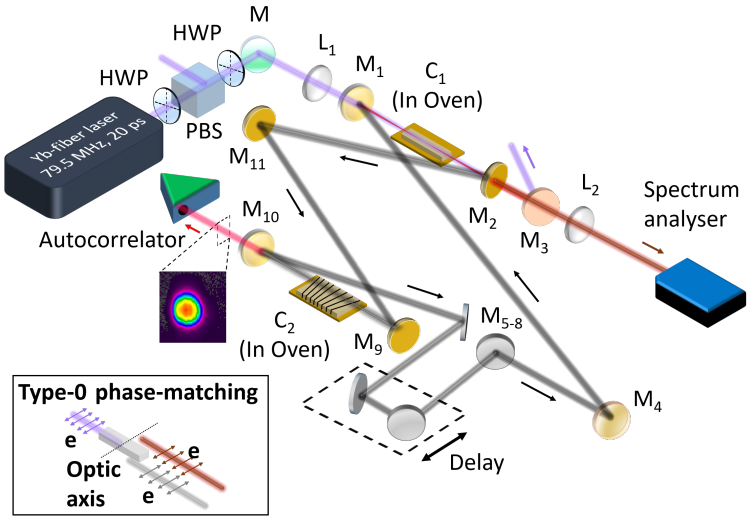

Figure 4.1: Experimental setup of the idler-resonant PPLN OPO with intracavity SHG. HWP: Half-wave plate, M: Mirrors, L: Lens, C: Crystal.

The OPO is configured in a ring cavity which is composed of two sets of folding mirrors; one (M_1 and M_2) with a focal length of 100 mm for the gain crystal and the other (M_9 and M_{10}) with a focal length of 75 mm for the SHG crystal. The SHG crystal, C_2, is a 50-mm-long, 10-mm-wide and 1-mm-thick 5%MgO:PPLN with fanout grating (Λ=34.8-36.2 μm) whose end-faces are antireflection (AR)-coated for high transmission (R<1%) at 1.2-1.6 μm and (R<2%) over 2.4-3.5 μm. The crystal (C_2) is also mounted in an oven providing temperature control from 23.5 °C to 200 °C with a stability of 0.1 °C. The cavity mirrors ($M_1 - M_2$, $M_9 - M_{10}$) have high reflectance in a wavelength range of 2.1-4 μm, and high transmittance with AR-coating at 1.064 and 1.3-2 μm. The silver coated mirrors (M_5-M_8) have high reflectance (R>97%) over 0.5-20 μm. The mirror (M_3) is a dichroic mirror for pump-separation and signal-extraction, and has high reflectance (R>99.9%) over 1.05-1.5 μm and high transmittance (T>99%) over 1.5-2.15 μm. The lens (L_2) is used for collimation of the signal beam and has high transmittance (T>97%) with AR-coating at 1.65-1.9 μm.

4.3 Device tuning and characterization

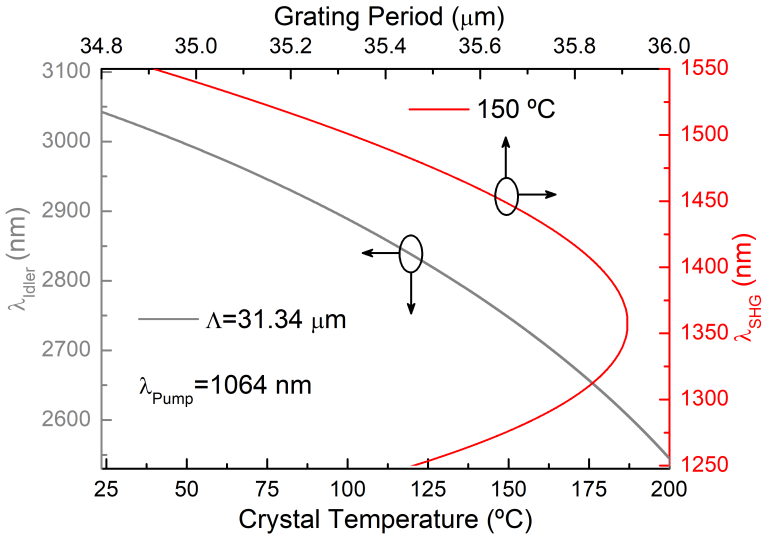

Figure 4.2: Calculation of idler wavelength with respect to crystal temperature of gain crystal (C_1) for fixed grating period (Λ=31.27 μm) and corresponding SHG wavelength versus the grating period of the fanout-grating crystal (C_2) kept at a fixed temperature of 150 °C.

The theoretically calculated idler wavelength tuning characteristics of the crystal (C_1) with single grating period (Λ=31.34 μm) as a function of crystal temperature, when pumped at 1064 nm are shown in Figure 4.2. The corresponding idler SHG wavelength tuning using a second MgO:PPLN crystal (C_2) requires the grating periods ranging from Λ=34.8-36.2 μm to operate at a fixed temperature of 150 °C. We then, performed the experimental investigation of the wavelength tuning characteristics of the OPO. Idler wavelength tuning was achieved by varying the temperature of the gain crystal C_1. We first studied the temperature tuning of the OPO and the corresponding intracavity SHG together with the total average output power variation across the tuning range. By varying the temperature of the gain crystal, C_1, over 23.5 [∘]C-200 °C, we were able to tune the generated single-pass signal across 1642-1856 nm. The corresponding SHG of the resonating idler is tunable across 1272-1515 nm, by varying the position of crystal C_2 kept at a constant temperature of 150 °C, resulting in a total (signal plus SHG) tuning over 457 nm. The results are shown in Figure 4.3, Figure 4.3(a) represents the measured signal output power corresponding to the measured wavelengths, and Figure 4.3(b) represents the measured SHG output power. The inset in Figure 4.3(b) shows the spatial beam profile of the SHG at maximum output power of 1230 mW at 1324 nm.

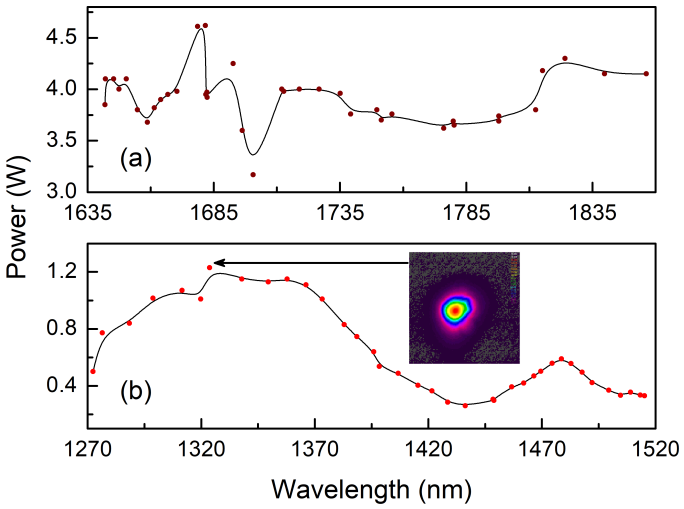

Figure 4.3: (a-b) Signal and SHG total output power generated with respect to their corresponding wavelengths at fixed pump power. The solid curves are a guide to the eye. Inset: SHG spatial beam profile at maximum output power.

The measurements were performed for a fixed input average pump power of ~10 W at 1064 nm. As can be seen, the total average SHG output power from the OPO is >1 W in the 1290-1375 nm region which is generally not easily accessible in the signal wavelength in a picosecond singly resonant OPO based on MgO:PPLN, pumped at 1064 nm as the corresponding idler wavelengths extend as far as 4704-5761 nm, beyond the long wavelength transparency cut-off of MgO:PPLN, where the absorption coefficient of the crystal is >0.94 cm^{-1} [11]. The average output signal power varies from ~3.85 W at 1642 nm to ~4.15 W at 1856 nm and the corresponding SHG output power varies from ~500 mW at 1272 nm to ~330 mW at 1515 nm. The sharp decline in the output SHG power at ~1440 nm accompanied by the drop in the idler power, is due the OH^- absorption in the two MgO:PPLN crystals at 2.880 μm. The observed drop in SHG output power below 1300 nm is due to the AR coatings of mirror M10 which is highly transmitting only between 1300-2000 nm and at 1064 nm.

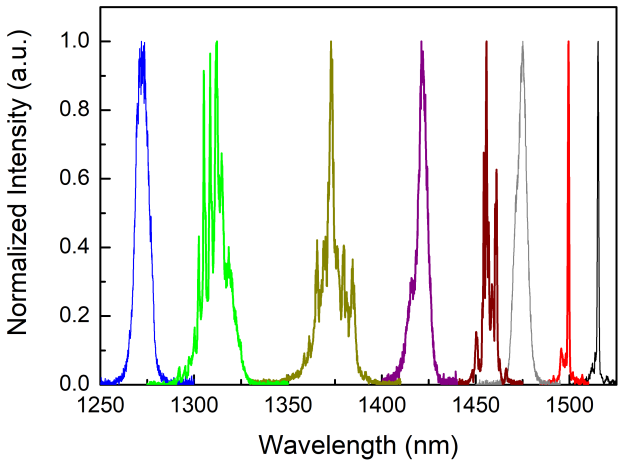

Figure 4.4: SHG spectrum over the entire tuning range.

We also recorded the signal and SHG spectrum over the entire tuning range of the OPO. All the spectral measurements were recorded using an infrared Spectrometer (800-2600 nm range) with a resolution of <0.5 nm. The results of the SHG tuning are shown in Figure 4.4. The SHG is tuned from 1272 nm ($\Delta\lambda$ ~8.1 nm) to 1515 nm ($\Delta\lambda$ ~0.8 nm), the corresponding signal spectrum varies from 1856 nm ($\Delta\lambda$ ~31.9 nm) to 1642 nm ($\Delta\lambda$ ~8.7 nm) as shown in Figure 4.5. As the crystal is heated, the resonant-

idler wavelength moves towards degeneracy, which results in increase in parametric gain bandwidth. And due to the high-reflector (HR) cavity for the resonant idler, it results in broadband oscillation leading to broadband signal generation.

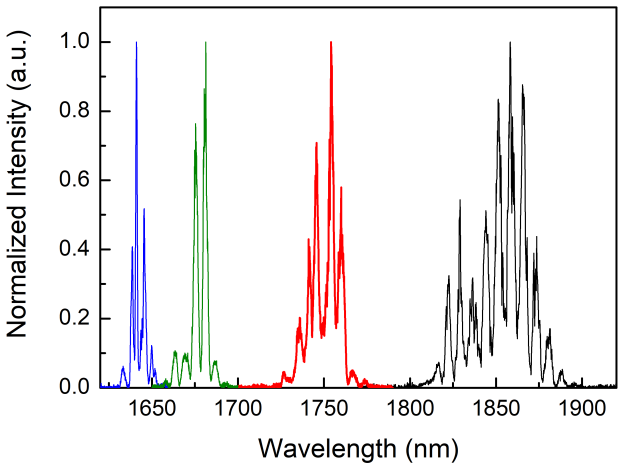

Figure 4.5: Signal spectrum over the entire tuning range.

We studied power scaling of the OPO at three different crystal temperatures, and the corresponding signal and SHG wavelengths, by recording the output powers as a function of input pump power. The measurements were performed for an available pump power of 10 W at 79.5 MHz pulse repetition rate. The crystal temperature (C_1) was tuned from room temperature (T=23.5 °C) to T=200 °C. We obtained signal power of 3.85 W (λ_{Signal}= 1642 nm, η=57.4 %) and SHG power of 330 mW (λ_{SHG}= 1515 nm, η=5.4%) with pump depletion of 70%, when C_1 was kept at room temperature (T=23.5 °C). Upon heating C_1 to T=170 °C, we obtained signal power of 3.7 W (λ_{Signal}= 1780 nm, η=40.8%), while the SHG power increased to 1230 mW (λ_{SHG}= 1324 nm, η=13.3%) with pump depletion of 84% as shown in Figure 4.6. As we further increase C_1 temperature to 200 °C, the signal power increases to 4.15 W (λ_{Signal}= 1856 nm, η=45.9%) with maximum SHG power of 500 mW (λ_{SHG}= 1272 nm, η=6.3%).

We performed measurements of output power stability over 1 hour for the signal and SHG for the three mentioned crystal temperatures. The output power stability corresponding to T=23.5 °C of the gain crystal is shown in Figure 4.7. As can be seen, the OPO exhibits passive long-term power stability of 0.4% rms for signal (λ=1642 nm)

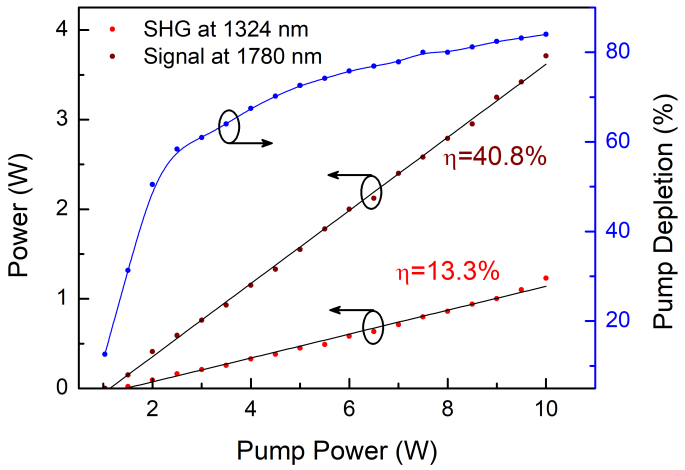

Figure 4.6: Output power scaling of the idler-resonant MgO:PPLN OPO.

and 0.6% rms for SHG (λ=1515 nm). Upon heating the crystal (C_1) to 170 °C, the power stability of the signal (λ=1780 nm) was recorded to be 0.6% rms over one hour and for the frequency doubled SHG (λ=1324 nm) recorded 3% rms over 1 hr. We also measured the power stabilities over 1 hour at maximum crystal oven temperature (C_1) of 200 °C, we found 0.9% rms for signal (λ=1856 nm) and 0.4% for SHG (λ=1272 nm) respectively.

We also performed the spectrum stability measurements of the signal and SHG for the above mentioned three temperature sets. At room temperature, the signal spectrum has exceptional peak stability of 0.006% rms at central wavelength of 1649 nm and FWHM stability of 8.1% rms over 1 hr. The corresponding SHG spectrum stability is also shown in Figure 4.8, where we observed peak stability of 0.01% rms at central wavelength of 1513 nm over 1 hr. At maximum crystal temperature of 200 °C, the peak stability of the signal at 1860 nm was recorded to be 0.6% rms over 1 hr. And the corresponding SHG at 1273 nm had peak stability of 0.05% rms over 1 hr.

The reason for the slightly poor spectral stability at higher crystal temperatures could be attributed to the fluctuation in the crystal temperature. These temperature fluctuation in turn leads to wavelength fluctuation in the signal and the resonating idler which also affects the mode of the cavity. And since the position and the temperature of the fanout grating crystal for SHG is fixed, the SHG power is hugely affected by

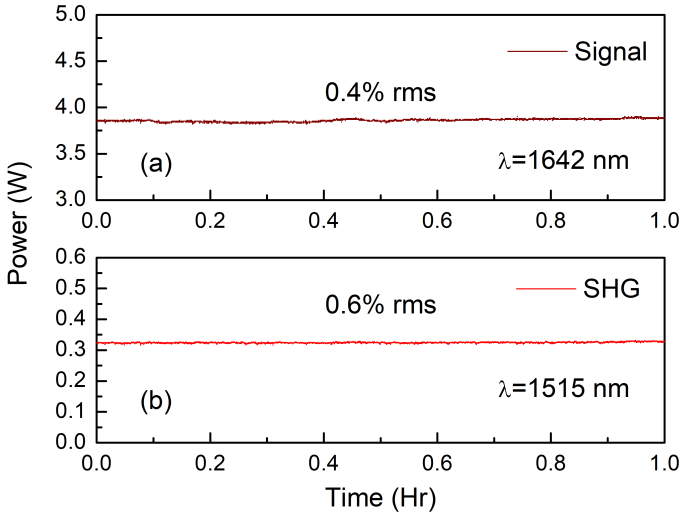

Figure 4.7: (a)-(b) Measurements of power stability for the signal and SHG at fixed gain-crystal temperature of 23.5 °C.

the idler wavelength fluctuations. It is to be noted that the SHG phase-matching conditions are not adequately fulfilled across the idler spectrum, owing to the limited spectral acceptance bandwidth of the SHG crystal at a given position and temperature. Further, the gain-bandwidth of the gain crystal as well as the SHG crystal increases towards degeneracy allowing the OPO to sustain multiple-modes simultaneously which further causes power fluctuations in the resonating wave.

In order to extract some idler power from the OPO, we replaced mirror M_4 with an output coupler (OC) with varying transmission (T~87%-98%) over the idler tuning range. Then we again performed the experimental investigation of the wavelength tuning characteristics of the OPO. Idler wavelength tuning was achieved by varying the temperature of the gain crystal C_1. We first studied the temperature tuning of the OPO and the corresponding intracavity SHG together with the total average output power variation across the tuning range. By varying the temperature of the gain crystal, C_1, over 25 °C-200 °C, we were able to tune the generated single-pass signal across 1627-1781 nm, the resonating idler across 2610-3075 nm. The corresponding SHG of the idler is tunable across 1305-1540 nm, by varying the position of crystal C_2 kept at a constant temperature of 150 °C, resulting in a total (signal plus idler plus SHG) tuning over 854 nm. The results are shown in Figure 4.9, Figure 4.9(a) represents the measured signal output power corresponding to the measured wavelengths, Figure 4.9(b) represents the

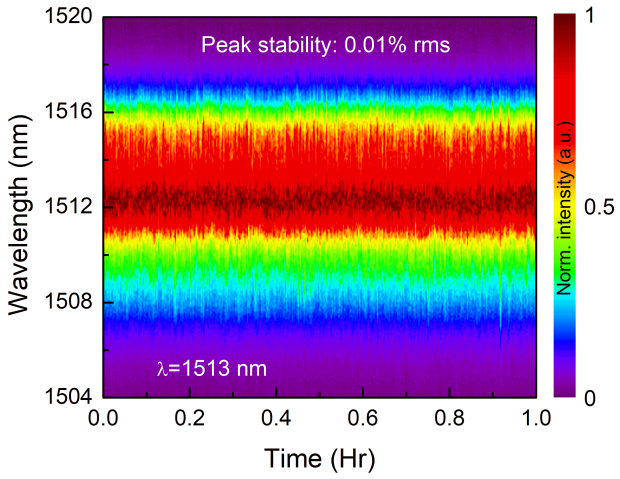

Figure 4.8: Measurement of spectrum stability for the SHG at fixed gain-crystal temperature of 23.5 °C.

measured SHG output power and Figure 4.9(c) represents the measured idler output power corresponding to the calculated idler wavelengths and the blue line represents the transmission of the output coupler for the idler wave.

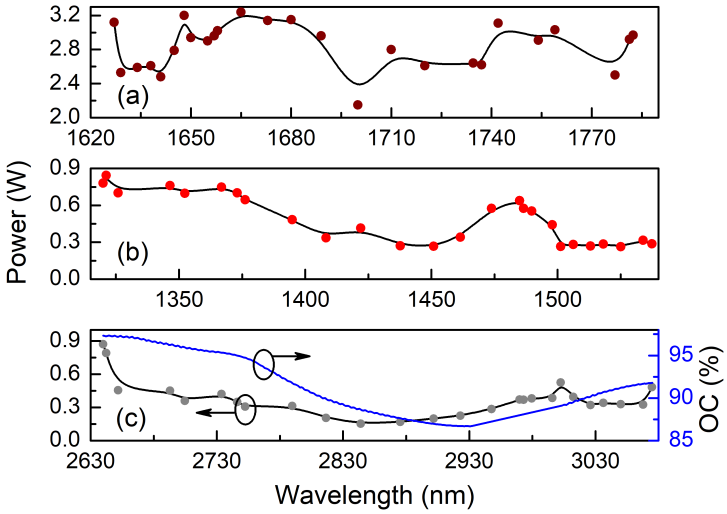

Figure 4.9: (a-c) Signal, SHG and idler total output power generated with respect to their corresponding wavelengths at fixed pump power. The blue line in (c) represents the output-coupling. The solid curves are a guide to the eye.

The measurements were performed for a fixed input average pump power of ~13 W at 1064 nm. As can be seen, the total average SHG output power from the OPO is >600 mW in the 1305-1375 nm region. The average output signal power varies from ~3.12 W at 1627 nm to ~3.38 W at 1781 nm while the average output idler power varies from ~482 mW at 3075 nm to ~872 mW at 2610 nm and the corresponding SHG output power varies from ~844 mW at 1305 nm to ~287 mW at 1540 nm. We once again recorded the signal and SHG spectrum over the entire tuning range of the OPO. All the spectral measurements were recorded using an infrared Spectrometer (800-2600 nm range) with a resolution of <0.5 nm. The results of the SHG tuning are shown in Figure 4.10. The SHG is tuned from 1305 nm ($\Delta\lambda$ ~8.7 nm) to 1540 nm ($\Delta\lambda$ ~5 nm), the corresponding signal spectrum varies from 1781 nm ($\Delta\lambda$ ~3.6 nm) to 1627 nm ($\Delta\lambda$ ~6.4 nm).

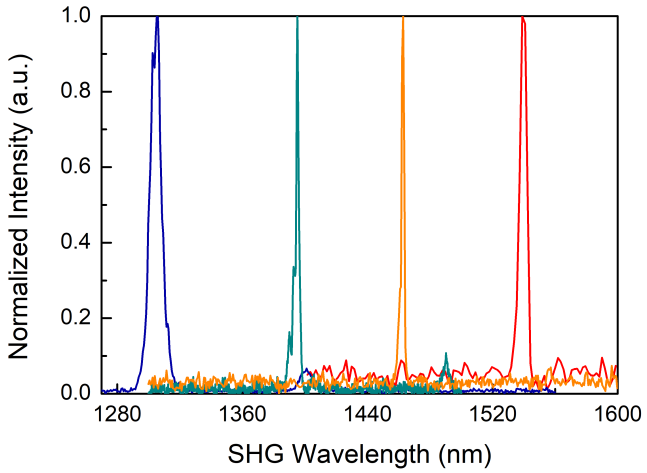

Figure 4.10: SHG spectrum over the entire tuning range.

The SHG power scaling with respect to the intra-cavity idler power for SHG wavelength of 1395 nm is shown in Figure 4.11. The SHG power scales quadratically as function of the intracavity idler power as expected. The intra-cavity idler power was calculated based on the measured signal output power using photon energy conservation. The spatial beam profile of the SHG at 1537 nm is presented in the inset of Figure 4.11. We also performed measurements of output power stability over 1 hour for the signal, idler and SHG for the three mentioned crystal temperatures. The output power stability corresponding to T=25 °C of the gain crystal is shown in Figure 4.12. As

can be seen, the OPO exhibits passive long-term power stability of 0.2% rms for signal (λ=1627 nm), 0.4% rms for idler (λ=3075 nm) and 0.7% rms for SHG (λ=1538 nm). Upon heating the crystal (C_1) to 150 °C, the power stability of the signal (λ=1720 nm) was recorded to be 0.6% rms over one hour and for the corresponding idler (λ=2790 nm) was 1.3% rms, the frequency doubled SHG (λ=1395 nm) recorded 1.8% rms over 1 hr. We also measured the power stabilities over 1 hour at maximum crystal oven temperature (C_1) of 200 °C, we found 4% rms for signal (λ=1782 nm), 2.7% for idler (λ=2641 nm) and 5.2% for SHG (λ=1310 nm) respectively.

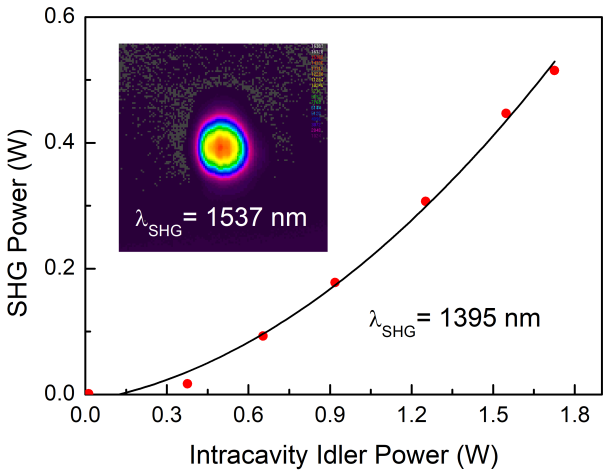

Figure 4.11: SHG power scaling with respect to intra-cavity idler power. Inset: spatial beam profile of SHG.

We further measured the M^2 value of the signal, idler and SHG beams at three different crystal temperatures for the ring cavity. Using a focusing lens of focal length, f=50 mm, and a scanning beam profiler, we performed the measurements and the data is presented in Table 4.1.

λ_{SHG}	λ_{Signal}	λ_{Idler}	**SHG**		**Signal**		**Idler**	
(nm)	(nm)	(nm)	M_X^2	M_Y^2	M_X^2	M_Y^2	M_X^2	M_Y^2
1311	1790	2623	2.1	1.7	1.9	1.9	1.9	1.6
1413	1711	2814	2.2	1.8	1.6	1.4	2.3	1.6
1537	1628	3075	2.6	2.3	1.6	1.6	1.8	1.4

Table 4.1: M^2 data for the ring cavity OPO.

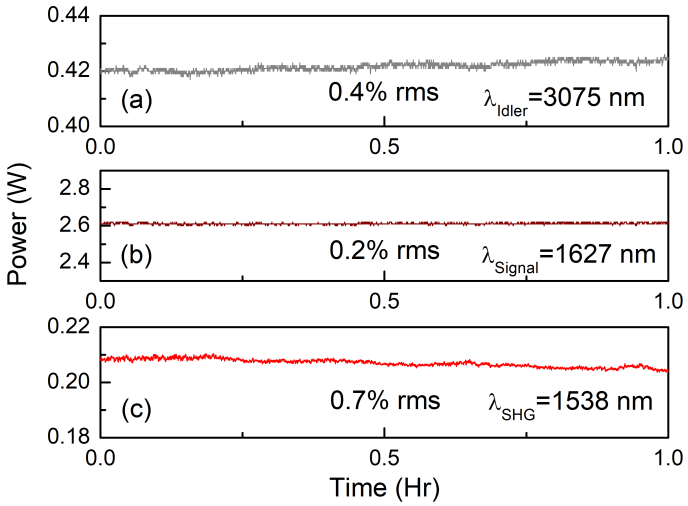

Figure 4.12: (a)-(c) Measurements of power stability for the idler, signal and SHG at fixed gain-crystal temperature of 25 °C.

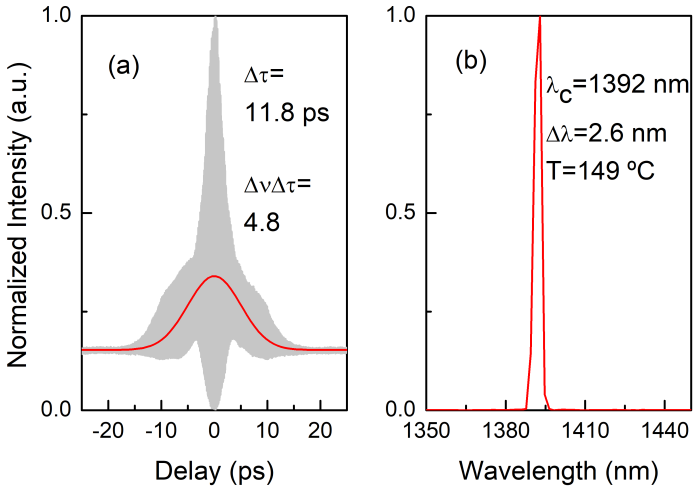

Figure 4.13: (a) Interferometric autocorrelation and (b) optical spectrum of the SHG wave at 1392 nm for the intracavity SHG ring cavity OPO.

The duration of the SHG pulses were measured by interferometric autocorrelation as shown in Figure 4.13(a). We observed that the nonlinear effects in the SHG crystal lead to temporal shortening of the seed pulses and the measured pulse duration (FWHM) of the SHG pulse of the ring cavity OPO at 1392 nm is typically ~11.8 ps, assuming sech^2 pulse shape. The spectral width is approximately 2.6 nm (FWHM) as shown in

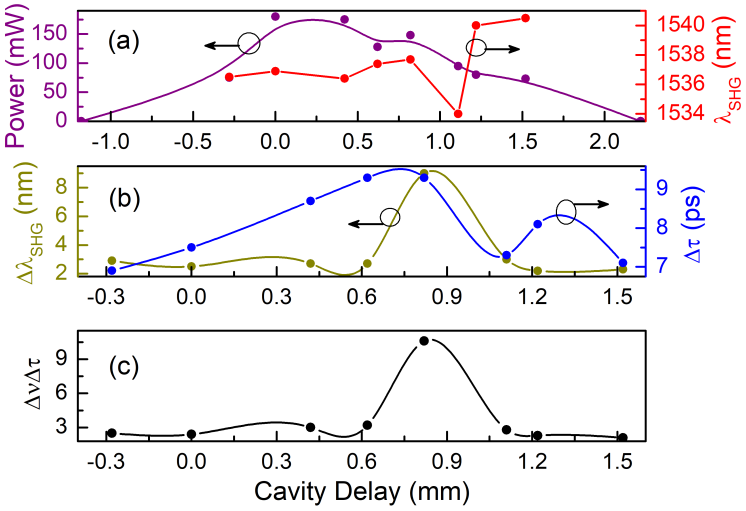

Figure 4.14: (a) SHG power and wavelength as a function of cavity delay. (b) FWHM of SHG wavelength and SHG pulse duration (measured using interferometric autocorrelation) versus cavity delay. (c) Calculated SHG frequency-time bandwidth as a function of cavity delay.

Figure 4.13(b), leading to a time-bandwidth product of $\Delta\nu\Delta\tau$ ~4.8. The measurements were also performed at the lower and higher ends of the SHG wavelengths, we recorded ~11 ps pulse duration at 1290 nm ($\Delta\lambda$ ~10.2 nm, $\Delta\nu\Delta\tau$ ~17.4). At maximum SHG wavelength of 1537 nm, the pulse duration is typically ~7.5 ps and spectral width is ~2.5 nm leading to $\Delta\nu\Delta\tau$ ~2.4. The time-bandwidth product for SHG wavelength at 1290 nm is quite large because the corresponding resonating idler at 2580 nm is much broader spectrally, as with increasing crystal (C_1 in Figure 4.1) temperature, the OPO goes towards degeneracy and hence the gain bandwidth gets larger thereby supporting multiple idler wavelengths to resonate inside the cavity simultaneously. We also performed an interferometric autocorrelation measurement for the cavity detuning at gain crystal temperature of 25 °C in order to minimize thermal fluctuations in the OPO and the data is shown in Figure 4.14. The total cavity delay was found to be 3.4 mm. As the cavity delay was changed from -1.18 mm to 2.22 mm, the measured SHG power (Figure 4.14(a)) changed from zero to zero with maximum power of ~148 mW at 0.82 mm cavity delay. The change in SHG wavelength as a function of cavity delay is shown in Figure 4.14(a). The corresponding measured FWHM of SHG wavelengths along with pulse durations (measured using interferometric autocorrelation) and the

calculated frequency-time bandwidths are shown in Figure 4.14(b)–(c) respectively.

4.4 Conclusions

In conclusion, we have reported the first high-average-power, high-repetition-rate, picosecond intracavity-SHG-ring cavity OPO based on 5%MgO:PPLN covering the 1.27-1.45 μm region while pumped at 1.064 μm. We have generated a broadly tunable radiation across 2610-3075 nm in the idler, 1627-1782 nm in the signal and 1272-1537 nm in the SHG with >1 W average output power in the 1290-1375 nm region. This generic technique of using a fanout-grating PPLN crystal for intracavity-SHG of an idler-resonant OPO allows the possibility of covering the entire tuning range right from the pump wavelength at 1064 nm to >4000 nm in a single device with high-average-power through-out the tuning range which has not been possible until now.

References

[1] S. Adachi, T. Oguchi, H. Tanida, S. Y. Park, H. Shimizu, H. Miyatake, N. Kamiya, Y. Shiro, Y. Inoue, T. Ueki and T. Iizuka, "The RIKEN structural biology beamline II (BL44B2) at the Spring-8," *Nuclear Instruments and Methods in Physics Research Section A: Accelerators, Spectrometers, Detectors and Associated Equipment* **467**, 711-714 (2001).

[2] J. L. Machol, R. M. Hardesty, B. J. Rye, and C. J. Grund, "Proposed compact, eye-safe lidar for measuring atmospheric water vapor," in *Advances in Atmospheric Remote Sensing with Lidar*, A. Ansmann, R. Neuber, P. Rairoux, and U. Wandinger, eds. (Springer, 1997), pp. 321–324.

[3] E. O. Potma, and X. S. Xie, "CARS Microscopy for Biology and Medicine," *Optics & Photonics News* **15**, 40-45 (2004).

[4] J. Qin, L. Shi, S. Dziennis, R. Reif, and R. K. Wang, "Fast synchronized dual-wavelength laser speckle imaging system for monitoring hemodynamic changes in a stroke mouse model," *Opt. Lett.* **37**, 4005-4007 (2012).

[5] J. Wang, Y. Wang, B. Li, D. Feng, J. Lu, Q. Luo, and P. Li, "Dual-wavelength laser speckle imaging to simultaneously access blood flow, blood volume, and oxygenation using a color CCD camera," *Opt. Lett.* **38**, 3690-3692 (2013).

[6] S. Chaitanya Kumar, J. Wei, J. Debray, V. Kemlin, B. Boulanger, H. Ishizuki, T. Taira, and M. Ebrahim-Zadeh, "High-power, widely tunable, room-temperature picosecond optical parametric oscillator based on cylindrical 5%MgO:PPLN," *Opt. Lett.* **40**, 3897-3900 (2015).

[7] K. Devi, S. Chaitanya Kumar, and M. Ebrahim-Zadeh, "High-power, continuous-wave, single-frequency, all-periodically-poled, near-infrared source," *Opt. Lett.* **37**, 5049-5051 (2012).

[8] V. Ramaiah-Badarla, S. Chaitanya Kumar, and M. Ebrahim-Zadeh, "Fiber-laser-pumped, dual-wavelength, picosecond optical parametric oscillator," *Opt. Lett.* **39**, 2739-2742 (2014).

[9] B. Nandy, S. Chaitanya Kumar, J. C. Casals, H. Ye, and M. Ebrahim-Zadeh, "Tunable high-average-power optical parametric oscillators near 2μm," *J. Opt. Soc. Am. B* **35**, C57-C67 (2018).

[10] K. C. Burr, C. L. Tang, M. A. Arbore, and M. M. Fejer, "Broadly tunable mid-infrared femtosecond optical parametric oscillator using all-solid-state-pumped periodically poled lithium niobate," *Opt. Lett.* **22**, 1458-1460 (1997).

[11] L. E. Myers, R. C. Eckardt, M. M. Fejer, R. L. Byer, and W. R. Bosenberg, "Multigrating quasi-phase-matched optical parametric oscillator in periodically poled LiNbO3," *Opt. Lett.* **21**, 591-593 (1996).

[12] S. Parsa, S. Chaitanya Kumar, B. Nandy, and M. Ebrahim-Zadeh, "Yb-fiber-pumped, high-beam-quality, idler-resonant mid-infrared picosecond optical parametric oscillator", *Opt. Express* **27**, 25436-25444 (2019).

[13] M. Ebrahim-Zadeh, S. French, and A. Miller, "Design and performance of a singly resonant picosecond LiB_3O_5 optical parametric oscillator synchronously pumped by a self-mode-locked Ti:sapphire laser," *J. Opt. Soc. Am. B* **12**, 2180-2191 (1995).

[14] F. Kienle, D. Lin, S. Alam, S. S. Hung, C. B. E. Gawith, H. E. Mahor, D. J. Richardson, and D. P. Shepherd, "Green-pumped, picosecond MgO:PPLN optical parametric oscillator," *J. Opt. Soc. Am. B* **29**, 144-152 (2012).

[15] S. Chaitanya Kumar, S. Parsa, and M. Ebrahim-Zadeh, "Fiber-laser-based, green-pumped, picosecond optical parametric oscillator using fan-out grating PPKTP," *Opt. Lett.* **41**, 52-55 (2016).

5

High-average-power, stable, compact and highly tunable picosecond optical parametric oscillator

This chapter constitutes the following publication:

1. **B. Nandy**, S. Chaitanya Kumar, and M. Ebrahim-Zadeh, "High-average-power, stable, compact and highly tunable picosecond optical parametric oscillator". (To be submitted)

5.1 Background and motivation

High-power picosecond mid-infrared optical parametric oscillators (OPO) are of great interest due to their broad applications in fields spanning from physics to biological and medical sciences [1-8]. Although such sources are now matured and well-established, providing Watt-level output powers across the near- to mid-IR in robust architectures, due to the requirement of synchronous pumping, they typically tend to be relatively bulky and of large size, with cavity lengths matched to that of the pump laser. A typical synchronously-pumped picosecond OPO with ~80 MHz pulse repetition rate has round trip cavity length of ~3.77 m, which can restrict its practical utility in space-constrained applications. This restriction also becomes increasingly important at lower pulse repeti-

tion rates approaching few MHz, where higher pulse energies are desired in applications such as three-photon microscopy [9]. In 2001, Südmeyer *et. al.* demonstrated the first synchronously pumped fiber-feedback OPO where a single-mode fiber represented most of the OPO cavity length [10]. In spite of the high fiber coupling loss at the fiber launch, high conversion efficiency can be achieved by using a high parametric gain medium. Using this concept, compact, stable and efficient systems were demonstrated in the femtosecond and picosecond regimes [11, 12] using a ring cavity configuration which happens to be very difficult to build and align and requires additional optical components which also contributes towards development challenges.

In this chapter, we present a high-average-power, highly stable (both power and spectrum) with immaculate beam quality, widely tunable, compact and easy to align, fiber-feedback picosecond OPO using a 80-cm-long single-mode IMRF in X-cavity configuration, resulting in a two-fold reduction in the overall footprint while operating at 79.5 MHz repetition rate.

5.2 Experimental Setup

The schematic of the experimental configuration of the IMRF picosecond OPO is depicted in Figure 5.1. The OPO is synchronously pumped by a mode-locked Yb-fiber laser (Fianium, $FP1060-20$) delivering up to 20 W of average power at a central wavelength of 1064 nm with a full-width-at-half-maximum (FWHM) spectral bandwidth of $\Delta\lambda_p$ ~1 nm, in pulses of ~20 ps duration at a ~79.5 MHz repetition rate. After attenuation optics for systematic input power control, an average pump power of ~8.8 W is focused to a waist radius of w_0 ~60 μm at the center of the nonlinear crystal, which is 42-mm-long MgO:PPLN with seven separate grating periods from Λ=28.5-31.5 μm each of cross-section size 1mm X 1mm. The crystal faces are antireflection-coated for the pump and signal (R<1%) with high transmission (R<7%) for the idler. The OPO is configured as a singly-resonant oscillator (SRO) in a folded standing-wave cavity formed by two concave mirrors (r=-100 mm), a plane output coupler (OC) in one arm, and the IMRF completing the cavity in the other arm. The signal is extracted through ~50% OC, while the idler exits the cavity in a single pass. The IMRF comprises a single-mode fiber (SMF-28) incorporating an integrated retro-reflector end-mirror with high reflectivity (R>98%) over the entire resonant signal wavelength range of 1451-2051 nm and

the SMF-28 fiber is specified to be single-mode over the wavelength range of 1260-1625 nm.

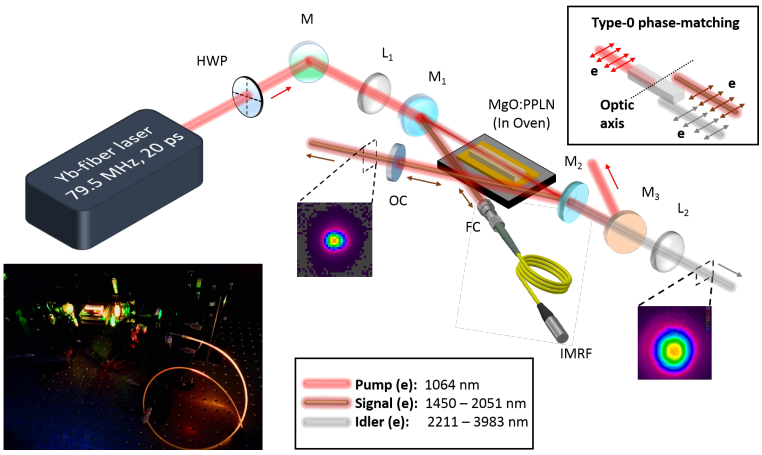

Figure 5.1: Experimental setup of the compact IMRF picosecond OPO. HWP: Half-wave plate, M: Mirrors, L: Lens, FC: Fiber coupler, IMRF: Integrated-mirror-retro-reflector fiber, OC: Output coupler, F: Filter. Inset: Laboratory photograph of the IMRF picosecond OPO.

5.3 Device tuning and characterization

Figure 5.2 shows the wavelength tuning range and the average output power of the IMRF picosecond OPO which is achieved by varying the PPLN crystal temperature at various grating periods. Watt-level output power is achieved over almost the whole tuning range of the signal and idler. As shown in Figure 5.2(a), the idler wavelength is tunable from 2211-3983 nm (total 1772 nm) with maximum output power of 0.96 W. And Figure 5.2(b) shows the signal wavelength tuning from 1451-2051 nm (total 600 nm) with maximum power of 0.94 W along with the transmission curve of the OC for the signal wavelength which varies from 26%-90% transmission over the signal tuning range with a ~30% transmission at 1550 nm. The sharp dip in the signal power near 2040 nm is due to the strong reflection of the AR-coating of the fiber coupler which reflects back most of the signal wave thereby blocking the signal wave from entering the fiber and resulting in reduction of the resonant intra-cavity power below the threshold of the OPO. The sharp decline in the idler power near 2210 nm is due to the loss of

signal power near 2040 nm. The sudden changes in power levels in both the signal and idler are due to change of grating period.

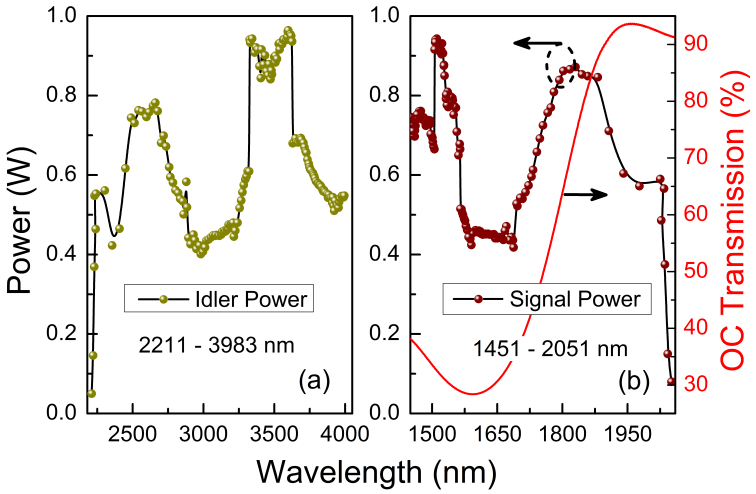

Figure 5.2: Tuning range and average output power of the IMRF picosecond OPO. (a) Output power over the idler tuning range of 2211 to 3983 nm. (b) Output power over the signal tuning range of 1451 to 2051 nm and the corresponding transmission curve for the OC.

We performed the power scaling of the signal and idler waves with respect to the pump power and also measured the pump depletion. As shown in Figure 5.3, we obtained a slope efficiency of ~21.3% for the signal power at 1550 nm with maximum signal power of 0.49 W at 9 W pump power and about ~24.4% for the idler power at 3393 nm with maximum idler power of 0.58 W at 9 W pump power and maximum pump depletion of ~37.1%.

In addition to temperature tuning, we also investigated cavity-delay tuning of the IMRF OPO for a fixed input pump power of 9 W, at a crystal temperature of ~50 °C for the grating period of 30.5 μm. The signal and idler output power as a function of cavity detuning is shown in Figure 5.4. As the cavity length is adjusted from -650 μm to zero detuning, the signal power (idler power) increases from 1 mW (2 mW) to a maximum of 486 mW (554 mW), beyond which it decreases to 2 mW (5 mW) at +350 μm of detuning. The signal and idler power from the IMRF OPO varies asymmetrically with respect to the zero detuning, which corresponds to the maximum signal and idler output power, and is more sensitive to the positive detuning. In the X-cavity configuration,

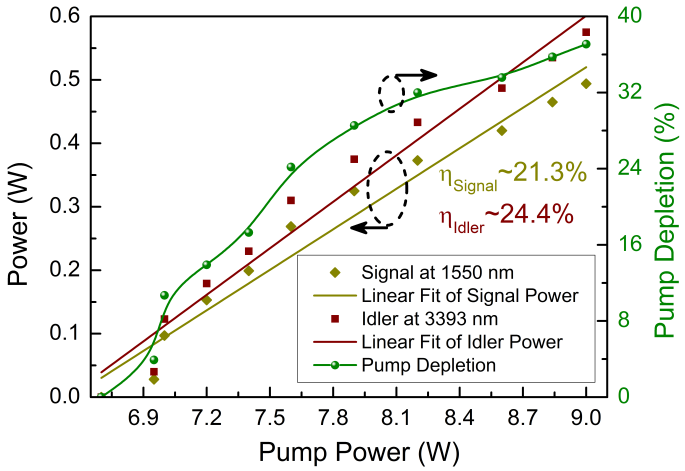

Figure 5.3: Signal and Idler power scaling of the IMRF OPO using a 50% signal OC.

this detuning corresponds to a total time delay of ~6.6 ps, compared to ~15.3 ps for a normal SRO where the fiber is replaced by a plain metallic mirror while everything else remains the same for the sake of comparison. Although the OPO oscillation was maintained over the entire 1 mm cavity tuning length detuning range, we observed an overall signal tuning of only ~2 nm, corresponding to ~10 nm of idler tuning in the mid-IR for the IMRF OPO. This could be attributed to the nonlinearity of the ~80 cm long (effective length of ~1.6 m for the signal due to retro-reflection) SMF28 fiber around 1550 nm, which limits the tuning range. Also shown in the insets of Figure 5.4 are the signal spectra with negative detuning and at perfect synchronization. We obtain both single-peak and double-peak spectrum by tuning the cavity delay, where the double-peak spectrum is a result of increased circulating signal intensity leading to enhanced self-phase-modulation.

We further characterized the IMRF-OPO with regard to signal and idler power stability by performing measurements of long-term average-power fluctuations, with the results shown in Figure 5.5. The signal power as shown in Figure 5.5(a) exhibits a passive power stability of better than 0.8% rms over 3 h, while operating at full power and at a signal wavelength of 1550 nm, similarly, the idler power as shown in Figure 5.5(b) exhibits a passive power stability of better than 0.7% rms over 3 h, operating at full power and at idler wavelength of 3393 nm. Whereas, for the normal

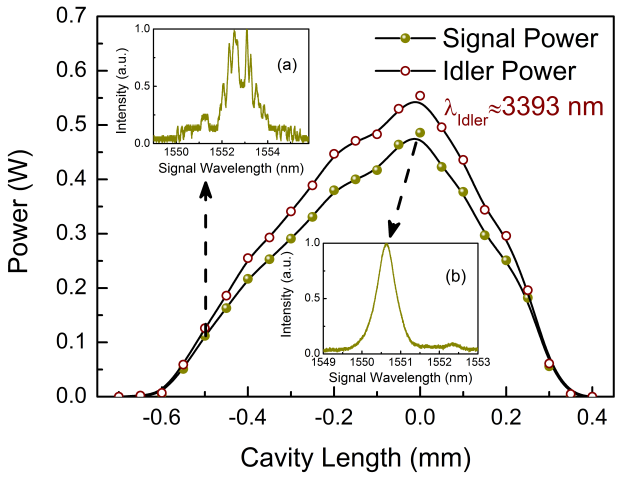

Figure 5.4: Variation of the signal and idler power as a function of the picosecond IMRF OPO cavity delay. Inset: signal spectra (a) away, and (b) at perfect synchronization.

SRO, we obtained power stability of 1.4% rms for signal and 0.5% rms for the idler over 3 h. The pump laser exhibits a power stability of ~0.2% rms over a similar period of time.

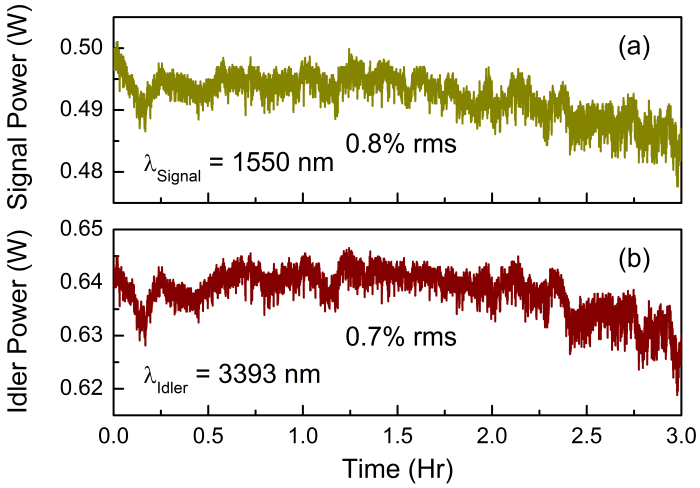

Figure 5.5: Long-term power stability of the output waves from the IMRF picosecond OPO. (a) Signal power stability at ~1550 nm over 3 hrs. (b) Idler power stability at ~3393 nm over 3 hrs.

We further recorded the spatial quality of the output beam from the IMRF OPO. Using a focusing lens of focal length, f=50 mm, and a scanning beam profiler, we measured the M^2-value of the output beams, resulting in M_x^2 <1.1 and M_y^2 <1 for the signal at 1550 nm, as shown in Figure 5.6(a) and M_x^2<1 and M_y^2<1.1 for the idler, as shown in Figure 5.6(b). The signal and idler beams were also observed to exhibit high spatial quality with single-mode Gaussian distribution, as presented in the inset of Figure 5.6(a)-(b).

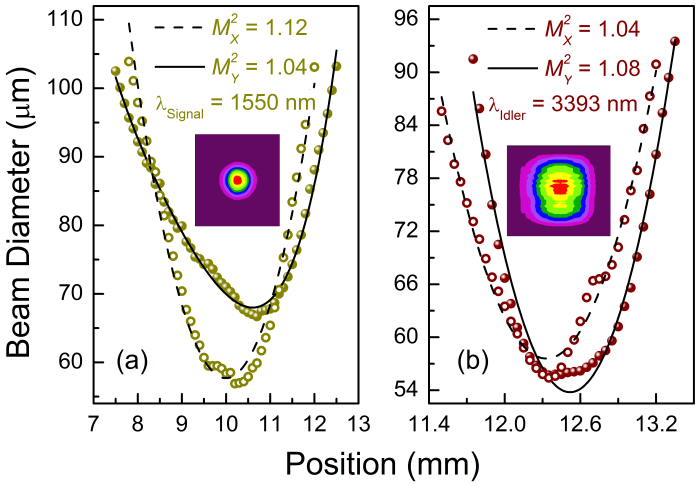

Figure 5.6: Beam quality measurements of the signal and the idler of the IMRF OPO. (a) M^2 measurements of the signal at 1550 nm. Inset: Spatial beam profile of the signal. (b) M^2 measurements of the idler at 3393 nm. Inset: Spatial beam profile of the idler.

As shown in Figure 5.7, we obtained excellent spectral stability of the signal beam over 1 h. We performed the spectral stability measurements for the single and double-peak by tuning the cavity delay length. We obtained 0.004% rms spectral stability for the double-peak signal spectrum as shown in Figure 5.7(a), and about 0.003% rms spectral stability for the single-peak signal spectrum as shown in Figure 5.7(b). We also measured the FWHM stability of the single-peak signal spectrum over 1 h and obtained 1.864% rms as shown in Figure 5.7(c). We had also measured the signal spectrum stability of the normal SRO at 1550 nm for the sake of comparison and obtained 0.01% rms over 1 h.

The duration of the signal pulses were measured by interferometric autocorrelation as shown in Figure 5.8(a). We observed that the nonlinear effects in the fiber lead to

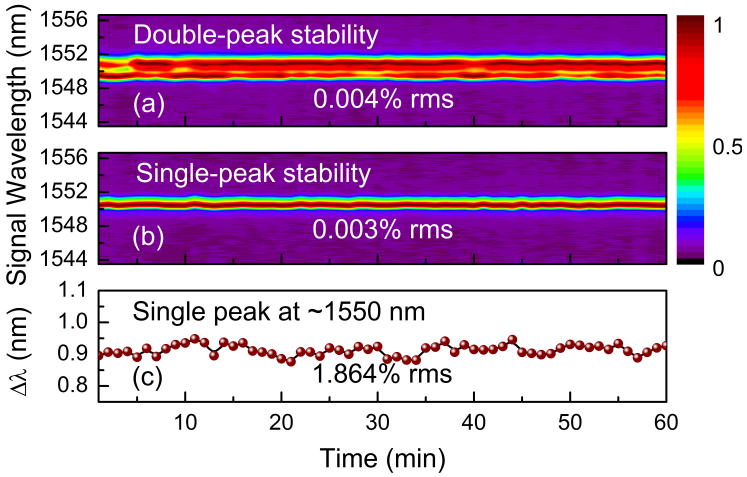

Figure 5.7: Spectral stability of the signal output of the IMRF OPO around 1550 nm over the duration of 1 h. (a) Double-peak spectrum stability over 1 h. (b) Single-peak spectrum stability over 1 h. (c) FWHM stability of the single-peak spectrum over 1 h.

temporal shortening of the seed pulses and the measured pulse duration (FWHM) of the signal pulse of the IMRF OPO at 1550 nm is typically ~10.6 ps, assuming sech^2 pulse shape. The spectral width is approximately 0.7 nm (FWHM) as shown in Figure 5.8(b), leading to a time-bandwidth product of $\Delta\nu\Delta\tau$ ~0.93. We compared the measurements to a normal SRO and we obtained signal pulses of ~23.7 ps at 1550 nm with spectral width of ~0.9 nm, leading to a time-bandwidth product of $\Delta\nu\Delta\tau$ ~2.7. The pump pulses had a time-bandwidth product of $\Delta\nu\Delta\tau$ ~5.3. We simultaneously measured the pulse train stability of the signal and pump pulses and found it to be around ~5.2% rms and ~4.6% rms over 20 ms. The pulse repetition-rate stability for both the signal and idler pulses of the IMRF OPO turned out to be ~0.00001% rms over 3 h.

5.4 Conclusions

In conclusion, to the best of our knowledge, we have demonstrated the first synchronously pumped picosecond IMRF OPO that uses a 80 cm long SMF28 fiber with integrated mirror. This IMRF OPO concept results in a very robust, compact and highly tunable light source which uses a Yb-fiber laser at 1064 nm as input pump and generates output waves from 1451-3983 nm with excellent power and spectral stability,

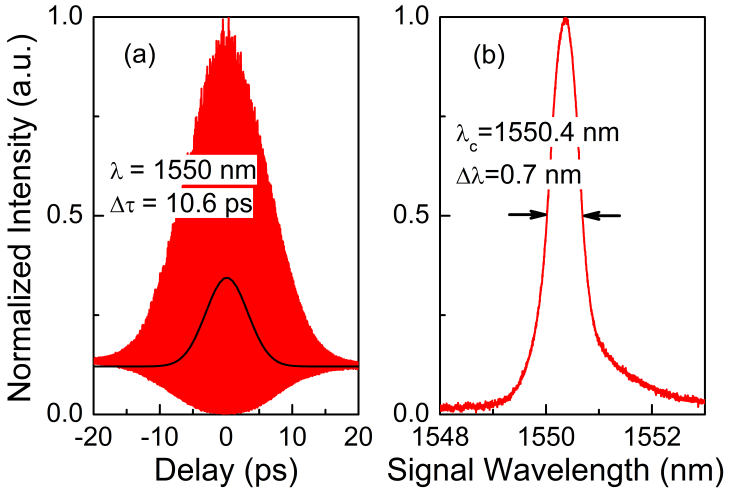

Figure 5.8: (a) Interferometric autocorrelation and (b) optical spectrum of the signal wave at 1550 nm for the IMRF OPO.

along with immaculate beam quality of TEM_{00} mode profile. The IMRF OPO provides as much as 0.96 W of idler power at 3598 nm and 0.94 W of signal power at 1511 nm, with >0.4 W over almost the entire tuning range. The IMRF OPO exhibits a passive signal and idler power stability of better than 0.8% rms and 0.7% rms over 3 h in excellent beam quality with M^2 values better than 1.1 for both the signal and idler beams. The spectral stability of this OPO is extremely good with ~0.003% rms over 1 h. The signal pulses extracted from the IMRF OPO exhibit a Gaussian temporal duration of ~10.6 ps at 1550 nm having a time bandwidth product of $\Delta\nu\Delta\tau$ ~0.93 where the shortening of the pulses is due to the nonlinear effects of the fiber and hence the pulse duration varies with change in the resonant signal wavelength due to the dependence of the refractive index on the wavelength.

With improvements in the fiber technology, improved AR-coatings for the fiber-coupling optics and use of high precision fiber alignment opto-mechanics for better fiber-coupling, will possibly pave the way for high average-output power, ultra-compact high repetition-rate, synchronously pumped picosecond OPOs which can be easily deployed in space-constrained applications and this technique can also be extended to deep-IR OPOs by using Fluoride based fibers.

References

[1] J. Qin, L. Shi, S. Dziennis, R. Reif, and R. K. Wang, "Fast synchronized dual-wavelength laser speckle imaging system for monitoring hemodynamic changes in a stroke mouse model," *Opt. Lett.* **37**, 4005-4007 (2012).

[2] J. Wang, Y. Wang, B. Li, D. Feng, J. Lu, Q. Luo, and P. Li, "Dual-wavelength laser speckle imaging to simultaneously access blood flow, blood volume, and oxygenation using a color CCD camera," *Opt. Lett.* **38**, 3690-3692 (2013).

[3] J. L. Machol, R. M. Hardesty, B. J. Rye, and C. J. Grund, "Proposed compact, eye-safe lidar for measuring atmospheric water vapor," in *Advances in Atmospheric Remote Sensing with Lidar*, A. Ansmann, R. Neuber, P. Rairoux, and U. Wandinger, eds. (Springer, 1997), pp. 321–324.

[4] S. Cha, K. P. Chan, and D. K. Killinger, "Tunable 2.1-μm Ho lidar for simultaneous range-resolved measurements of atmospheric water vapor and aerosol backscatter profiles," *Appl. Opt.* **30**, 3938-3943 (1991).

[5] S. W. Henderson, C. P. Hale, J. R. Magee, M. J. Kavaya, and A. V. Hauffaker, "Eye-safe coherent laser radar system at 2.1 μm using Tm, Ho: YAG lasers," *Opt. Lett.* **16**, 773-775 (1991).

[6] S. Ishii, K. Mizutani, H. Fukuoka, T. Ishikawa, B. Philippe, H. Iwai, T. Aoki, T. Itabe, A. Sato, and K. Asai, "Coherent 2 μm differential absorption and wind lidar with conductively cooled laser and two-axis scanning device," *Appl. Opt.* **49**, 1809-1817 (2010).

[7] D. Yan, Y. Wang, D. Xu, P. Liu, C. Yan, J. Shi, H. Liu, Y. He, L. Tang, J. Feng, J. Guo, W. Shi, K. Zhong, Y. H. Tsang, and J. Yao, "High-average-power, high-repetition-rate tunable terahertz difference frequency generation with GaSe crystal pumped by 2 μm dual-wavelength intracavity KTP optical parametric oscillator," *Photon. Res.* **5**, 82-87 (2017).

[8] P. J. Gilling, C. B. Cass, M. D. Cresswell, A. R. Malcolm, and M. R. Fraundorfer, "The use of the holmium laser in the treatment of benign prostatic hyperplasia," *J. Endourol.* **10**, 459-461 (1996).

[9] S. W. Hell, K. Bahlmann, M. Schrader, A. Soini, H. Malak, I. Gryczynski, and J. R. Lakowicz, "Three-photon excitation in fluorescence microscopy," *Journal of Biomedical Optics* **1**, 71-75 (1996).

[10] T. Südmeyer, J. Aus der Au, R. Paschotta, U. Keller, P. G. R. Smith, G. W. Ross, and D. C. Hanna, "Femtosecond fiber-feedback optical parametric oscillator," *Opt. Lett.* **26**, 3580-3582 (2001).

[11] T. Südmeyer, J. Aus der Au, R. Paschotta, U. Keller, P. G. R. Smith, G. W. Ross, and D. C. Hanna, "Novel ultrafast parametric systems: high repetition rate single-pass OPG and fibre-feedback OPO," *J. Phys. D: Appl. Phys.* **34**, 2433-2439 (2001).

[12] F. Kienle, P. S. Teh, S. Alam, C. B. E. Gawith, D. C. Hanna, D. J. Richardson, and D. P. Shepherd, "Femtosecond fiber-feedback optical parametric oscillator," *Opt. Lett.* **35**, 304-306 (2010).

6

Fiber-laser-pumped picosecond optical parametric generation and amplification in MgO:PPLN

This chapter constitutes the following publication:

1. **B. Nandy**, S. Chaitanya Kumar, and M. Ebrahim-Zadeh, "Fiber-laser-pumped picosecond optical parametric generation and amplification in MgO:PPLN," *Opt. Lett.* (In Press).
2. S. Chaitanya Kumar, **B. Nandy**, and M. Ebrahim-Zadeh, "Performance studies of high-average-power picosecond optical parametric generation and amplification in MgO:PPLN at 80 MHz". (submitted in *Opt. Express*)

6.1 Background and motivation

The generation of high-repetition-rate picosecond pulses at high average power is of great interest for a variety of applications including spectroscopy [1] and material processing [2]. The development of tunable picosecond sources in the 2 μm wavelength range is of particular interest for applications in LIDAR [3] and laser processing of biological tissues [4]. While mode-locked Thulium and Holmium laser technologies have been extensively investigated for generating coherent radiation in the 2 μm wavelength range, they offer limited tunability [5]. On the other hand, synchronously-pumped optical parametric oscillators (OPOs) pumped by Yb-fiber lasers at 1064 nm are es-

tablished as reliable sources of high-repetition-rate picosecond pulses across the near- to mid-infrared at multi-Watt average power levels [6]. However, a major challenge in the development of ultrafast OPOs is the requirement for cavity length synchronization with input pump pulse repetition rate, which also dictates the minimum system size. For wavelength generation near 2 μm, such OPOs must also be operated near degeneracy, hence requiring careful cavity design for reliable performance [7, 8]. As a comparatively simple single-pass process, optical parametric generation (OPG) and amplification (OPA) can overcome some of the practical operational difficulties, system complexity, size, and high cost associated with ultrafast OPOs. Using OPG-OPA schemes, access to wavelength regions near 2 μm has been achieved using birefringent nonlinear materials such as β-BaB_2O$_4$ [9], BiB_3O_6 [10] and $KTiOPO_4$ [11]. However, such systems rely on high pump pulse energies at low repetition rates for efficient conversion. On the other hand, MgO-doped periodically-poled $LiNbO_3$ (MgO:PPLN) offers high nonlinearity (deff~16 pm/V), improved optical quality, and noncritical phase-matching in long interaction lengths (up to 80 mm). These properties open up the possibility for realizing efficient single-pass OPG-OPA sources using low-energy picosecond pulses at high repetition rates in a practical, simplified and compact architecture. This also presents the opportunity for the development of efficient, high-average-power, high-repetition-rate picosecond sources near 2 μm based on OPG-OPA approach, as we demonstrate here.

Earlier reports on single-pass picosecond OPG sources include a 55-mm-long PPLN crystal pumped by a mode-locked $NdYVO_4$ oscillator-amplifier system at 1064 nm with 7 ps pulses at 82 MHz repetition rate. The single-stage OPG device provided tunable radiation over 1571-1642 nm in the signal and 3026-3302 nm in the idler with a maximum total average power of 8.9 W for 24 W of pump at 37% conversion efficiency, with an OPG threshold of 4 W [12]. The output power was further increased to 9.5 W by injection seeding the OPG with a continuous-wave (cw) source at 1580 nm. In another report, a 40-mm-long MgO:PPLN crystal was used for a single-stage OPG pumped at 1035 nm by a mode-locked Yb-fiber master oscillator-power amplifier system, providing 150-ps pulses at 1 MHz repetition rate. The device generated tunable output over 1450-3615 nm with a maximum total power of 3.9 W for 12 W of pump power at 32.5% conversion efficiency, with an OPG average power threshold of ~5 W. Using a tunable cw seed, the output power was improved to 4.3 W, however, pumping beyond 9.2 W resulted in catastrophic damage to the MgO:PPLN crystal [13].

Here we report an efficient, high-average-power, picosecond source based on cascaded single-pass OPG-OPA scheme using two MgO:PPLN crystals pumped by an Yb-fiber laser at 80 MHz pulse repetition rate. The two-stage OPG-OPA system is tunable across 1902-2415 nm, including degeneracy, and provides up to 8.3 W of total output power for 14 W of pump power at a record conversion efficiency of ~59% with spectral bandwidth as large as ~350 nm (10 dB level) at a central wavelength of 2107 nm. The output exhibits excellent passive power and spectral stability better than 0.9% rms and 0.1% rms, respectively, over 1 hour, in high spatial beam quality. To the best of our knowledge, this is the first report of such cascaded OPG-OPA scheme in the picosecond time domain and the highest conversion efficiency and lowest threshold ever achieved in single-pass parametric generation. The high average power and record efficiency together with short pulse durations and broad spectral bandwidths over a wide wavelength range, including the 2 μm region, are some of the key attributes of this compact and simple single-pass OPG-OPA system.

6.2 Experimental Setup

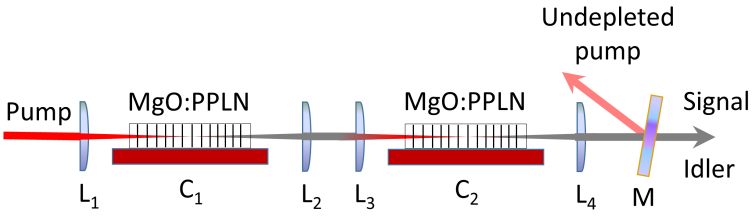

Figure 6.1: Schematic of the picosecond OPG-OPA setup. L_1: f=200 mm, L_2: f=150 mm, L_3: f=100 mm. The total physical length of OPG-OPA system is ~70 cm.

The schematic of the experimental setup is shown in Figure 6.1. The device consists of two nonlinear frequency conversion stages of OPG and OPA. The pump laser is a mode-locked Yb-fiber laser (Fianium, $FP1060-20$) operating at a central wavelength of 1064 nm with a full-width-half-maximum (FWHM) spectral bandwidth of $\Delta\lambda_p$ ~1.5 nm, in pulses of ~21 ps duration at 80 MHz repetition rate. After attenuation optics and polarization control, an average pump power of ~14 W is available at the input to the OPG stage. The nonlinear crystal for the OPG stage is a 50-mm-long, 2-mm-wide, 1-mm-thick MgO:PPLN crystal, C_1, with a single QPM grating period of Λ=32.16

μm, for type-0 ($e \Rightarrow ee$) parametric generation. The pump beam is focused to a waist radius of w_{01} ~52 μm (ξ_1 ~1.4) at the center of the crystal. The OPA stage comprises a MgO:PPLN crystal, C_2, identical to that used for the OPG stage. Both crystals are antireflection (AR)-coated (R<0.5%) at 1064 nm and 2050-2150 nm, with high transmission (R<10%) over 2250-4300 nm. Owing to the depleted pump beam profile and ~9% transmission loss through L_2 and L_3, the output from the OPG stage together with the undepleted pump is collimated and re-focused to a waist radius of w_{02} ~39 μm (ξ_2 ~2.6) at the center of C_2 in the OPA stage. Both the crystals are mounted on independent ovens providing temperature control from 25 °C to 200 °C with a stability of 0.1 °C. The output after the OPA stage is re-collimated and separated from the undepleted pump using a dichroic mirror, M, with R>99.9% at 1064 nm, T>99% over 1605-2128 nm, and T>86% over 2128-2415 nm.

6.3 Device tuning and characterization

Initially, we investigated the wavelength tuning characteristics of the OPG-OPA system. Tuning was performed by simultaneously changing the temperature of the MgO:PPLN crystals in the two stages. The output spectral evolution as a function of the simultaneously varied C_1 and C_2 crystal temperatures, measured after the OPA stage, is presented in Figure 6.2(a). The spectra were measured using a spectrometer for the 800-2600 nm wavelength range with a resolution of <0.5 nm. By simultaneously varying the temperature of C_1 and C_2 crystals, the source provides central wavelength tuning over 1902-2415 nm, corresponding to an overall tuning range of 513 nm, which also covers degeneracy. The group velocity mismatch between the pump and signal is estimated to be 115 ± 1.6 fs/mm across the tuning range, in MgO:PPLN, resulting in a temporal walk-off length >185 mm, much greater than the 50 mm length of C_1 and C_2 crystals. As the temperature is increased from 30 °C to 50 °C, the generated signal and idler beams evolve as independent branches. Further increasing the temperature beyond 50 °C results in a single broad spectrum, owing to the large gain bandwidth of the MgO:PPLN crystal as we approach degeneracy. The theoretically calculated degenerate phase-matching temperature for MgO:PPLN with a grating period of Λ=32.16 μm, when pumping at 1064 nm, is 78.6 °C, providing a gain bandwidth of ~155 nm centered at 2128 nm for the 50-mm-long crystal.

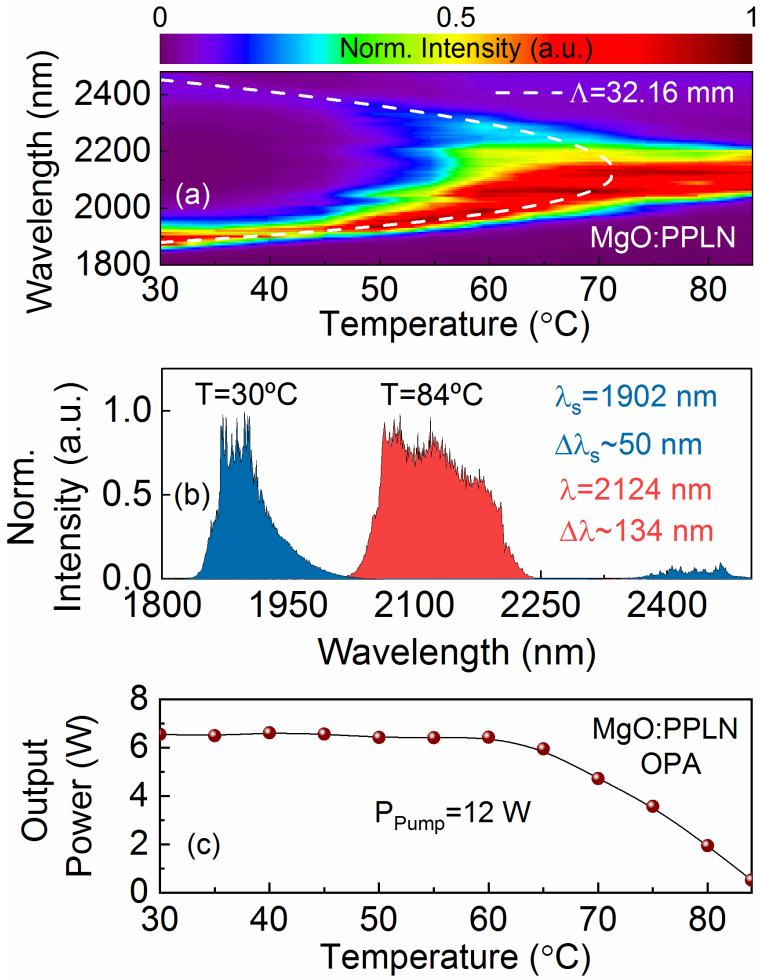

Figure 6.2: (a) Output spectral evolution (b) output spectra and (c) total output power measured after the OPA stage as a function of the simultaneously varied MgO:PPLN crystal temperature.

All measurements presented in Figure 6.2 were performed for an average pump power of 12 W at the input to the OPG stage, corresponding to a peak intensity of 85 MW/cm^2 in C_1. This high intensity, together with the pump beam divergence, further increases the gain bandwidth of the MgO:PPLN crystal for OPG and OPA processes, not only affecting the generated signal and idler bandwidths, but also their central wavelengths. The calculated temperature tuning curve for 1064 nm pumped OPG in MgO:PPLN with a grating period of Λ=32.16 μm, in the high-gain limit is also shown in Figure 6.2(a) for comparison, indicating good agreement with the measured central

wavelengths. The spectra recorded at the output of the OPA stage at two extreme operating temperatures are presented in Figure 6.2(b). At a temperature of 30 °C, the signal spectrum is centered at 1902 nm with a FWHM bandwidth of ~50 nm. Although weak, the corresponding idler spectrum centered at 2415 nm can also be seen towards the longer wavelength side in Figure 6.2(b). Similar measurement at 84 °C resulted in an output spectrum centered at 2124 nm with a FHWM bandwidth of 134 nm. We also measured the total power (signal plus idler) across the tuning range after the OPA stage, with the results presented in Figure 6.2(c). As evident, for an input pump power 12 W, the output power remains constant at 6.5 W while varying the temperatures of C_1 and C_2 from 30 °C to 60 °C, corresponding to signal central wavelengths ranging from 1902 to 2087 nm. Increasing the temperature above 60 °C results in a drop in output power to a minimum of 520 mW at 84 °C corresponding to a central wavelength of 2124 nm.

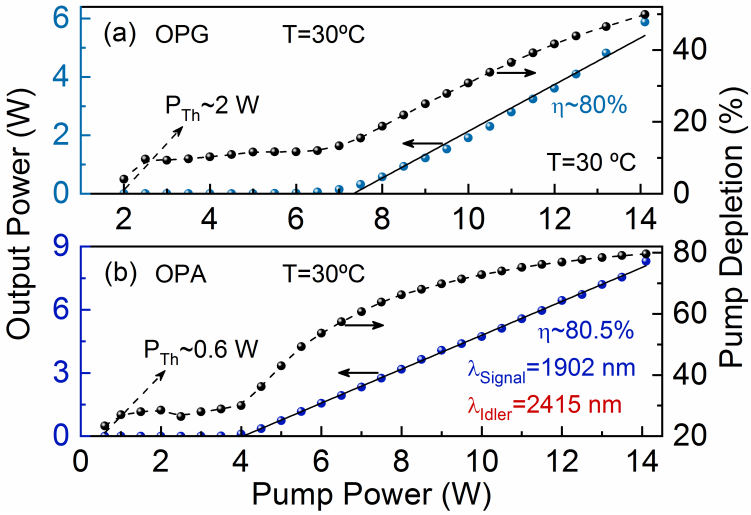

Figure 6.3: Power scaling characteristics of (a) OPG and (b) OPA stages at an operating temperature of 30 °C.

We further performed power-scaling characterization of both OPG and OPA stages independently. The results are presented in Figure 6.3. The output power from the OPG stage, together with the simultaneously measured pump depletion, as a function of the pump power at a temperature of 30 °C are shown in Figure 6.3(a). For a maximum input pump power of 14 W, we were able to generate up to 5.9 W of total (signal plus idler) output power, corresponding to a conversion efficiency of 42%. Although

a linear growth in output power with a slope efficiency of 80% is recorded above 7 W of pump power at the input to the OPG stage, using a power meter with a sensitivity of 1 μW, we were able to record the threshold of the OPG to be as low as ~2 W but it could be lower and we were limited by the sensitivity of the power meter. A maximum pump depletion of ~50% is recorded after the OPG stage. Similar power scaling measurements were performed at the output of the OPA stage as a function of the pump power at the input to the OPG stage, at the same operating temperature of 30 °C for both C_1 and C_2 crystals. The results are presented in Figure 6.3(b). As evident, the maximum output power from the OPA stage is measured to be 8.3 W, corresponding to an overall external conversion efficiency of ~59%. To the best of our knowledge this is the highest conversion efficiency ever reported from OPG-OPA system in any time-scale. The spectrum presented in Figure 6.2(b), for a temperature of 30 °C, corresponds to the OPA output while generating the maximum power of 8.3 W. Hence, from the measured spectral distribution and energy conservation, we estimated a signal power of 7.2 W at 1902 nm and an idler power of 1.1 W at 2415 nm.

It is to be noted that this idler power is not corrected for the 10% AR- coating loss on the output facets of both C_1 and C_2 crystals. These estimated signal and idler powers were also confirmed using a dichroic mirror different from M1 in Figure 6.1, which was AR-coated for high reflection at this specific operating signal wavelength and high transmission at the corresponding idler. We were not able to use this dichroic mirror, M, over the entire OPG-OPA experimental tuning range due to the increasing loss at longer wavelengths. Moreover, the AR-coatings for the collimation and focusing lenses were optimized for the signal, resulting in higher losses at the idler wavelengths. Hence, the lower idler powers compared to signal across the entire tuning range are due the inherently lower parametric gain at longer wavelengths as well as higher transmission losses through the optical components. While the slope efficiency in the OPA stage remains identical to that in the OPG at ~80.5%, the threshold pump power is further reduced drastically to ~600 mW, by a factor of >3 times compared to the OPG. This threshold power corresponds to a pump pulse energy of 7.5 nJ. We did not observe any damage in either to C_1 or C_2 crystals while pumping at 14 W of input power, generating a maximum of 8.3 W of output power at a pump depletion of ~80% after the OPA, leading to a 30% improvement in pump depletion compared to the OPG stage. Further, the output power from the OPA stage increases to practical levels beyond 4

W of input pump power, as opposed to 7 W in case of OPG. This is also evident from Figure 6.3, where the depletion remained minimal in the low gain limit. On the other hand, at higher pumping levels, the pump depletion increases linearly together with the output power in case of the OPG, while evidence of saturation is observed in the OPA stage. A nominal increase in conversion efficiency of ~17% and saturation of pump depletion in the OPA stage is attributed to the significant pump conversion in the OPG stage, resulting from operation in the high gain limit.

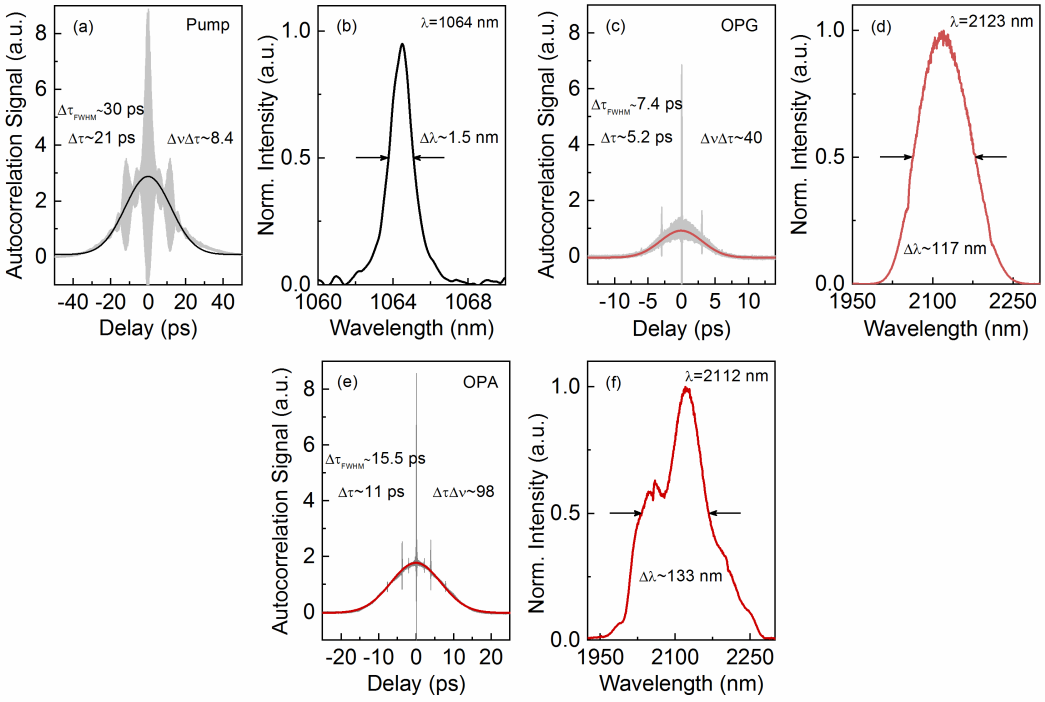

Figure 6.4: Interferometric autocorrelation trace and corresponding spectra of the (a, b) pump (c, d) OPG and (e, f) OPA respectively.

On the other hand, by simultaneously optimizing the phase-matching temperatures of C_1 and C_2 modified spectral and power performance can be achieved. We performed temporal characterization of the input pump as well as the generated output pulses from the OPG and OPA using an interferometric autocorrelator. The typical autocorrelation trace of the pump pulse, together with the corresponding spectrum centered at 1064 nm with an FWHM bandwidth of 1.5 nm, is shown in Figure 6.4(a,b). The pump pulses have FWHM duration of 30 ps, resulting in an estimated pulse duration of 21 ps, assuming Gaussian pulse shape. The output pulse duration from the OPG stage, mea-

sured at a central wavelength of at 2123 nm, was determined to be ~5.2 ps, as presented in Figure 6.4(c, d). With a FWHM spectral bandwidth of 117 nm, this results in a time-bandwidth product of $\Delta\tau\Delta\nu$ ~40, which ~4.8 times that of the input pump pulses, and >90 times the transform-limit for a Gaussian pulse. Moreover, the measured signal pulse duration of 5.2 ps indicates a pulse compression in the OPG stage by a factor of ~4 with respect to the input pump. Similar autocorrelation measurements of OPG output at other wavelengths resulted in pulse durations ranging from 5.6 ps at 1902 nm to 6.6 ps at 2106 nm. The autocorrelation measurements of OPA output resulted in Gaussian pulse duration of ~11 ps with a slightly larger FWHM spectral bandwidth of ~133 nm, as presented in Figure 6.4(e,f), with a corresponding time-bandwidth product of $\Delta\tau\Delta\nu$ ~98 and a pulse compression factor of ~2. The time-bandwidth product can be further improved by controlling the bandwidth using spectral narrowing techniques such as spectral filtering, injection seeding, or by deploying a diffraction grating for selecting a portion of the OPG output spectrum before amplification in the OPA stage. We also measured the idler pulse duration at the longest wavelength at the OPA output, where we were able to separate the signal and idler using a dichroic mirror. The measurement resulted in an idler pulse duration of ~5.9 ps at 2415 nm. To the best of our knowledge, the pulse duration of 5.2 ps in Figure 6.4(c) is the shortest generated in a high-average-power, high-repetition-rate, single-pass picosecond OPG scheme to date. This strong pulse compression is achieved due to the exponential gain available for OPG in MgO:PPLN in the high-gain limit.

In order to understand the origin of the observed pulse compression in our picosecond single-pass OPG, we performed theoretical simulations corresponding to the experimental conditions using the real laboratory values as input parameters. A Gaussian pump pulse with a 21 ps duration at 80 MHz and an input average pump power of 12 W at 1064 nm, focused to a beam waist of w_0 ~52 μm in a 50-mm-long MgO:PPLN crystal with a d_{eff} ~16 pm/V. The time-dependent parametric gain for OPG at a crystal temperature of 72 °C was then estimated, considering the time-varying input pump intensity leading to a $\Gamma_0 L$ ~19, corresponding to a peak pump intensity of ~85 MW/cm^2. The resulting temporal gain profile contributing to OPG in the high-gain limit then determines the generated output pulse duration. In Figure 6.5(a), the calculated normalized time-dependent parametric gain contributing to signal and idler pulse generation as a

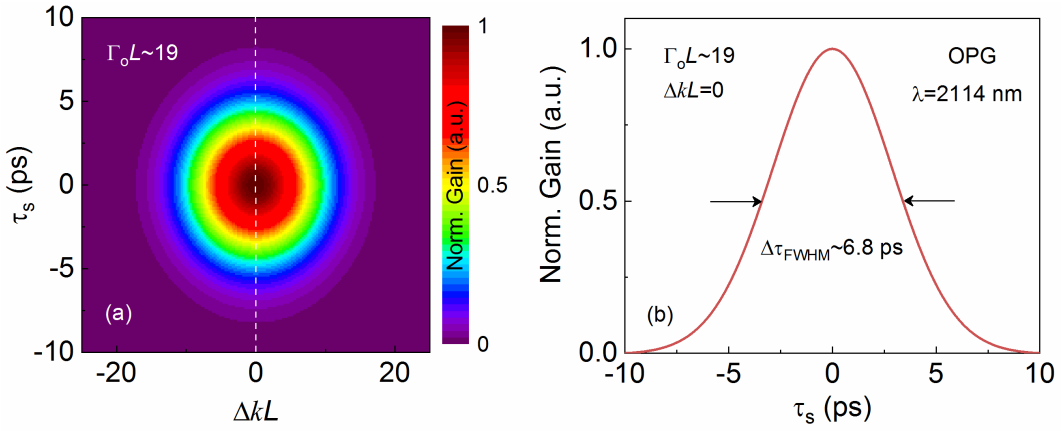

Figure 6.5: (a) Simulated normalized temporal gain profile for signal pulse generation as a function of the phase-mismatch parameter in the high-gain limit. (b) Normalized signal pulse profile in the high-gain limit for ΔkL=0.

function of the phase-mismatch parameter, ΔkL, is shown in a color-scale plot. The resulting temporal profile of the signal pulse in the OPG, for a phase-mismatch parameter, ΔkL=0, corresponding to the dotted line in Figure 6.5(a), is presented in Figure 6.5(b). This indicates an FWHM duration of ~6.8 ps, in close agreement with the experimental value of 7.4 ps, thus confirming the role of exponential parametric gain in the pulse compression observed in our experiments.

We also performed long-term power stability measurements of the output from OPA stage. As shown in Figure 6.6(a), the output exhibits excellent passive power stability better than 0.9% rms over 1 hour, compared to 0.1% rms for the pump over the same period, as presented in Figure 6.6(b). The output power stability can be improved by minimizing thermal fluctuations caused by the ovens housing C_1 and C_2, and by further thermal isolation of the entire system to reduce air currents. Also shown in the inset of Figure 6.6(a) is the spatial profile of output beam from the OPA, recorded using a pyroelectric camera at a distance of 1 m from C_2, confirming single-peak Gaussian profile with circularity of ~88%.

Finally, we recorded the long-term spectral stability of the OPA output at a central wavelength of 2078 nm, as shown in Figure 6.7, resulting in a central wavelength stability of 0.1% rms and a FWHM bandwidth stability of 11% rms, over 1 hour.

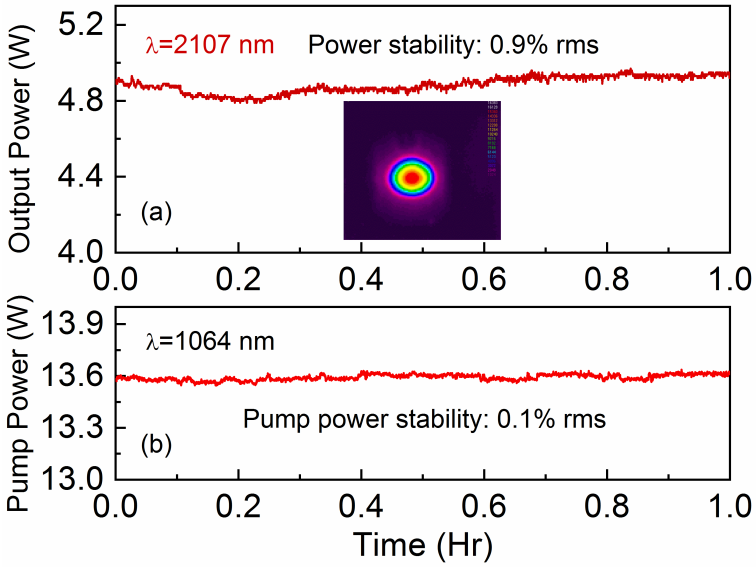

Figure 6.6: (a) Long-term power stability of the output from (a) OPA stage; inset: spatial profile of output beam. (b) Power stability of input pump.

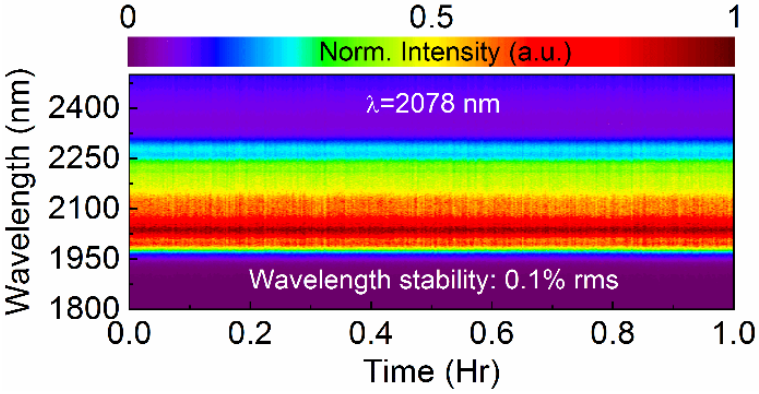

Figure 6.7: Long-term spectral stability of the output from the OPA stage operating a central wavelength of 2078 nm.

6.4 Conclusions

In conclusion, we have demonstrated an efficient, high-power picosecond source based on cascaded single-pass OPG-OPA in MgO:PPLN, for the first time to our knowledge, tunable over 1902-2415 nm, and delivering up to 8.3 W of average power at 80 MHz repetition rate, with record conversion efficiency of 59%. We have achieved a record threshold as low as 600 mW (7.5 nJ) and a pump depletion of ~80% in the single-pass

configuration. The generated output exhibits excellent passive power stability of 0.9% rms and central wavelength stability of 0.1% rms over 1 hour. We have generated FWHM spectral bandwidth of ~217 nm centered at 2107 nm, with 10dB bandwidth reaching ~350 nm. The ability to independently control the phase-matching condition in OPG and OPA stage enables fine control of central wavelength as well as the generated spectral bandwidth. Owing to the exponential parametric gain provided by the high nonlinearity and strong pump intensity in the 50-mm-long MgO:PPLN crystal, the source generates signal pulses of 5.2 ps duration from the OPG stage, corresponding to a 4 times temporal compression with respect to the pump across the tuning range. By deploying pump pulses of higher peak power and independent pump beam lines for the OPG and OPA stages, further enhancement of overall conversion efficiency and parametric gain can be achieved, leading to stronger pulse compression. Moreover, the ability to independently vary the phase-matching conditions in the OPG and OPA stage enables fine control of the central wavelength as well as the accessible spectral bandwidths. The use of further successive amplification stages could not only benefit power scaling, but also help relax the strong focusing condition, while operating in the high-gain limit. The development of this simple and compact high repetition-rate picosecond single-pass OPG-OPA source alleviates the need for complex synchronous cavities associated with SPOPOs, delivering multi-Watt average powers with short pulse duration, providing a cost-effective alternative for a variety of applications.

References

[1] S. Junaid, S. Chaitanya Kumar, M. Mathez, M. Hermes, N. Stone, N. Shepherd, M. Ebrahim-Zadeh, P. Tidemand-Lichtenberg, and C. Pedersen, "Video-rate, mid-infrared hyperspectral upconversion imaging," *Optica* **6**, 702-708 (2019).

[2] H. Kämmer, G. Matthäus, S. Nolte, M. Chanal, O. Utéza, and D. Grojo, "In-volume structuring of silicon using picosecond laser pulses," *Appl. Phys. A* **124**, 302-306 (2018).

[3] J. L. Machol, R. M. Hardesty, B. J. Rye, and C. J. Grund, "Proposed compact, eye-safe lidar for measuring atmospheric water vapor," in *Advances in Atmospheric Remote Sensing with Lidar*, A. Ansmann, R. Neuber, P. Rairoux, and U. Wandinger, eds. (Springer, 1997), pp. 321–324.

[4] N. M. Fried, and K. E. Murray, "High-power thulium fiber laser ablation of urinary tissues at 1.94 μm," *J. Endourol.* **19**, 25–31 (2005).

[5] I. T. Sorokina, V. V. Dvoyrin, N. Tolstik, and E. Sorokin, "Mid-IR Ultrashort Pulsed Fiber-Based Lasers," *IEEE J. Select. Topics Quantum Electron.* **20**, 0903412-12 (2014).

[6] M. Ebrahim-Zadeh and S. Chaitanya Kumar, "Yb-fiber-laser-pumped ultrafast frequency conversion sources from the mid-infrared to the ultraviolet", *IEEE J. Sel. Top. Quantum Electron.* **20**, 7600519-19 (2014).

[7] B. Nandy, S. Chaitanya Kumar, J. C. Casals, H. Ye, and M. Ebrahim-Zadeh, "Tunable high-average-power optical parametric oscillators near 2 μm," *J. Opt. Soc. Am. B* **35**, C57-C67 (2018).

[8] S. Chaitanya Kumar, and M. Ebrahim-Zadeh, "Yb-fiber-based, high-average-power, high-repetition-rate, picosecond source at 2.1 μm," *Laser & Photon. Rev.* **10**, 970-977 (2016).

[9] J. Y. Zhang, J. Y. Huang, Y. R. Shen, and C. Chen, "Optical parametric generation and amplification in barium borate and lithium triborate crystals," *J. Opt. Soc. Am. B* **10**, 1758-1764 (1993).

[10] Z. Sun, M. Ghotbi, and M. Ebrahim-Zadeh, "Widely tunable picosecond optical parametric generation and amplification in BiB_3O_6," *Opt. Express* **15**, 4139-4148 (2007).

[11] H. He, Q. Zhao, J. Guo, Y. Lu, Y. Liu, and J. Wang "Picosecond optical parametric generation in flux grown KTP," *Optics Comm.* **87**, 33-35 (1992).

[12] B. Köhler, U. Bäder, A. Nebel, J. P. Meyn, and R. Wallenstein, "A 9.5-W 82-MHz-repetition-rate picosecond optical parametric generator with cw diode laser injection seeding", *Appl. Phys. B* **75**, 31-34 (2002).

[13] L. Xu, H. Chan, S. Alam, D. J. Richardson, and D. P. Shepherd, "High-energy, near- and mid-IR picosecond pulse generated by a fiber-MOPA-pumped optical parametric generator and amplifier", *Opt. Express* **23**, 12613-12618 (2015).

7

Phase-locked picosecond optical parametric oscillator

This chapter constitutes the following publication:

1. **B. Nandy**, S. Chaitanya Kumar, and M. Ebrahim-Zadeh, "Phase-locked picosecond optical parametric oscillator," *Opt. Lett.* **45**, 3981-3984 (2020).

7.1 Background and motivation

The development of degenerate femtosecond optical parametric oscillators (OPOs) has provided a novel tool for the generation of broadband phase-locked radiation from the visible to mid-infrared [1-5]. Using the doubly-resonant oscillator (DRO) configuration under type 0 and type I phase-matching (identical output polarizations), the signal-idler waves become indistinguishable at degeneracy, providing the condition for the generation of phase- locked broadband output from the OPO. This effect, which was first observed in a monolithic single-mode continuous-wave DRO [6], was later shown to be also attainable in degenerate ultrafast DROs synchronously pumped by femtosecond lasers [1-5]. Common to all such ultrafast DROs is a femtosecond laser oscillator providing a phase-locked input pump, enabling down-conversion to a degenerate phase-locked broadband output centered at degeneracy. Using such ultrafast DROs, phase-locked broadband radiation from ~420 nm to ~8 μm, pumped at center wavelengths from 535 nm to 2.35 μm, has been generated with average powers up to ~500 mW [1-5].

On the other hand, the potential of picosecond laser oscillators for the generation of phase-locked radiation based on this approach has, to the best of our knowledge, not so far been demonstrated. One latent limitation of picosecond lasers is the relatively narrow bandwidth and the absence of a well-defined phase-locked input pump compared to femtosecond lasers. This could present a potential barrier to broadband phase-locked generation using this class of ultrafast oscillators. However, picosecond lasers could potentially offer attractive merits as attractive pump source for this class of OPO sources due to reduced complexity, widespread availability, lower cost, and promise for power scaling. It is, thus, important to explore the feasibility of extending the concept of phase-locked degenerate OPOs to picosecond laser oscillators.

In this chapter, we report what we believe to be the first phase- locked degenerate OPO synchronously pumped by a picosecond laser. The OPO is based on a degenerate DRO and is driven by a mode-locked Yb-fiber laser at ~80 MHz pulse repetition rate. Such picosecond OPOs in singly-resonant oscillator (SRO) configuration are now highly mature technology, capable of providing multi- Watt average powers across the near- and mid-infrared [7]. On the other hand, picosecond OPOs based on MgO:PPLN have been explored in DRO scheme to generate high-power narrowband spectral output [8]. However, their exploitation in degenerate DRO scheme for phase-locked broadband generation has not been previously demonstrated. Here we show that stable broadband phase-locked generation can be achieved with this technique using picosecond pump pulses of low intensity and narrow linewidth, even with time-bandwidth product far from the transform limit. In doing so, we also demonstrate a record average power of 2.8 W, which is to our knowledge the highest power generated by any phase-locked OPO to date.

7.2 Experimental Setup

A schematic of experimental setup for the phase-locked picosecond OPO is shown in Figure 7.1. A mode-locked Yb-fiber laser (Fianium, *FemtoPower*) delivering up to 12.4 W of average power at 1064 nm is used to synchronously pump the OPO. The laser delivers pulses of 20 ps duration with a full-width half-maximum (FWHM) spectral bandwidth of 1.5 nm at ~80 MHz repetition rate. The laser pulses are strongly chirped, with a time-bandwidth product of $\Delta\nu\Delta\tau$ ~8, more than 20 times the transform limit.

For the OPO we choose MgO:PPLN as the nonlinear crystal due to it low group velocity dispersion (GVD) for parametric generation near degeneracy when pumped at 1064 nm. The crystal has a zero GVD at 1912 nm, with GVD~-68 fs^2/mm at 2128 nm. We take further advantage of low GVD in the crystal to use a 50-mm-long interaction length for maximum nonlinear gain and conversion efficiency. The crystal incorporates a uniform grating period of Λ=32.16 μm for type 0 ($e \Rightarrow ee$) phase-matching and is housed in an oven with temperature stability of 0.1 °C. Using the relevant Sellmeier equations [9], the phase-matching temperature for parametric generation at 2128 nm is calculated to be 78.6 °C.

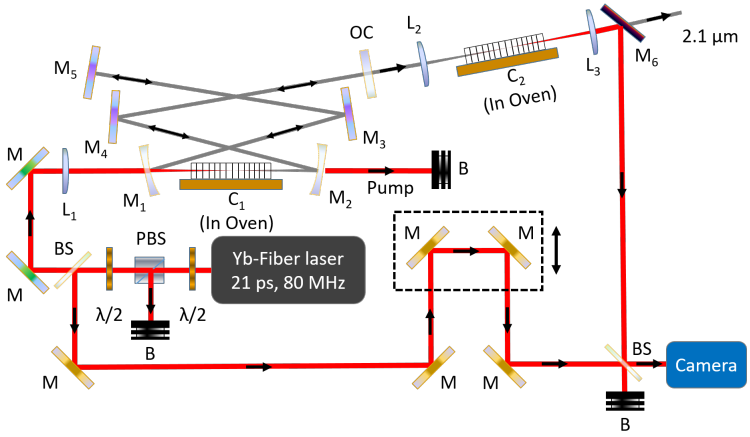

Figure 7.1: Experimental setup for the degenerate phase-locked picosecond OPO synchronously pumped by a mode-locked Yb-fiber laser. M: mirror, OC: output coupler, C: MgO:PPLN crystal, L: lens, $\lambda/2$: half-wave plate, BS: beam-splitter, PBS: polarizing beam-splitter, B: beam block.

The OPO is configured in a six-mirror standing-wave cavity comprising two concave mirrors (M_1-M_2: r=200 mm), three plane mirrors (M_3-M_5), and a plane output coupler (OC). All mirrors, M_1- M_5, have >99% reflectivity over 1900-2400 nm to allow degenerate DRO operation, while OC has 90% transmission (non-optimized) at 2128 nm for extraction and characterization of the output. The pump power to the OPO is controlled using a half-wave ($\lambda/2$) plate and a polarizing beam-splitter. A second $\lambda/2$ plate is used to control the polarization of the pump for optimum phase-matching in the MgO:PPLN crystal. The pump is focused to a beam waist radius of w_0 ~60 μm in the crystal, corresponding to a focusing parameter of ξ ~1.05 [10]. The OPO threshold is breached at an input pump power of 6.2 W, and the output performance is studied

at the maximum available pump power of 12.4 W. Phase-locked operation is confirmed by several independent measurements of OPO output.

7.3 Device tuning and characterization

In passive operation close to degeneracy, the OPO emits an unstable time-varying spectrum, typical of a DRO, as presented in Figure 7.2. Phase-locked operation is then initiated by fine adjustment of OPO cavity length together with variation of the MgO:PPLN crystal temperature to reach exact degeneracy. At 78 °C, and with precise control of cavity length, degenerate operation is established, and the condition for self-phase-locking of signal-idler pair is realized, resulting in the formation of a stable broadband output spectrum centered at 2128 nm with a bandwidth of 202 nm (10 dB level), as shown in Figure 7.2. The small discrepancy of 0.6 °C between the calculated and measured crystal temperature for exact degenerate operation is due to the design of the oven.

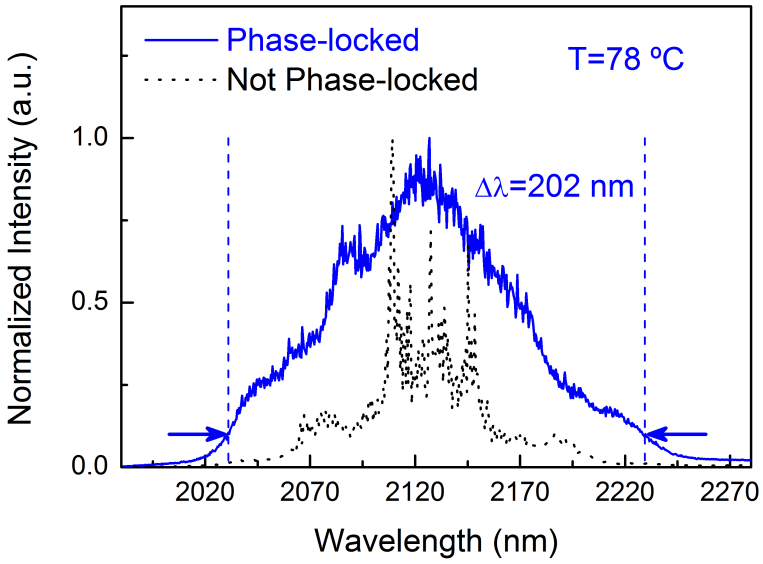

Figure 7.2: Picosecond OPO output spectrum in the absence of phase- locking and in degenerate phase-locked state.

In order to further verify phase-locking, we perform coherence measurements between the pump and degenerate OPO output using f-$2f$ interferometry [1, 3, 6]. The OPO output is frequency-doubled in an identical MgO:PPLN crystal and mixed with a portion of the input pump beam. The optical paths are matched using a delay line

and the beams are combined on a beam-splitter before recording the spatial interference pattern on a CCD camera (Coherent *Beamview*, integration time of 10 ms). In phase-locked state, a stable and persistent fringe pattern is obtained, as shown in Figure 7.3, confirming phase coherence of the OPO output. For better visualization of the fringes in a 2D image, the measurement was deliberately performed at non-zero angle between the interfering beams. The fringe pattern displays excellent stability under passive conditions and remains constant for days without the need for intervention.

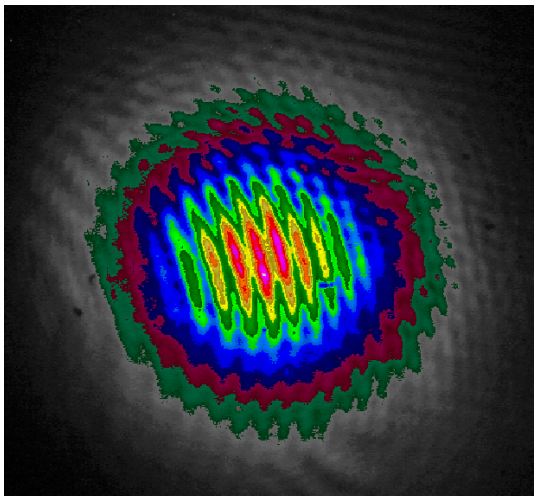

Figure 7.3: Spatial f-$2f$ interference pattern of degenerate picosecond OPO output in phase-locked state.

We also validate phase-locked generation by radio frequency (RF) measurements of OPO output in unlocked and phase-locked state. With the OPO unlocked, several satellite peaks are present in the RF spectrum, as shown by the dashed black trace in Figure 7.4. With the OPO in phase-locked state, the RF spectrum contains a single peak, as shown by the solid blue trace in Figure 7.4. The small residual features in the phase-locked RF is due to the input pump.

Having confirmed the generation of a stable phase-locked output, we studied other performance characteristics of the picosecond OPO including output power scaling and spatial beam quality, as well as spectral evolution with input pump power. The power scaling results are shown in Figure 7.5(a), where the OPO average power is seen to increase linearly with pump power at a slope efficiency of 45%. At the maximum input power of 12.4 W, the phase-locked OPO generated 2.8 W of average power, correspond-

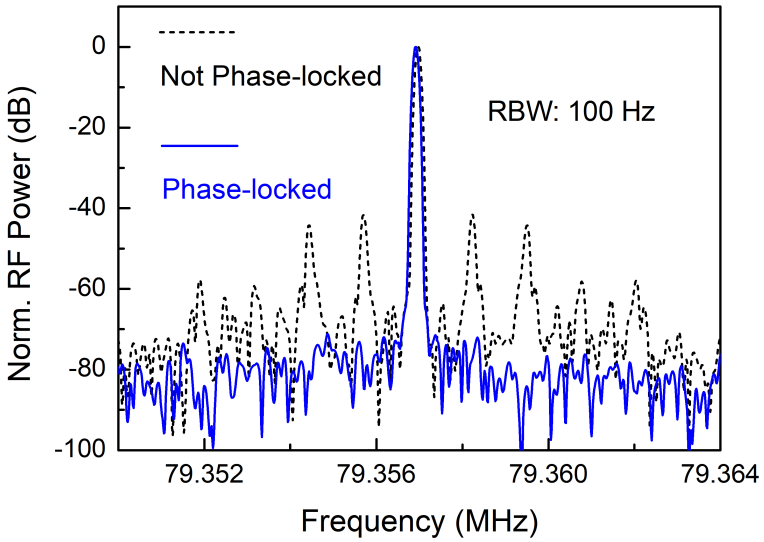

Figure 7.4: Radio-frequency spectrum of picosecond OPO output in unlocked and phase-locked state.

ing to an external efficiency of 22.6%. There is no sign of saturation in output power, thus indicating that higher powers will be attainable with increased input pump powers. The spectral evolution of the phase-locked output with input pump power is also shown in Figure 7.5(b), where it can be seen that spectral stability is achieved above ~7.5 W, soon after the OPO threshold is breached at 6.2 W. At the same time, the phase-locked spectral bandwidth is clearly observed to increase with the rise in input pump power, which we attribute to the increase in parametric gain at higher pumping intensities.

The formation of phase-locked output is also confirmed by the abrupt increase in OPO output power (from 1.8 to 2.8 W) and the marked improvement in stability (from 5.5% to 0.6% rms) over 1 hour in transition from the unlocked to phase-locked regime, as shown in Figure 7.6(a). This is also accompanied by strong stabilization of the output spectrum, from a chaotic behavior to a stable and locked profile with a 0.2% rms fluctuation in the central wavelength at 2128 nm over 1 hour, as evident in Figure 7.6(b). Once phase-locked, the OPO output power and spectrum remain stable for days under passive laboratory conditions without the need for intervention or active stabilization.

Under passive conditions in phase-locked operation, we simultaneously measured the pulse repetition rate of the OPO output, together with that of the pump, with the results presented in Figure 7.7(a,b). As expected, the synchronously-pumped OPO repetition

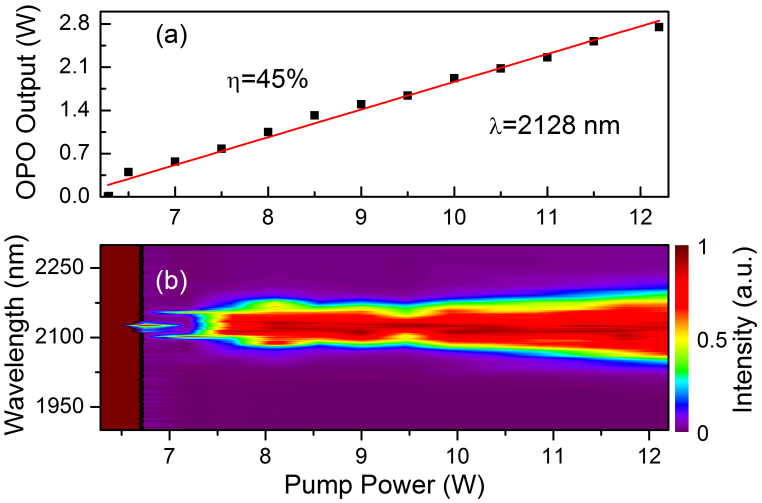

Figure 7.5: (a) Output power, and (b) spectrum of degenerate phase-locked picosecond OPO as a function of input pump power.

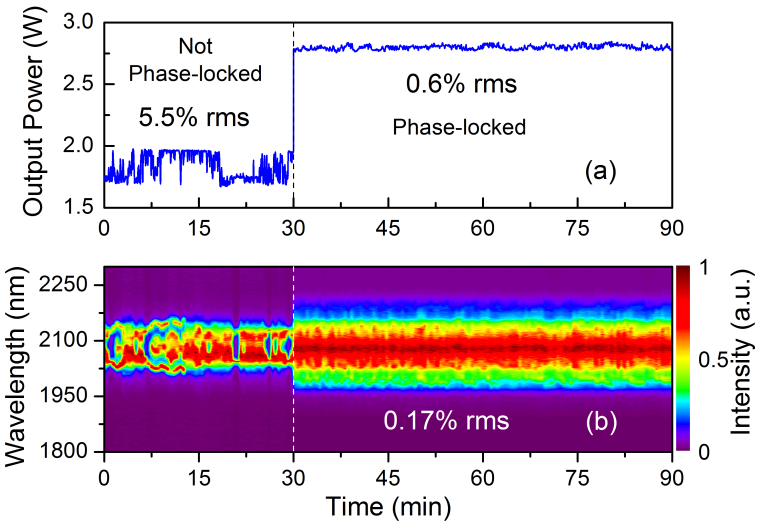

Figure 7.6: (a) Picosecond OPO output power and stability in transition from unlocked to phase-locked regime. (b) Spectral stability of picosecond OPO output in transition from unlocked to phase-locked regime.

rate follows the input pump, which exhibits a standard deviation of 4.2 Hz in over 1 hour. While the instantaneous repetition rate jitter of input pump pulse train together with the instabilities in the OPO cavity length under passive laboratory conditions in the absence of active control could be attributed to the residual fluctuations on the phase-

locked spectrum presented in Figure 7.2, the long-term drift in the repetition rate has a noticeable effect neither on the overall spectral stability nor the output power, owing to the relatively long synchronous length available in a picosecond OPO as compared to a femtosecond OPO. Further, under synchronous pumping, the phase noise of the pump and fluctuations in OPO cavity length translate into intensity noise in the output spectrum [11].

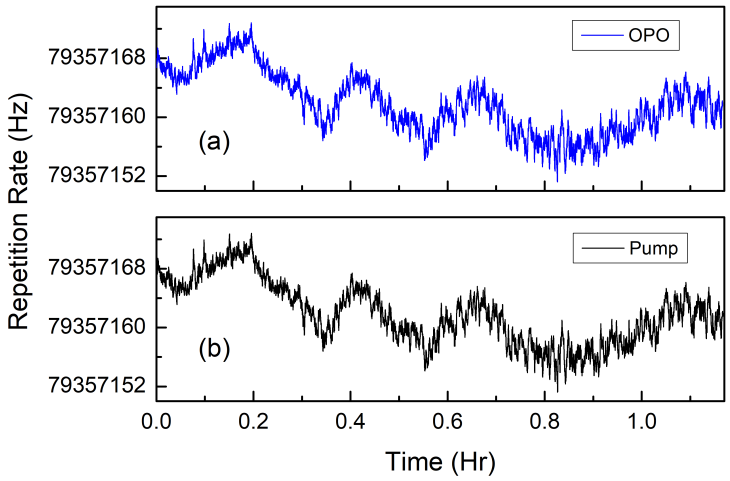

Figure 7.7: (a) Variation in repetition rate with time of (a) input pump pulse train from the picosecond Yb-fiber laser, and (b) the output pulse train from the phase-locked picosecond OPO, over 1 hour.

The spatial beam profile of the output from the phase-locked picosecond OPO recorded using a pyroelectric camera, while operating at the maximum output power of 2.8 W, is shown in Figure 7.8, confirming TEM_{00} mode profile. Further, using scanning beam profiler and focusing lens with focal length f=50 mm, we measure the beam-quality of the output from the phase-locked OPO at 2128 nm to be M_x^2<1.4 and M_y^2<2.

Finally, we perform temporal characterization of picosecond OPO in degenerate phase-locked state and at maximum output power of 2.8 W using a two-photon autocorrelator and an InGaAs photodetector. A typical interferometric autocorrelation trace of the phase-locked picosecond OPO output is shown in Figure 7.9(a). The measurements result in a FWHM width of 30 ps, corresponding to a Gaussian pulse duration of $\Delta\tau$ ~21 ps for the phase-locked output. It is also clearly evident that the output

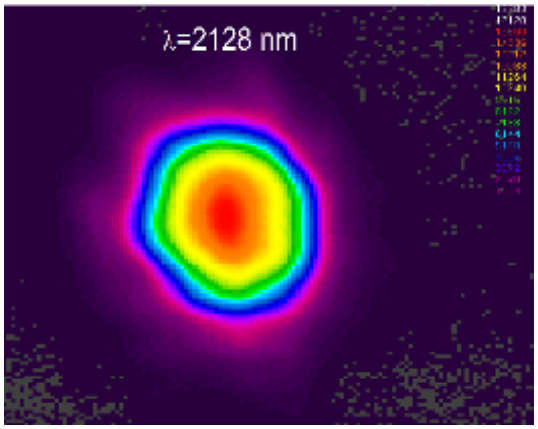

Figure 7.8: Spatial output beam profile of phase-locked picosecond OPO.

pulses are strongly chirped. This temporal measurement corresponds to the phase-locked spectrum presented in Figure 7.2. For comparison, similar measurements for the pump pulses at 1064 nm were performed using a GaAsP photodiode, with the result presented in Figure 7.9(b), clearly confirming strongly chirped input pulses with Gaussian pulse duration of $\Delta\tau$ ~20 ps. Also shown in the inset of Figure 7.9(b) is the pump spectrum with an FWHM spectral bandwidth of 1.5 nm centered at 1064 nm. The results confirm that the non-ideal temporal characteristics of input pump pulses are directly transferred to the phase-locked OPO output pulses. Therefore, with improvements in the temporal quality of input pump pulses, one can expect further enhancement in the output pulse characteristics of the phase-locked picosecond OPO.

7.4 Conclusions

In conclusion, we demonstrated a broadband phase-locked degenerate picosecond OPO, for the first time, synchronously pumped by a mode-locked Yb-fiber laser. We have shown that despite non-ideal characteristics of the pump laser with regard to a narrow linewidth and a time-bandwidth product far from the transform limit, robust and reliable phase-locked generation with exceptional power, excellent passive power and spectral stability, and good spatial quality is attainable. The phase-locked picosecond OPO provides a record average power of 2.8 W in pulses of 21 ps at ~80 MHz repetition rate with a spectral bandwidth of 202 nm centered at 2128 nm. We have validated phase-locked operation by measurements of OPO output power and spectral stability,

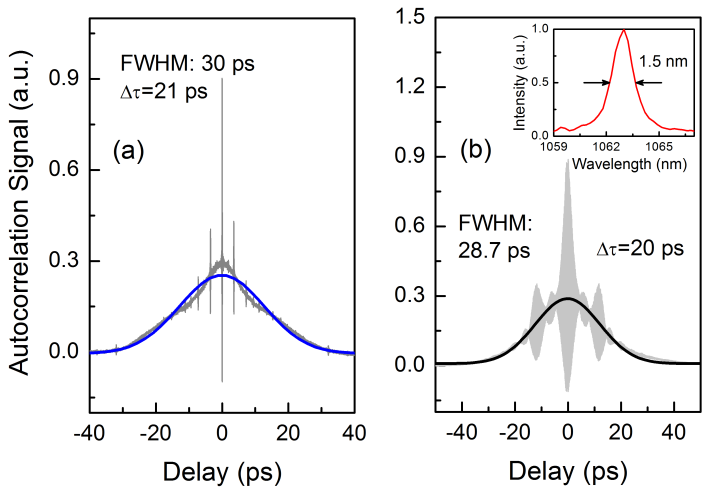

Figure 7.9: Typical interferometric autocorrelation profile of (a) phase-locked OPO output pulses at 2128 nm, and (b) input Yb-fiber pump pulses at 1064 nm.

RF spectrum and f-2f interferometry, and have observed spectral broadening of the phase-locked output with input pump power. The phase-locked bandwidth and output power can be further increased by scaling the input pump power, which is readily attainable with picosecond Yb-fiber lasers. Active stabilization of OPO cavity and the use of input pump pulses of improved spectral and temporal quality with reduced repetition rate jitter and transform-limited characteristics are also expected to lead to further improvements in the performance of the phased-locked picosecond OPO with regard to power and spectral stability, and chirp-free output pulses.

This initial demonstration points to the feasibility of developing phase-locked picosecond OPO sources with multi-Watt average powers using relatively simple, low-cost, and widely available mode-locked fiber pump lasers, paving the way for new applications in remote sensing, atmospheric optics, free-space communications, astronomy, and more. The approach can also be extended to other spectral regions using alternative picosecond lasers and nonlinear materials.

References

[1] S. T. Wong, T. Plettner, K. L. Vodopyanov, K. Urbanek, M. Digonnet, and R. L. Byer, "Self-phase-locked degenerate femtosecond optical parametric oscillator," *Opt. Lett.* **33**, 1896-1898 (2008).

[2] A. Marandi, N. C. Leindecker, V. Pervak, R. L. Byer, and K. L. Vodopyanov, "Coherence properties of a broadband femtosecond mid-IR optical parametric oscillator operating at degeneracy," *Opt. Express* **20**, 7255-7262 (2012).

[3] V. Ramaiah-Badarla, A. Esteban-Martin, and M. Ebrahim-Zadeh, "Self-phase-locked degenerate femtosecond optical parametric oscillator based on BiB_3O_6," *Laser Photon. Rev.* **7**, L55-L60 (2013).

[4] V. Smolski, S. Vasilyev, I. Moskalev, M. Mirov, Q. Ru, A. Muraviev, P. Schunemann, S. Mirov, V. Gapontsev, and K. Vodopyanov, "Half-Watt average power femtosecond source spanning 3–8 μm based on subharmonic generation in GaAs," *Appl. Phys. B* **124**, 101 (2018).

[5] Y. Chen, M. C. Silfies, G. Kowzan, J. M. Bautista, and T. K. Allison, "Tunable visible frequency combs from a Yb-fiber-laser-pumped optical parametric oscillator," *Appl. Phys. B* **125**, 81 (2019).

[6] C. D. Nabors, S. T. Yang, T. Day, and R. L. Byer, "Coherence properties of a doubly resonant monolithic optical parametric oscillator," *J. Opt. Soc. Am. B* **7**, 815-820 (1990).

[7] M. Ebrahim-Zadeh, and S. Chaitanya Kumar, "Yb-fiber-laser-pumped continuous-wave frequency conversion sources from the mid-infrared to the ultraviolet," *IEEE J. Sel. Top. Quantum Electron.*, **20**, 350-372 (2014).

[8] S. Chaitanya Kumar, and M. Ebrahim-Zadeh, "Yb-fiber-based, high-average-power, high-repetition-rate, picosecond source at 2.1 μm," *Laser Photon. Rev.* **10**, 970-977 (2016).

[9] O. Paul, A. Quosig, T. Bauer, M. Nittmann, J. Bartschke, G. Anstett, and J. A. L'huillier, "Temperature-dependent Sellmeier equation in the MIR for the extraordinary refractive index of 5% MgO doped congruent $LiNbO_3$," *Appl. Phys. B* **86**, 111-115 (2007).

[10] G. D. Boyd, and D. A. Kleinman, "Parametric interaction of focused Gaussian light beams," *J. Appl. Phys.* **39**, 3597-3639 (1968).

[11] J. M. Dudley, D. T. Reid, M. Ebrahim-Zadeh, and W. Sibbett, "Characteristics of a noncritically phasematched Ti: sapphire pumped femtosecond optical parametric oscillator," *Opt. Commun.* **104**, 419-430 (1994).